Chapter 7

WRF-LES-GAD/GAL model verification and validation

The WRF-LES-GAD (WLGD or simply GAD) and WRF-LES-GAL (WLGL or simply GAL) models are used to carry out high-fidelity large-eddy simulations of turbulent wind fields in the stratified atmospheric boundary layer (ABL) flows and study the effects of atmospheric stability on the wake characteristics and aerodynamic response of a wind turbine (WT). The verification and validation analyses of the WLGD and WLGL models are presented against numerical results from the available LES codes and experimental data. The presented verification starts with the analysis of WT wake aerodynamics in non-turbulent uniform inflow conditions and continues with the comparison of the predicted turbulent non-uniform wind field results and the aerodynamic performance of the WT against field data for varying ABL conditions. A sensitivity analysis has been conducted to appropriately select parameters for wind turbine parameterizations in preparation for further studies. The analysis employs the WLGL model under non-turbulent constant inflow conditions.

7.1 Case 1: Wind turbine wake aerodynamics under constant inflow conditions

In wind turbine wake modeling, laminar flow refers to a situation where the wind flow approaching the WT is smooth and steady without any turbulence. In non-turbulent flow, the wake behind the wind turbine is typically characterized by a relatively symmetrical flow pattern. The wind flow field behind the WT rotor is less complex and more predictable than for turbulent inflow conditions.

This section relies on a part of the content of an extended abstract that has been presented at an international conference:

- Kale, B., Buckingham, S., van Beeck, J. and Cuerva-Tejero, A., 2021. Multiscale wind turbine wake modeling within a wind farm using the WRF-LES model: An application to the Lillgrund offshore wind farm. *Wind Energy Science Conference 2021*, Hannover, Germany, 25-28 May 2021 (online).

A baseline test case with non-turbulent inflow under neutral ABL conditions is designed to verify the WLGD and WLGL model results against data from different LES codes reported in Martinez-Tossas et al. [208]. These reference LES codes parameterize the wind turbine rotor using a generalized actuator line wind turbine model. The results of the WLGD and WLGD models have been compared to four different LES codes that are namely: LESGO, a pseudo-spectral LES code from the Johns Hopkins University (JHU), SOWFA, a finite volume LES code from the National Renewable Energy Laboratory (NREL), SP-Wind, a pseudo-spectral LES code developed by the Turbulent Flow Simulation and Optimization Group at KU Leuven (KUL), and EllipSys3D, a finite volume LES code from the Technical University of Denmark (DTU). A description of the simulated flow, details of the numerical set-up, and the model results are included in the following sections.

7.1.1 Numerical set-up

The wind turbine chosen for this analysis is the NREL 5MW reference WT with a rotor diameter, $D = 126$ m and hub height, $z_{hub} = 90$ m [147]. The schematics of the computational domain used in the reference paper and in the current work are shown in Figures 7.1 and 7.2, respectively. The reference simulations employ uniform inflow at the inlet and the standard Smagorinsky subfilter-scale with a fixed Smagorinsky coefficient, that is $c_s = 0.16$, is utilized. The LESGO code utilizes periodic boundary conditions (BCs) in the longitudinal and one of the lateral directions in pseudo-spectral mode, and the spatial discretization in the other lateral direction is done by using a second-order, central finite difference scheme. Zero shear stress BCs are prescribed in this direction. Time integration is done using the second-order Adams-Bashford method. The SOWFA code employs a second-order numerical discretization in both space and time, and the boundary conditions are set to uniform inflow with zero normal pressure gradient at the inlet, zero normal gradient of velocity, and fixed pressure at the outlet. The lateral boundary conditions are set to zero gradient. Temporal discretization is achieved by employing a second-order backward differentiation scheme. Similar to the LESGO model, the SP-Wind pseudo-spectral LES code also uses pseudo-spectral discretization in the longitudinal and lateral directions. Fourth-order finite discretization is used for the other lateral direction. The BCs are periodic in the pseudo-spectral directions with zero stress condition in the finite-difference direction. Time advancement is done using a standard fourth-order Runge-Kutta method. The EllipSys3D, a finite volume solver that uses multi-block structured grids, employs a blended spatial discretization algorithm that is a blend of second-order central differencing scheme (10%), along with a third-order Quadratic Upstream Interpolation for Convective Kinematics (QUICK) scheme (90%) for diffusive and convective terms. The BCs are set to symmetry on the walls with inflow and convective outflow boundary conditions. Time advancement is achieved using a second-order backward Euler scheme and the solution is marched in time using inner time stepping. The pressure correction equation is solved using the Pressure-Implicit with Splitting of Operator (PISO) algorithm.

Idealized WRF-LES simulations are performed by employing two domains, with a one-way

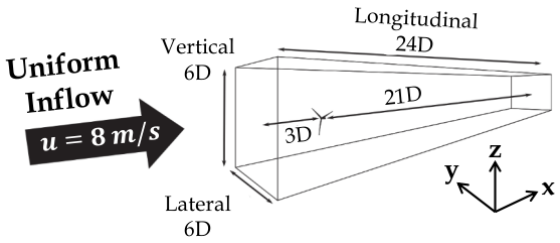

Figure 7.1: Schematic of the computational domain used by four different LES codes. Reproduced from: Martínez-Tossas et al. [207].

nesting strategy, due to the unavailability of fixed velocity BC at the inlet. In general, the WRF model provides several lateral BC options, which are periodic, symmetric, and open radiative, also referred to as gravity-wave radiating boundary condition. In the latter, the momentum equation for the horizontal velocities along a boundary on which the condition is specified, given in Equations (5.29) and (5.30), is replaced by

$$\delta_\tau U'' = -U^* \delta_x u, \tag{7.1}$$

where $U^* = \min(U - c_b, 0)$ at the $x = 0$ (western) boundary, $U^* = \max(U + c_b, 0)$ at the $x = L$ (eastern) boundary, and likewise for the south and north boundaries of the V momentum. Here, δ_τ is the temporal difference operator, and δ_x is the horizontal difference operator evaluated in a one-sided manner using the difference between the boundary value and the value one grid point into the grid, from the boundary. c_b, which is specified as a model constant, is the phase speed of the gravity waves that are to be radiated [304]. Because there is no fixed BC option for velocity to be defined at the inlet boundary in WRF, a two-domain configuration has been used with a large buffer zone between the outlet of the child (nested) and parent domains to allow for the dispersion of wind turbine wake effects. Since periodic BCs are used for the parent domain by default, the wind flow is recycled from the parent domain's outlet into the nested domain. The recycled wind flow is no longer affected by the presence of the wind turbine, as there is no turbulence in the buffer zone and the wake effects are attenuated.

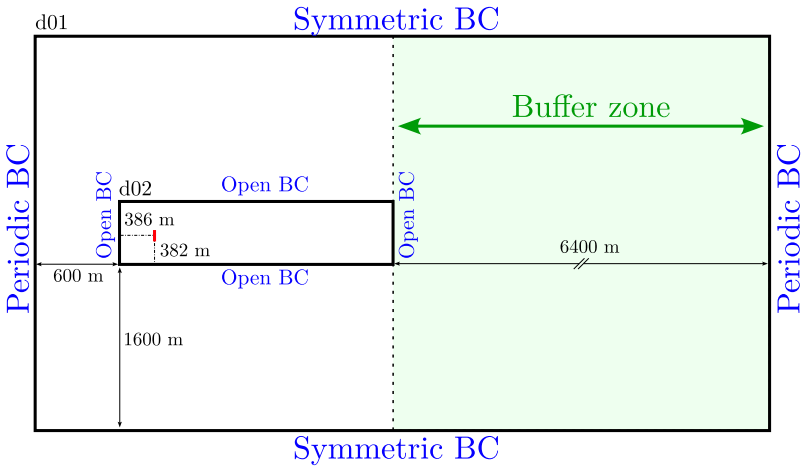

Figure 7.2: Schematic of the WRF-LES computational domains (top view).

Table 7.1: Domain dimensions of the reference LES codes and WLGD/WLGL models.

LES code	Domain	$N_x \times N_y \times N_z$	SDs [m]	FDDs [m]	L_x [m]	L_y [m]	L_z [m]
All LES codes [208]	single	$768 \times 192 \times 384$	~ 4	~ 2	3024	756	756
			$\Delta x = \Delta y$ [m]	Δz [m]			
WLGD/WLGL	d01	$251 \times 101 \times 187$	40	~ 4	10000	4000	756
	d02	$751 \times 191 \times 187$	4	~ 4	3000	760	756

Note. N_x, N_y, and N_z stand for the number of grid points whereas $\Delta x, \Delta y$, and Δz represent the spatial grid resolutions in the x, y, and z directions, respectively. Note that Δz is set close to ~ 2 m and cannot be directly set equal to $\Delta x = \Delta y = 2$ m, because of WRF's terrain-following eta coordinate system in the vertical direction. L_x, L_y, and L_z represent physical dimensions of the domain in the x, y, and z directions, respectively. SD refers to spectral directions whereas FDD refers to finite difference directions reported in Martinez-Tossas et al. [208].

In addition, a large nesting ratio, $\Delta x_{d01}/\Delta x_{d02} = 10$, has been used to increase the wake recovery rate in the buffer zone. Such an approach allows simulating a constant velocity BC at the inlet of the nested domain, thus allowing the WLGD and WLGL results from the nested domain to be compared directly with those from the reference CFD codes. To sum up, periodic BCs have been used at the inlet (west) and outlet (east) of the parent domain, whereas symmetric BCs have been used for the lateral boundaries (north and south). For the nested domain, open radiative BCS have been set for all domain boundaries. The surface kinematic heat flux, $Q_s = (\overline{w'\theta'})_s$, was set to $Q_s = 0$ and no surface layer parameterization scheme was used. Temporal discretization is achieved by a third-order Runge–Kutta scheme, whereas the horizontal and vertical advection schemes are based on fifth- and third-order finite difference approximations.

In all simulations reported in the reference paper, the grid resolution was set to $\Delta/D = 0.03125$ in the spectral directions (SDs) and $\Delta/D = 0.015625$ in the finite difference directions (FDDs), whereas a uniform grid spacing in all directions, $\Delta x = \Delta y \approx \Delta z$, was set to $\Delta x = \Delta y \approx \Delta z \approx 4$ m in WLGD and WLGL simulations.

The rotational speed of the wind turbine is 9.155 rpm, corresponding to a tip-speed ratio (TSR), $\lambda = 7.55$. In order to smear out the aerodynamic loads, computed at the WT actuator points, onto the computational grid, a Gaussian function was used. A value for the regularization kernel $\epsilon \geq 2.5\Delta x$ was used.

The chord and twist angle, as a function of blade radius, were linearly interpolated using tabulated airfoil data. The number of actuator points was $N = 64$ for all codes and no tip correction was used in any of the codes. Non-tilted rotor shaft configuration without the aerodynamic effects of the nacelle and tower were considered.

The simulations were run over a period of flow time to allow sufficient time for the wake to develop. Afterwards, they were time-averaged for 1-2 flow-through times for comparison. The chosen time step ensures that the tip of the blade does not pass through more than one grid cell in one time step. The computational set-up for all simulations is summarized in Table 7.1.

In all simulations, the wind turbine was placed at $3D$ from the inlet of the parent domain, and centered in the lateral and vertical directions. The wall effects were turned off in order to simulate non-shear wind flow. In WLGD and WLGL simulations, a uniform potential temperature profile with no capping inversion was prescribed at the inlet of the parent domain, allowing for the simulation of constant inflow through the wind turbine rotor. All simulations were forced with a constant inflow velocity, $U_\infty = 8$ m s^{-1}, and the air density was set to, $\rho = 1.0$ kg m^{-3}.

7.1.2 Results

Time- and blade-averaged (for all reference codes and WLGL model) or time- and disk-averaged (for the WLGD model) quantities (hereinafter referred to as mean quantities) are shown in Figure 7.3. Note that 36 radial lines are used to represent the wind turbine rotor in the WLGD model. Reference BEM results shown in Figure 7.3 are obtained by solving BEM equations iteratively without tip loss correction. The distributions of the mean angle of attack, $\overline{\alpha}$, along the nondimensional radial distance, r/R, with r being the radial distance and R being the blade span, agree quite well with the BEM results. As reported in the reference paper, the main differences were found in the mean longitudinal velocity distribution compared to the BEM results, especially at the root and tip of the blade. However, almost all the LES codes, WLGD and WLGL models show a similar trend between $r/R \approx 0.2$ and $r/R \approx 0.8$.

The mean nondimensional drag force, $\overline{F}_D^*$, is given by

$$\overline{F}_D^* = \frac{\overline{F}_D}{lD\rho U_\infty^2}, \tag{7.2}$$

where $\overline{F}_D$ is the mean drag, D is the rotor diameter, and l represents the width of each blade segment in the radial direction. The distributions of $\overline{F}_D^*$ also agree reasonably well with the reference BEM data, except for slight differences observed at the blade root. No significant differences were found in radial distributions of the mean nondimensional lift force, $\overline{F}_L^*$, which is given by

$$\overline{F}_L^* = \frac{\overline{F}_L}{lD\rho U_\infty^2}, \tag{7.3}$$

where $\overline{F}_L$ is the mean lift. This means that the implementation of the generalized actuator disk an actuator line models in every code is similar. Note that the nondimensional mean drag (Equation (7.2)) and lift (Equation (7.3)) used for code-to-code comparison in this study are alternative representations of the original definitions of drag and lift coefficients, which are given by Equation (7.4).

One major reason for the mismatch between the results from BEM and LES codes is the chosen value of the regularization kernel width, ϵ [207]. The discontinuities in the distribution of mean dimensionless drag and lift are because the distribution of the airfoil profiles along the blade does not change as smoothly as in reality. A smoother radial distribution of airfoil characteristics can be achieved by interpolating the lift and drag

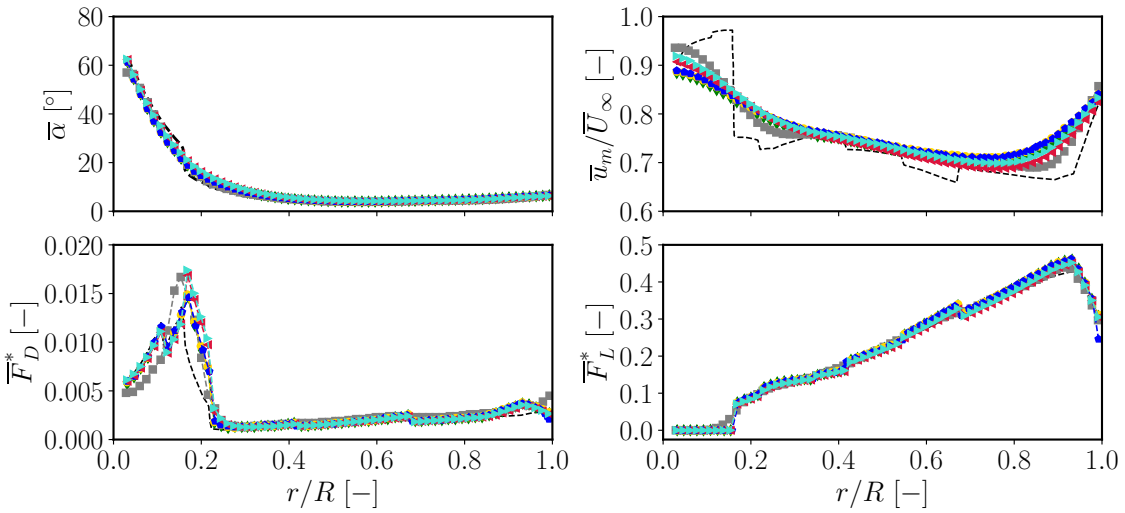

Figure 7.3: Time- and blade-averaged angle of attack, $\overline{\alpha}$ (upper left), nondimensional longitudinal velocity, $\overline{u}_m/U_\infty$ (upper right), nondimensional drag, $\overline{F}^*_D$ (lower left), and lift, $\overline{F}^*_L$ (lower right), as a function of nondimensional radial distance, r/R, along the blade. BEM (- - -), DTU (- - -), KUL (- - -), NREL (- - -), JHU (- - -), WLGD (- - -), and WLGL (- - -).

tables between adjacent sections of the blades, which was done by the EllipSys3D code from DTU; therefore, smoother drag and lift distributions were found in the results of that code. Although the quantities discussed herein are obtained in a discrete way along the blade, the aerodynamic loads predicted by the generalized actuator disk and actuator line models are distributed smoothly onto the computational grid, using a Gaussian distribution function, explaining why the smoothness of the nondimensional distribution of the mean longitudinal velocity along the blade. Nevertheless, no significant difference was observed across all research codes, although the WLGD model does not parameterize the wind turbine blades as rotating lines.

Figure 7.4 illustrates the color maps of time-averaged normalized longitudinal velocity, $\overline{u}/U_\infty$, field in the x-z plane for the LES codes. The near-to-mid wake region, up to approximately $x/D = 5$, evidenced no significant differences among the codes. This is because turbulence was not triggered in that position of the wake. Starting from $x/D \sim 7$, different velocity fields were observed once turbulence was evident.

Even though the same SFS closure scheme was utilized in all simulations, laminar to turbulent transition is more evident in color maps of the time-averaged normalized longitudinal component of the Reynolds stress tensor, $\overline{u'u'}/U^2_\infty$, field in the x-z plane (Figure 7.5). It has been observed that $\overline{u'u'}/U^2_\infty$ field up to roughly $5D$ downstream of the rotor plane is almost zero for all the LES codes, despite the different numerical discretization schemes employed by each code. Nevertheless, when laminar to turbulent transition occurs (approximately at 7-8D), the wake velocity fields begin to differ from each and a faster transition to turbulence in codes based on higher-order numerical schemes is observed. Due to the fact that the higher wave numbers in the derivatives are damped in the codes

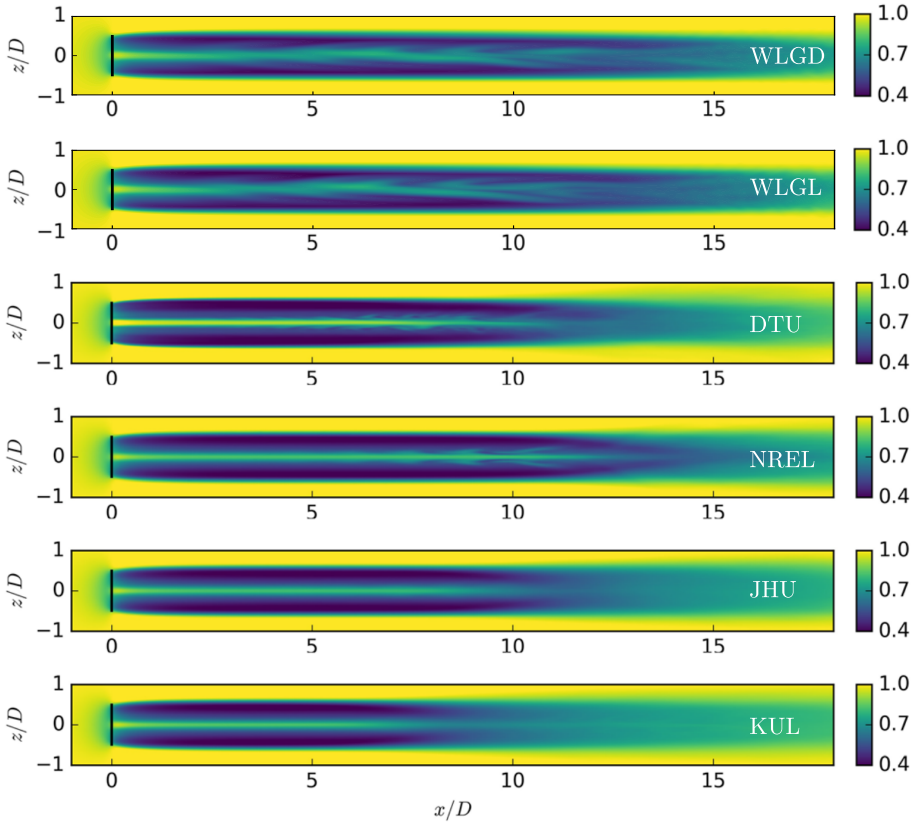

Figure 7.4: Color maps of time-averaged normalized longitudinal velocity, $\overline{u}/U_\infty$, field in the x-z plane from different LES codes. The colorbar refers to the magnitude of $\overline{u}/U_\infty$, ranging between 0.4 and 1. The vertical black line denotes the location of the wind turbine rotor.

based on finite differencing, a delayed laminar to turbulent transition occurs in the WRF-LES and NREL codes (except for the DTU code in which the transition to turbulence occurred slightly earlier than other finite difference and finite volume codes). In contrast, pseudo-spectral codes from KUL and JHU predict faster transition due to the presence of higher wave numbers in the derivatives of governing equations employed by numerical discretization schemes [208].

Figure 7.6 shows the vertical profiles of the time- and blade-averaged longitudinal velocity component, $\overline{u}_m/U_\infty$, at different distances downstream of the wind turbine rotor. The mean longitudinal velocity profiles show a similar trend in the near wake, up to $x/D = 3$, yet the results from the WLGD and WLGL models start to differ from other LES codes at the wake center. This may be due to the coarser grid resolution utilized for the WLGD and WLGL simulations, which is twice the grid resolution used in other codes.

Figure 7.7 shows vertical profiles of the mean longitudinal Reynolds stress tensor component at different distances downstream of the wind turbine rotor. The vertical profiles of the mean longitudinal Reynolds stress tensor component for the generalized actuator line models show a very similar trend in the rotor plane, $x/D = 0$, yet the result from the WLGD model significantly differs from other LES codes. This is an inherent result of the

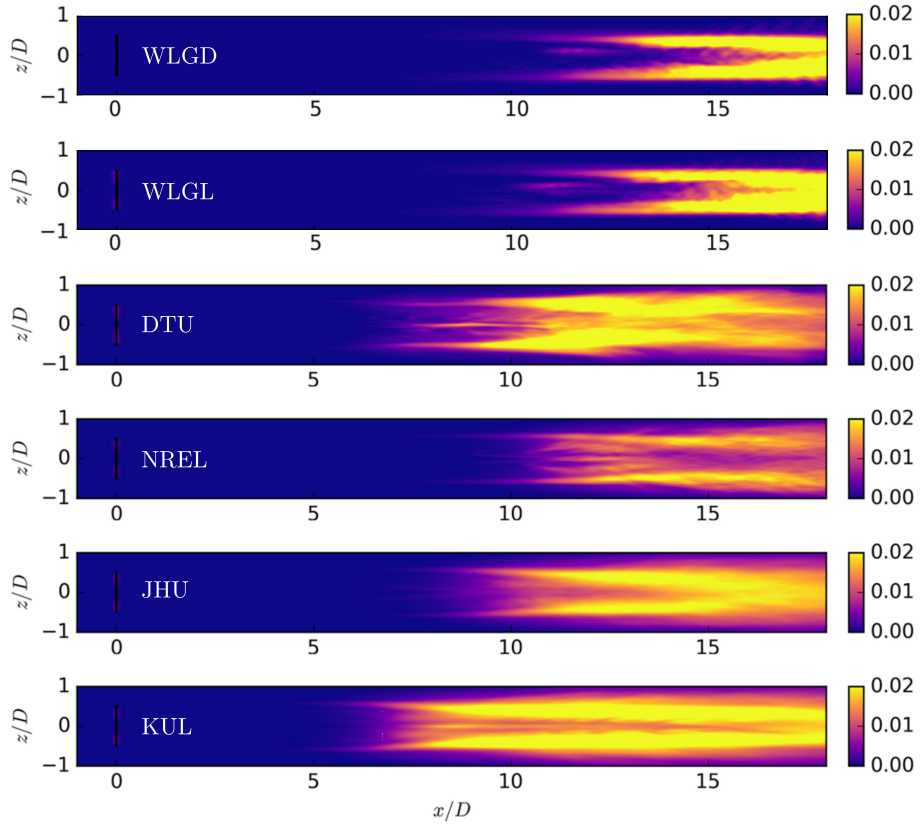

Figure 7.5: Color maps of the time-averaged normalized longitudinal component of the Reynolds stress tensor, $\overline{u'u'}/U_\infty^2$, field in the x-z plane from different LES codes. The colorbar refers to the magnitude of $\overline{u'u'}/U_\infty^2$, ranging between 0 and 0.02. The vertical black line denotes the location of the wind turbine rotor.

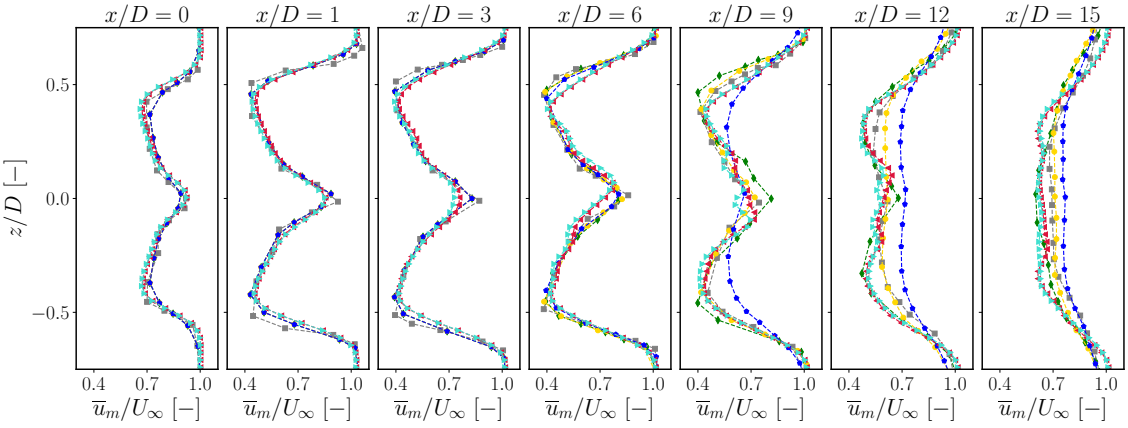

Figure 7.6: Vertical profiles of time- and blade-averaged longitudinal velocity component, $\overline{u}_m/U_\infty$, at different locations downstream of the wind turbine rotor. DTU (- - -), KUL (- - -), NREL (- - -), JHU (- - -), WLGD (- - -), and WLGL (- - -).

implementation of the generalized actuator disk model, as it does not track the rotation of the blades in time. Even though the rotational effects are considered in the WLGD model, the time- and disk-averaged longitudinal Reynolds stress tensor component yields a quasi-uniform profile in the vertical direction. As illustrated in the color maps of the time-averaged normalized longitudinal component of the Reynolds stress tensor in Figure 7.5,

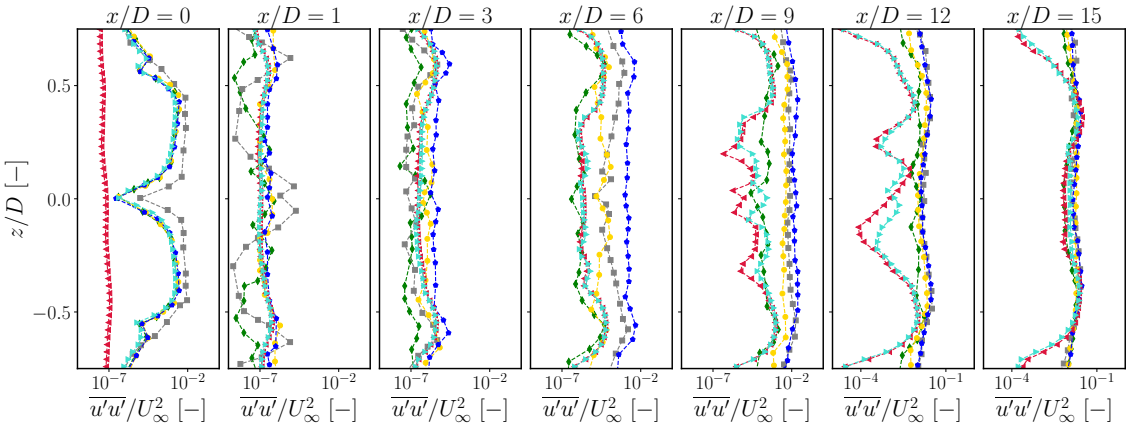

Figure 7.7: Vertical profiles of longitudinal Reynolds stress tensor component, $\overline{u'u'}/U_\infty^2$, at different locations downstream of the wind turbine rotor. DTU (- - -), KUL (- - -), NREL (- - -), JHU (- - -), WLGD (- - -), and WLGL (- - -). Note that the x-axis scale for the vertical profiles at $x/D \geq 12$, where the wake has become turbulent, is larger than at other locations.

almost no turbulence was produced by the blades in the rotor plane at $x/D = 0$. However, as the wake propagated through the domain outlet, the magnitude of $\overline{u'u'}/U_\infty^2$, which is an indicator of laminar-to-turbulent transition, became to increase. The differences are smaller in the far wake after the wind flow becomes turbulent in all LES codes. When the Reynolds stress term becomes several times higher, it means that turbulence is triggered in the wake.

Recall that not only numerical discretization schemes but also BCs are not identical in all LES codes. Therefore, the exact comparison of vertical profiles at downstream locations where the wake becomes turbulent is not straightforward. In other words, the comparison of the results in the near wake, where the wind flow is laminar, and hence there is no vortex break-up, may provide more reliable information when comparing vertical profiles of any quantity across all LES codes.

7.1.3 Sensitivity analysis for selection of wind turbine model parameters

The parameters that may be varied in a sensitivity analysis for a generalized actuator line model, such as the WLGL model, include the aerodynamic force smearing function, regularization (smearing) kernel width, and functions for correcting the airfoils to account for three-dimensional aerodynamic effects. The sensitivity of the model output, such as power, thrust, and torque, as well as wake velocity deficit, the radial distribution of some aerodynamic parameters like the angle of attack, nondimensional drag and lift coefficients, and so on, to changes in these parameters, can then be analyzed to determine the importance of each parameter in determining the overall performance of the wind turbine. With this regard, the above-mentioned effects were tested using the same inflow conditions utilized for the simulation of the NREL 5MW WT for constant inflow conditions. The WLGL model selected for the sensitivity analysis was run for 10-min without tower and nacelle effects included. Non-tilted rotor shaft and zero blade precone configuration were consid-

ered. A total number of 16 simulations were run and the results were then time averaged over 2-min. Instantaneous WLGL data was output every 10 s for comparison.

Aerodynamic force smearing

As already mentioned, wind turbine parameterizations require an aerodynamic force spreading function to distribute the local aerodynamic forces exerted by the actuator lines over a given area instead of applying them at a single point. Within the smearing area, the force exerted by each actuator line is distributed using a weighting function, typically based on a Gaussian distribution or other weighting functions, which can be linear, polynomial, or exponential. This distribution helps smooth the effect of the actuator lines by reducing the impact of numerical errors that can result from the discrete representation of the blades. In theory, there is no significant difference between the results of the different aerodynamic force-smearing functions.

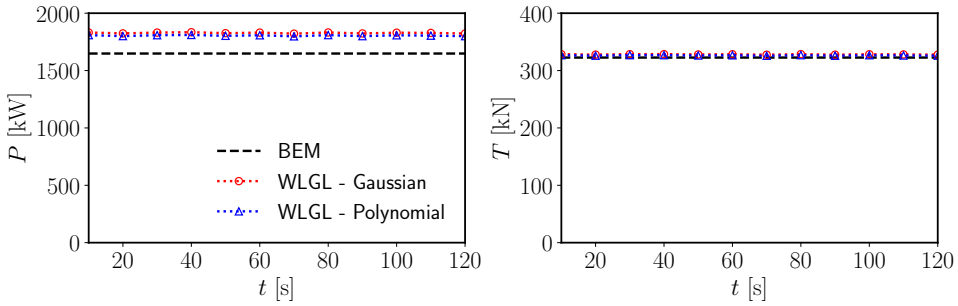

Figure 7.8: Comparison of 2-min time-series of aerodynamic power (left) and thrust (right) from the WLGL model. The dotted red line with an open circle marker denotes the results from the Gaussian force smearing function, whereas the dotted blue line with a triangle marker denotes the results from the polynomial force smearing function. The dashed black line refers to the results from the BEM model. All simulations were performed for a freestream wind speed of $U_\infty = 8$ m s^{-1} for a constant inflow.

Figure 7.8 compares 2-min time-series of aerodynamic power and thrust from the WLGL model using the Gaussian (Equation (5.121)) and polynomial (Equation (5.122)) distribution functions. For the WLGL simulations, the same numerical set-up was used. The aerodynamic force smearing kernel width, ϵ, was set to $\epsilon/\Delta x = 2.5$ and no blade root/tip and airfoil correction functions were used. Both findings demonstrate that there is no significant difference between the two different weighting functions in terms of power and thrust estimates; thereby, the results are invariant with the use of different aerodynamic force-smearing functions. Nonetheless, a difference was observed in the power estimates from both weighting functions compared to the BEM data. The mean relative difference between WLGL estimates and BEM data regarding aerodynamic power is 10.9% and 9.5% for the Gaussian and polynomial weighting functions, respectively. For thrust, it is 1.7% and 1.2%.

Regularization (smearing) kernel width

The regularization kernel, ϵ, is typically defined as a two-dimensional or three-dimensional function that depends on the distance from the center of the smearing area to the location at which the force is being applied. The shape of the regularization kernel is chosen based on the desired smoothing effect, the grid resolution of the CFD simulation and the expected size of the turbulent eddies in the flow.

Qualitatively and quantitatively, the impact of regularization kernel width, ϵ, on the wake development, radial distributions of the angle of attack and time- and-disk-averaged velocity, and power, thrust, and torque estimates were investigated using the Gaussian force distribution function. It is known that a lower bound of $\epsilon/\Delta x = 2$ should be used for an oscillation-free solution, as suggested by Troldborg [347]. The researchers have performed similar sensitivity analyses in many studies to investigate the influence of ϵ by changing the grid resolution and keeping the relation $\epsilon/\Delta x = 2$ [207, 347]. However, different studies have been carried out to examine the effect of ϵ by keeping the grid resolution constant. Doing so gives a broader insight into how regularization kernel width affects the predictions of the models, mainly when using coarse grid resolutions.

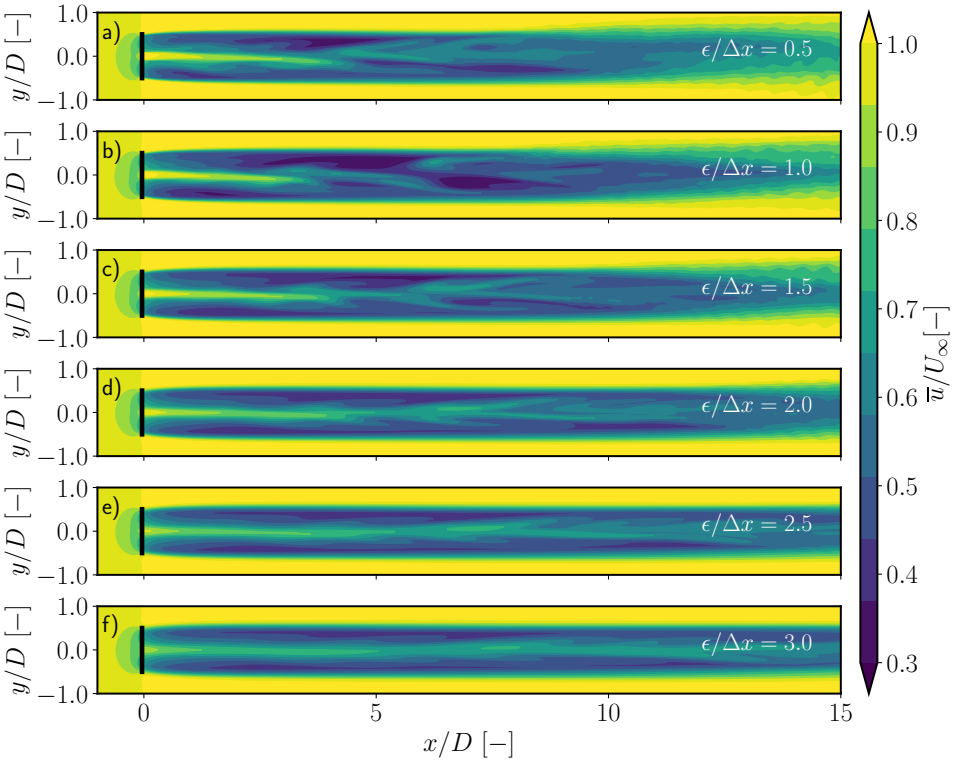

Figure 7.9: Normalized mean longitudinal velocity contours in a horizontal plane through the WT hub for different values of $\epsilon/\Delta x$. The position of the WT rotor is indicated by the black line. All simulations were performed for a freestream wind speed of $U_\infty = 8$ m s^{-1} for a constant inflow.

Figure 7.9 shows contours of mean longitudinal velocity component for the WLGL model for different values of $\epsilon/\Delta x$. These findings reveal that changing the value of $\epsilon/\Delta x$ and keeping the same grid resolution produces significant differences in the wake prediction.

Smaller values of $\epsilon/\Delta x$ produce thinner shear layers, with larger values of longitudinal velocity in the center of the wake. The main difference was observed in the center of the wake. The ϵ parameter affects the load distribution being applied onto the flow field, in turn, the configuration of the near wake. Increasing the value of $\epsilon/\Delta x$ leads to a smoother distribution of loads in the flow field, with a more gradual decrease towards the blade tip and root, thereby resulting in a larger gap between the blades. Conversely, decreasing the value of $\epsilon/\Delta x$ leads to a more concentrated distribution of loads near the blade tip and root. This can cause the shear layer to become thinner and more unstable, leading to a faster transition to turbulence.

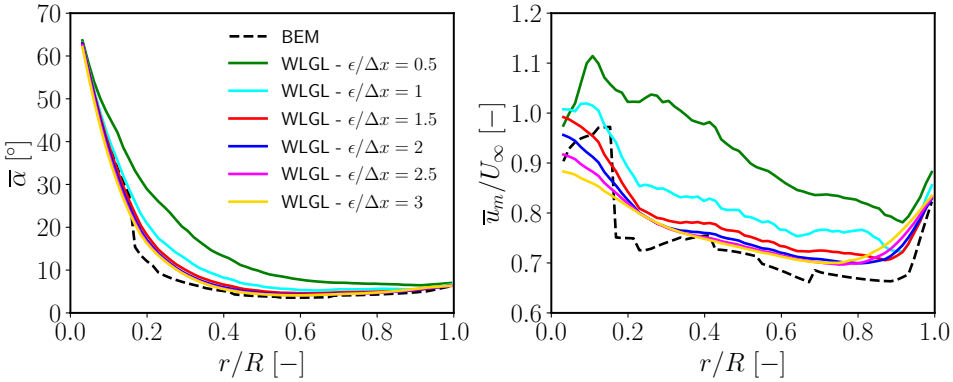

Figure 7.10: Time- and blade-averaged angle of attack, $\overline{\alpha}$, and normalized longitudinal velocity, $\overline{u}_m/U_\infty$, as a function of nondimensional blade length, r/R, for different values of $\epsilon/\Delta x$. All simulations were performed for a freestream wind speed of $U_\infty = 8$ m s^{-1} for a constant inflow.

Figure 7.10 shows the time-averaged angle of attack (left) and normalized longitudinal velocity (right) for the GAL along the blade for different values of $\epsilon/\Delta x$. When the $\epsilon/\Delta x$ value is small, a larger force over a smaller volume is smeared from the actuator point onto the computational grid. This can result in a more abrupt change in the flow behavior at the region close to the actuator point, which can affect the accuracy of the simulation (see the radial distributions of $\overline{\alpha}$ and $\overline{u}_m/U_\infty$ for $\epsilon/\Delta x = 0.5$). Contrarily, larger values of $\epsilon/\Delta x$ apply a smaller force over a larger volume that results in a smoother distribution of the velocity in the radial direction. For both the angle of attack and normalized longitudinal velocity distributions as a function of nondimensional blade length, the WLGL results start to converge and compare fairly well with the BEM data when $\epsilon/\Delta x \geq 2$, with slight differences in the blade root and tip.

Figure 7.11 compares time-averaged power, $\overline{P}$, thrust, $\overline{T}$, and torque, $\overline{Q}$, as a function of $\epsilon/\Delta x$. For smaller $\epsilon/\Delta x$ values, the longitudinal velocity at the actuator point is higher, resulting in a higher angle of attack. A higher angle of attack and speed results in higher lift, thereby significantly increasing the overall power and torque produced by the wind turbine if the blade section is stalled. As for the normalized velocity distribution, time-averaged power, thrust, and torque converges to a given value when $\epsilon/\Delta x \geq 2$. No remarkable change was observed in thrust generation. The relative differences between the WLGL estimates and BEM results for time-averaged power, thrust, and torque are

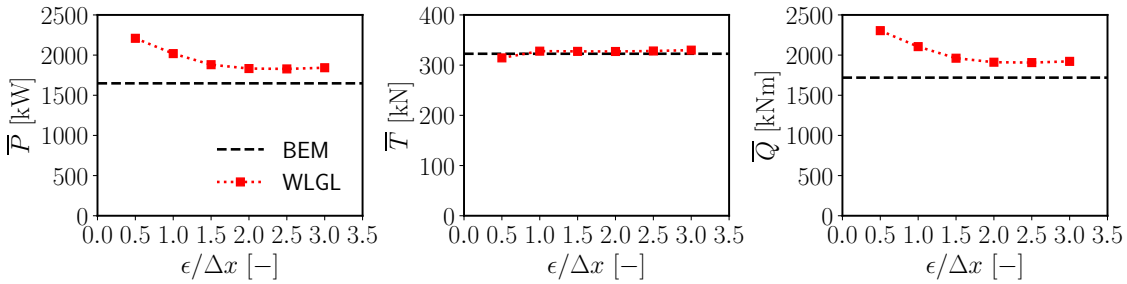

Figure 7.11: Comparison of time-averaged power, $\overline{P}$, thrust, $\overline{T}$, and torque, $\overline{Q}$, as a function of $\epsilon/\Delta x$. All simulations were performed for a freestream wind speed of $U_\infty = 8$ m s^{-1} for a constant inflow.

summarized in Table 7.2.

Correction of aerodynamic coefficients of airfoils to account for 3D effects

Aerodynamic coefficients utilized in aeroelastic simulations of wind turbines (WTs) are often acquired through two-dimensional tests conducted in wind tunnels or from computational analyses. However, the flow over the blades, particularly at the root region, is predominantly three-dimensional, resulting in notable differences in the lift coefficient of a blade section when operating in two-dimensional flow conditions (with flow velocity confined in the blade element plane) versus when it is subjected to flow with a velocity component along the blade span. One well-known consequence of these three-dimensional effects is the "rotational augmentation" observed at the blade root sections. These regions experience a significant increase in the lift coefficient for the same angles of attack when Coriolis forces (arising from blade rotation and flow velocity) induce a spanwise flow velocity component within the boundary layer of the blade [13]. Three-dimensional effects can significantly alter the aerodynamic performance of the airfoil, resulting in inaccuracies in the predicted drag, lift, and other characteristics if the functions of the aerodynamic coefficients versus angle of attack, determined in two-dimensional conditions are not properly corrected to account for three-dimensional effects.

One way to take into account these three dimensional effects in the aerodynamic coefficients is to use simple empirical correction methods based on wind tunnel experiments. These methods typically involve adding or modifying geometric features of the airfoil. These simple three-dimensional airfoil correction models increase the lift near the blade root to account for unique flow conditions occurring in the blade root region, as explained

Table 7.2: Relative differences between the WLGL model results (obtained from time-series saved every 10 s during 10-min simulation) and BEM data.

Parameter	$\epsilon/\Delta x = 0.5$	$\epsilon/\Delta x = 1.0$	$\epsilon/\Delta x = 1.5$	$\epsilon/\Delta x = 2.0$	$\epsilon/\Delta x = 2.5$	$\epsilon/\Delta x = 3.0$
$\mathbb{E}_{\overline{P}}$ [%]	34.016	22.447	14.074	11.167	10.892	11.781
$\mathbb{E}_{\overline{T}}$ [%]	2.542	1.613	1.478	1.407	1.712	2.238
$\mathbb{E}_{\overline{Q}}$ [%]	34.019	22.450	14.076	11.170	10.894	11.784

previously.

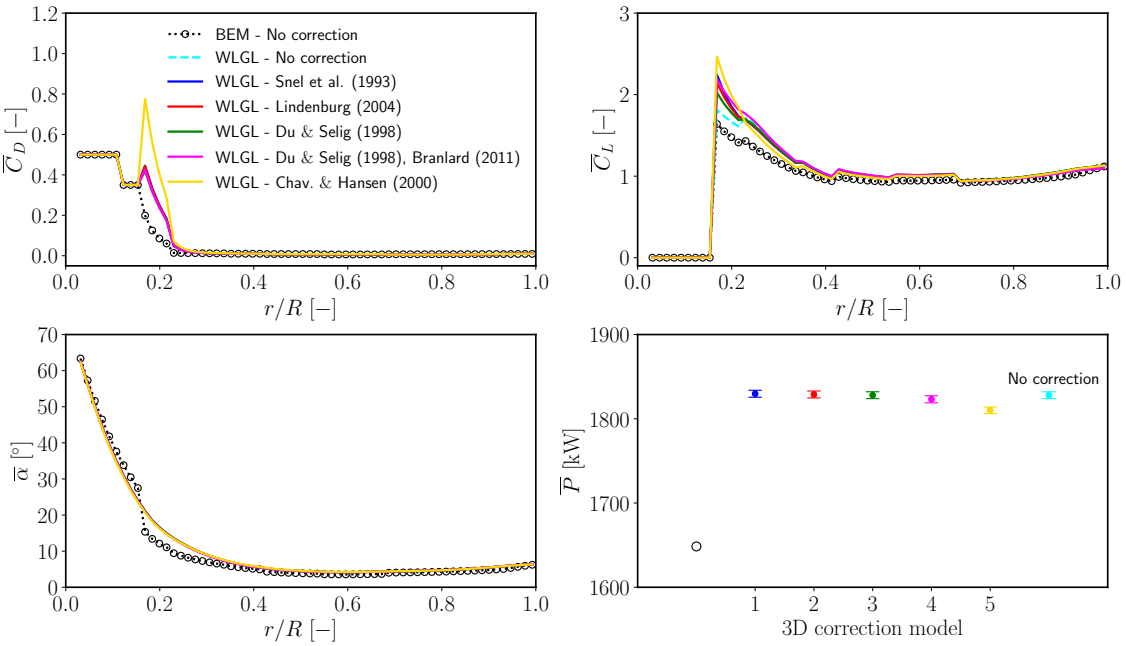

Figure 7.12: Comparison of time-averaged drag (upper left) and lift (upper right) coefficient, angle of attack, $\overline{\alpha}$, (lower left) as a function of nondimensional blade span, r/R, and power estimations of the WLGL model using different 3D airfoil correction models (lower right). All simulations were performed for a freestream wind speed of $U_\infty = 8$ m s^{-1} for a constant inflow. (●): Snel (model #1), (●): Lindenburg (model #2), (●): Du & Selig (model #3), (●): Du, Selig, & Branlard (model #4), and (●): Chav. & Hansen (model #5). (○): BEM without correction and (●): WLGL without correction.

Figure 7.12 compares time-averaged drag, $\overline{C}_D$, and lift, $\overline{C}_L$, coefficients, angle of attack as a function of nondimensional blade span, r/R, and power, $\overline{P}$, estimations of the WLGL model using different 3D airfoil correction models. Here, $\overline{C}_D$, and lift, $\overline{C}_L$, are defined as follows:

$$\overline{C}_D = \frac{\overline{D}}{0.5\rho U_\infty^2 c}, \quad \text{and} \quad \overline{C}_L = \frac{\overline{L}}{0.5\rho U_\infty^2 c}, \tag{7.4}$$

where $\overline{D}$ and $\overline{L}$ are the mean drag and lift per unit length, respectively.

In the present study, 3D airfoil correction model proposed by Chaviaropoulos and Hansen [46] overestimates the drag and lift coefficients compared to other model results and reference BEM data at approximately $r/R = 0.2$, while producing the least power output, resulting in the lowest relative difference with respect to BEM results. None of these models influence the radial distribution of the angle of attack. It is essential to highlight that reaching a definitive conclusion regarding the best-performing model is challenging without comparable experimental data.

7.1.4 Conclusions

The ability of the WLGD and WLGL models to reproduce the wind turbine wake aerodynamics for a case with constant inflow conditions has been thoroughly evaluated by

comparing the estimations of both models with the results from four different large-eddy simulation research codes. A similar trend was observed for the local angle of attack, longitudinal velocity component, lift and drag forces along the blade, and longitudinal velocity and Reynolds stress tensor components in the near wake. For the far wake, noticeable differences were observed in the longitudinal velocity and Reynolds stress tensor components (in both the color maps in the x-z plane and vertical profiles at several distances downstream of the wind turbine) due to model sensitivity to numerical discretization utilized by all the codes tested in this work. Model-to-model comparison has shown that all the research codes using a generalized actuator line model reproduce similar results in the constant inflow case analyzed herein. Likewise, the WLGD model can also estimate similar longitudinal wake velocity and variance fields in the near wake, with very minor differences in the rotor plane as a consequence of the non-rotating blade parameterization approach employed by the WLGD model. The main difference across all the codes was observed approximately further that 7-8D downstream positions where flow turbulence becomes evident. The LES codes based on higher-order numerical schemes predicted the appearance of intense turbulence in wake positions closer to the rotor plane.

Finally, parametric analysis on the effect on the numerical predictions of the aerodynamic force smearing function, both Gaussian and polynomial, regularization kernel width, ϵ, blade root/tip correction function and 3D airfoil correction algorithm, has been done using the same inflow conditions described previously used for the simulation of the NREL 5MW reference wind turbine. Since the smearing polynomial function is designed to provide similar accuracy to the Gaussian function, it has been found that the WT power and thrust estimates do not depend on the type of aerodynamic force smearing function used.

The selection of the proper regularization kernel width is of crucial importance, as it has a significant influence on the spatial force distribution, and on the predictions of the WT power and thrust, as well as on the radial distributions of velocity in the rotor plane. The value of ϵ also influences the shape of the wake downstream of the rotor, especially after $x/D > 7$ where it becomes intensely turbulent. Similar results were obtained in line with the findings reported in the literature [207, 238]. However, a more comprehensive sensitivity analysis, including turbulent flow conditions, is still required before choosing the best-case setup.

The models used to correct airfoil aerodynamic coefficients to account for three-dimensional flow effects analyzed herein are only compared to the BEM results to give an insight into how these models behave when combined with the WLGL model. It has been found that some of the correction models, like the Chav. & Hansen model [46], largely overpredicts the BEM data at the blade root in terms of drag and lift. No significant difference was found among these models in terms of angle of attack distribution along the blade and WT power output.

7.2 Case 2: Validation against field data - Lillgrund wind farm

The WLGD has been validated using experimental data from the Lillgrund offshore wind farm (WF). This WF was chosen due to the availability of wind turbine design data and experimental data. Although the simulation of an offshore wind farm is beyond the scope of this dissertation, it is included in the validation analysis of the WLGD model to provide a more comprehensive evaluation study of the capabilities of the WLGD model when simulating multiple wind turbines reproducing the wind turbine-ABL flow interaction and the effect of upstream wind turbines on the power generation of downstream wind turbines. The grid resolution used in this case does not allow the use of WLGL model, as it requires much finer grid resolutions.

7.2.1 Definition of the Lillgrund WF test case

Lillgrund wind farm consists of 48 Siemens SWT-2.3-93 wind turbines, each with a rated power output of 2.3 MW, and is located south of the Öresund Bridge, between Denmark and Sweden. The wind turbines have a diameter of $D = 93$ m and a hub height of $z_{hub} = 65$ m, with a rated wind speed of about $U_R \approx 12$ m s^{-1}. The location of the Lillgrund WF and WT layout are shown in Figure 7.13. This WF is densely packed, as the smallest WT spacing is $3.3D$, while the largest WT spacing is $4.3D$ in certain wind directions. This layout makes the WF efficiency poor compared to other WFs, such as the Horns Rev WF [239]. The shallow water at a specific location inside the Lillgrund WF made unfeasible the installation of two wind turbines in Row E.

Based on meteorological data collected from a met mast located southwest of the WF using cup anemometers mounted at different heights, and temperature sensors, the average atmospheric stability was considered neutral, as an equal distribution of stable and unstable observations for the southern sector of the WF was found in earlier studies [239]. The measured power data used for comparison have been reproduced from the same reference paper of Nilsson et al. [239]. In order to save computational overhead, only one case with a mean horizontal wind speed of $\overline{U}_{hub} = 8$ m s^{-1} and a mean wind direction of $\overline{\beta}_{hub} = 120 \pm 2.5°$ at hub height was simulated. The same strategy for calculation of mean turbulence intensity, $\overline{TI}$, that is

$$\overline{TI} = \frac{\sigma_{U_{hub}}}{\overline{U}_{hub}}, \tag{7.5}$$

where $\sigma_{U_{hub}}$ is the standard deviation of the horizontal wind speed at hub height.

The wind farm's performance can be evaluated through the calculation of array efficiency,

This section relies on a part of the content of an extended abstract that has been presented at an international conference:

- Kale, B., Buckingham, S., van Beeck, J. and Cuerva-Tejero, A., 2021. Multiscale wind turbine wake modeling within a wind farm using the WRF-LES model: An application to the Lillgrund offshore wind farm. *Wind Energy Science Conference 2021*, Hannover, Germany, 25-28 May 2021 (online).

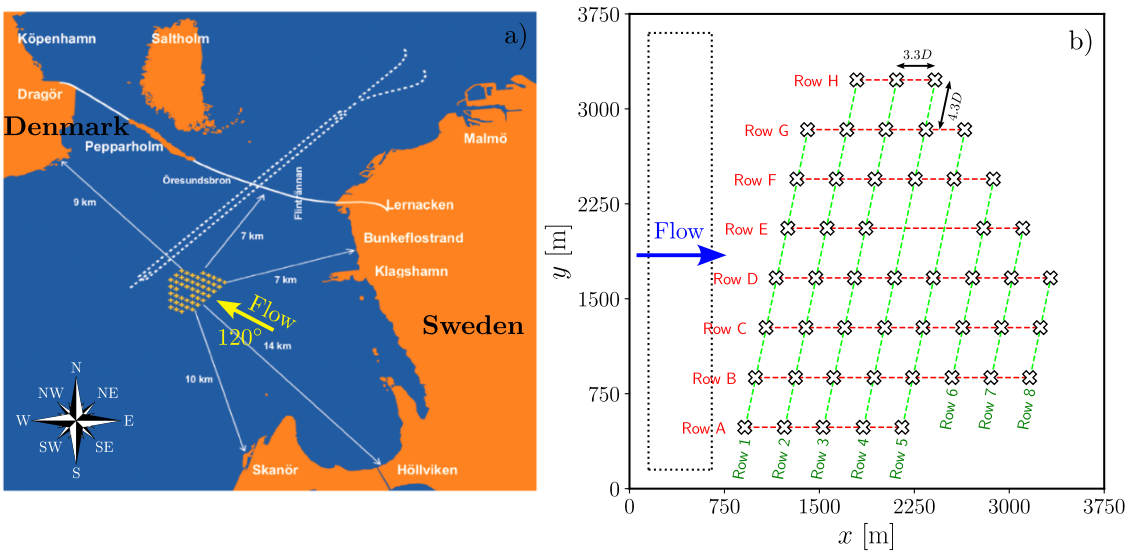

Figure 7.13: Location (a) and layout (b) of the Lillgrund wind farm. Crosses denote 48 SWT-2.3-93 wind turbines, whereas dashed red and green lines depict rows from 1 to 8 and A to B, respectively. The rectangle region indicated by dotted black lines represents the inflow region where wind flow characteristics are determined. D refers to the rotor diameter. Wind flow originates from the left-hand side of the domain. The image on the left-hand side has been reproduced from Creech et al. [63].

η_{array}. This efficiency is calculated as the ratio between the total power output of the entire WF and a mean reference power value, which is then multiplied by the number of WTs in the array, N_t. η_{array} is defined as follows:

$$\eta_{\text{array}} = \frac{\sum_{n=1}^{N_t} P_n}{N_t \overline{P}_{\text{ref}}}. \tag{7.6}$$

In Equation (7.6), the instantaneous power output of the n^{th} WT, denoted as P_n, is directly acquired from the WLGD model's 1-min outputs. Meanwhile, the mean reference power, symbolized as $\overline{P}_{\text{ref}}$, is calculated based on the average power output of WTs that remain unaffected by wake losses as simulated by the WLGD model. In this study, these wind turbines are identified as the WTs from the upstream row (Row 1). Therefore, $N_t\overline{P}_{\text{ref}}$ represents the wind farm's potential power output under the given wind conditions without any losses [288].

7.2.2 Numerical set-up

An idealized WLGD simulation to model the interaction between the ABL flow and a wind farm was performed by using two domains, based on a one-way nesting strategy. The surface kinematic heat flux, $Q_s = (\overline{w'\theta'})_s$, was set to $Q_s = 0$ to model pure neutral ABL flow through the wind farm. Temporal discretization was achieved by a third-order Runge–Kutta scheme, whereas the horizontal and vertical advection schemes were based on fifth- and third-order finite difference approximations, respectively. The SFS closure

was achieved using the first-order Smagorinsky SFS model.

The simulation was initialized using dry atmospheric conditions without radiation, cloud, or land-surface models. The initial capping inversion was created by specifying the initial potential temperature field to be 300 K up to 500 m above the surface. From 500 m to 800 m, temperature increases by 8 K. Above 800 m, the potential temperature increases at a rate of 0.005 K m^{-1}. This potential temperature profile is similar to that used by Moeng and Sullivan [224] for modeling of a neutral ABL. A uniform geostrophic wind profile, with longitudinal and lateral components of $U_{g1} = 8.65$ m s^{-1} and $U_{g2} = -0.81$ m s^{-1}, respectively, was applied up to the model top. A Rayleigh damping layer with a coefficient of 0.003 s^{-1} was utilized in the upper part of the inversion layer to damp out spurious vertical motions. In order to trigger turbulence, small perturbations of $[-0.5, +0.5]$ K, obtained from a pseudo-random uniform distribution decreasing as a cubic function of height, were added to the initial values of potential temperature, below capping inversion [204, 219]. The MOST was used to account for the fluxes of momentum and heat [227] in the surface layer. The Revised MM5 Monin–Obukhov scheme [145] was used to parameterize surface fluxes. No wind-wave interaction was considered; hence, sea surface waves were not modeled. Instead, the model surface was considered as a flat rough wall with an aerodynamic roughness length of $z_0 = 0.0001$ m, which is appropriate for representing the sea surface [55].

In the WLGD simulation, for the coarse domain, grid resolution in horizontal space was set to $\Delta x = \Delta y = 30$ m. Vertical grid spacing was set to, $\Delta z \approx 10$, in the first 200 m above the surface, and beyond, it was stretched up to the model top. For the nested domain, the horizontal grid spacing was set to $\Delta x = \Delta y = 10$ m. The coarse domain size is 6 km, whereas the nested domain size is 3.75 km, in both horizontal directions. Both domains use the same grid spacing in the vertical direction up to the model top placed at $\sim$1.25 km. The coarse domain consists of $201 \times 201 \times 61$ grid points, while the nested domain has $376 \times 376 \times 61$ grid points in the longitudinal, lateral and vertical directions, respectively. The model time step for the coarser domain was set to 0.2 s and a time step ratio of 3 was employed for the nested domain.

Periodic boundary conditions were prescribed on the boundaries of the parent domain, with open boundary conditions on the child domain. The coarser domain was spun up for several hours to reach a quasi-equilibrium state based on the prescribed geostrophic wind. After a uniform flow solution was achieved in the x-y plane across the domain, the WLGD model was activated on the finer domain. Time series of different flow variables and wind turbine outputs were recorded every 1-min. The nested domain with the wind turbine model was turned on at the beginning of hour 15 h, and run for 1 h and 10-min. The first 10-min of the nested domain simulation were relegated to make sure that turbulence was well developed in the finer domain. Inflow wind speed and wind direction at hub height, for wind turbine control purposes, were obtained at one rotor diameter upstream of the wind turbine rotor, based on running time averages of the instantaneous velocity components. The averaging interval consists of 4320 data points.

Regarding wind turbine modeling, the generic SWT-2.3-93 WT model was used since the geometry and airfoil data for the actual Siemens WT are not public. The aerodynamic effects of the nacelle and tower, as well as control mechanisms for generator speed and blade pitch, were also included. In order to simplify the numerical set-up, the layout of the Lillgrund WF was rotated $\sim$150° clockwise so as to align the westerly ABL flow with the entire WF.

In order to smear out local aerodynamic loads computed by the WLGD model onto the computational grid, a Gaussian function was used and the resulting body forces were added to the momentum equations of LES. A regularization kernel, ϵ, that is related to the grid size as $\epsilon = 2\Delta x$, was used. The chord and twist angle, as a function of blade radius, were linearly interpolated using tabulated airfoil data. A total of 45 actuator points with 30 fixed lines were used to represent the WT rotor and blades. Prandtl's root and tip loss corrections were used to account for the infinite number of blades in the WLGD model. Tilted rotor shaft and coned blade configuration were considered. A constant air density of $\rho = 1.225$ kg m^{-3} was used to calculate the power produced by each wind turbine.

7.2.3 Results

Figure 7.14 shows mean vertical profiles of horizontal wind speed, $\langle\overline{U}\rangle$, wind direction, $\langle\overline{\beta}\rangle$, turbulence intensity, $\langle\overline{TI}\rangle$, and potential temperature, $\langle\overline{\theta}\rangle$, obtained from the WLGD model simulation for neutral ABL conditions. A spatio-temporal averaging in time and horizontal space, denoted by $\overline{\langle\cdot\rangle}$, was applied to determine these vertical profiles in a region represented by dashed lines as shown in Figure 7.13b. No experimental data are available to compare the modeled and observed inflow conditions. The magnitudes of modeled quantities at hub height are: $\langle\overline{U}_{hub}\rangle = 8.3$ m s^{-1}, $\langle\overline{\beta}_{hub}\rangle = 269.3°$, $\langle\overline{TI}_{hub}\rangle = 0.052$ and $\langle\overline{\theta}\rangle = 301.2$ K. The bias error between the modeled and observed horizontal wind speed reported in Nilsson et al. [239] for the sector $120° \pm 2.5°$ is 3.75%. The difference between the desired and simulated wind direction is -0.26%. Since the conditions in the free atmosphere are assumed to be non-turbulent, all atmospheric variables in the vertical profiles return to their initial conditions above $z/z_i = 1$.

Figure 7.15 shows the time-averaged contour plots of normalized horizontal velocity, $\overline{U}_{hub}/\langle\overline{U}_{hub}\rangle$, turbulence intensity, $\overline{TI}_{hub}$, the longitudinal component of the Reynolds stress, $(\overline{u'u'})_{hub}/\langle\overline{U}^2_{hub}\rangle$, and kinematic shear stress, $(\overline{u'w'})_{hub}/\langle\overline{U}^2_{hub}\rangle$, at hub height. $\langle\overline{U}_{hub}\rangle$ is the hub height horizontal wind speed averaged in time and horizontal space. The Lillgrund WF is a compact wind farm with relatively smaller distances between the WTs, and thus the wakes produced by the front WTs strongly affect the rotational speed of downwind WTs since there is not enough distance for the wake to recover (typically $10D$, depending on the state of the ABL) before reaching the next wind turbine. Lower wake velocity regions were observed behind the second row (Row 2) wind turbines due to larger momentum extraction from the wind flow compared to results from other rows. This is also visible in contour plots of $\overline{TI}_{hub}$ and $(\overline{u'u'})_{hub}/\langle\overline{U}^2_{hub}\rangle$ because of enhanced turbulence mixing. The increase in turbulence intensity could potentially have adverse effects associ-

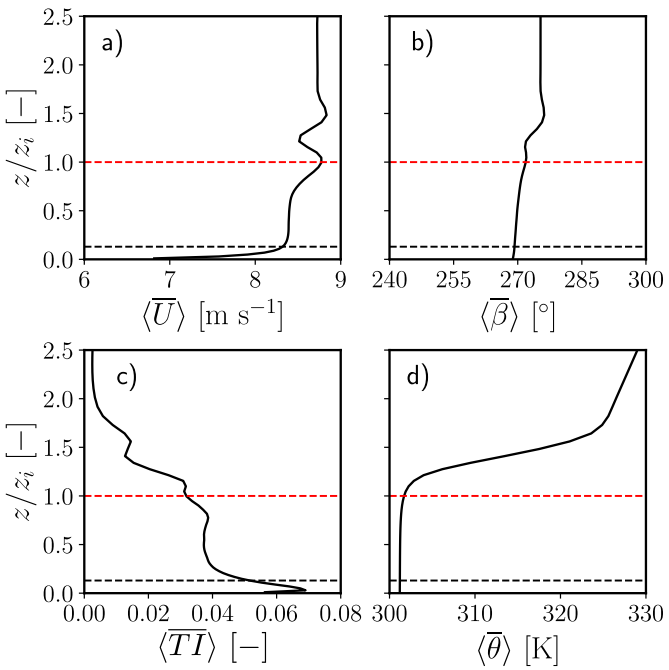

Figure 7.14: Mean vertical profiles of horizontal wind speed, $\langle\overline{U}\rangle$, (a), wind direction, $\langle\overline{\beta}\rangle$, (b), turbulence intensity, $\langle\overline{TI}\rangle$, (c), and potential temperature, $\langle\overline{\theta}\rangle$, (d). (- - -) denotes the ABL height, z_i, (i.e., inversion height), whereas (- - -) refers to hub height, $z_{hub} = 65$ m. These vertical profiles were obtained by applying a spatio-temporal averaging in a region represented by dashed lines shown in Figure 7.13b. $\langle\cdot\rangle$ denotes spatial averaging in time and horizontal space.

ated with unexpected intermittent stops of WTs due to lower wind speeds and increased fatigue loads. These negative effects are also evident in contour plots of $(\overline{u'w'})_{hub}/\langle\overline{U}^2_{hub}\rangle$, especially for the WTs further downstream ($x > 1500$) m. It should be noted that the gap in the Lillgrund WF positively influences the first WT downstream of the gap, as this gap helps recover the wake before it reaches the downstream WT.

Figure 7.16 compares the WLGD model estimations of power production with the available LES results and experimental data reported in Nilsson et al. [239]. The power generated by each WT was averaged in time and normalized by the median of the power production of the front-row WTs. A particular discrepancy exists for all wind turbines in Rows 2 and 3, resulting in underestimations of the power output. Overall, the agreement between WLGD estimates, LES results, and measured data is quite good. However, some WTs, particularly those in the second row, stopped intermittently due to lower wind speeds determined at one rotor diameter upstream. This was less pronounced for the third-row WTs because the wake from the front-row WTs recovered before reaching the third-row WTs when the second-row WTs stopped. These downstream WTs encounter wakes in which the greatest amount of meandering was observed.

Figure 7.17 illustrates the ratio between the time-averaged power produced by each turbine and the total time-averaged power production of all the WTs in the plant (i.e., fractional contribution of each turbine to total power). Each WT at the front of a wind-aligned row

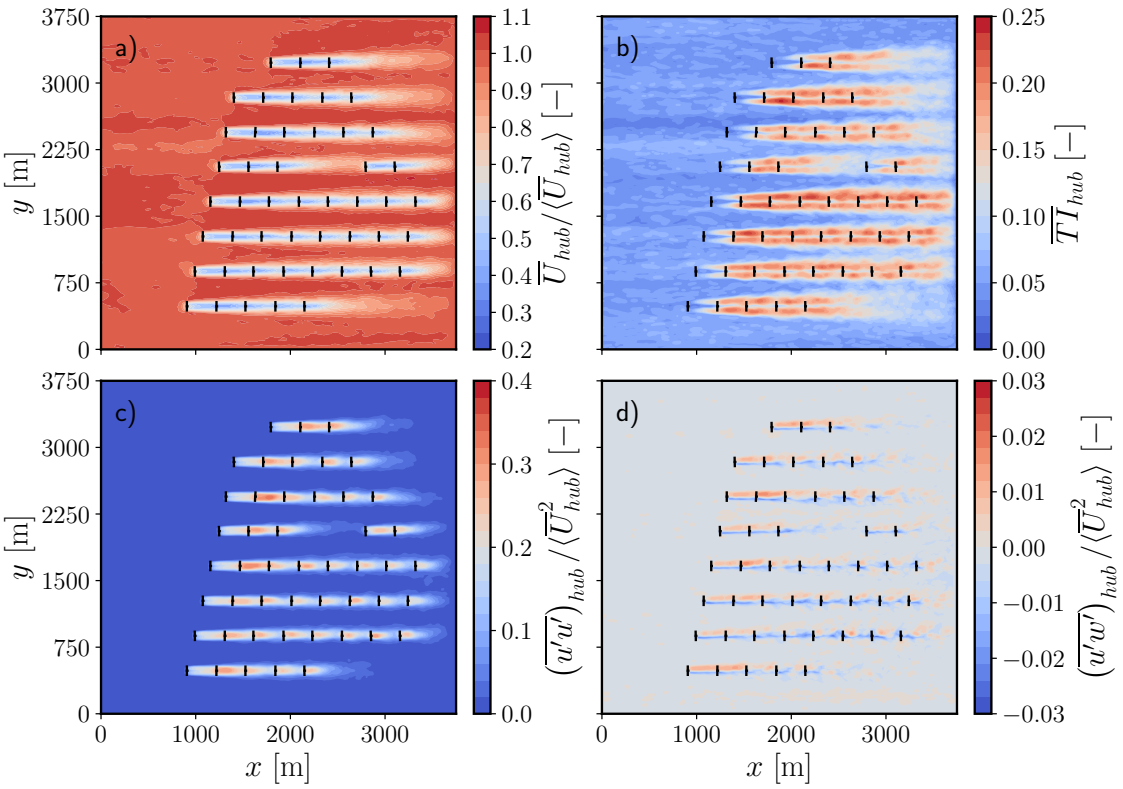

Figure 7.15: Time-averaged contour plots of normalized horizontal velocity, $\overline{U}_{hub}/\langle\overline{U}_{hub}\rangle$, (a), turbulence intensity, $\overline{TI}_{hub}$, (b), the longitudinal component of the Reynolds stress, $(\overline{u'u'})_{hub}/\langle\overline{U}^2_{hub}\rangle$, (c), and kinematic shear stress, $(\overline{u'w'})_{hub}/\langle\overline{U}^2_{hub}\rangle$, (d) at hub height. $\langle\overline{U}_{hub}\rangle$ is the hub height horizontal wind speed averaged in time and horizontal space. (——) indicates the location of the wind turbine rotor. Wind flow originates from the left-hand side of the domain.

produces 4.75-5% of the total power, whereas downstream WTs produce 0.5-3.5% of the total power, with the lowest power production of about 0.5-1% in the second row. The WT, located just behind the omitted WTs, produces about 4% of the total power, which is the second highest contribution to the total power. Similar findings were also obtained in Churchfield et al. [55].

The simulated array efficiency, denoted as $\eta^{\text{WLGD}}_{\text{array}}$, calculated as the ratio between the power output of the entire wind farm and the reference power multiplied by the number of WTs in the array, is 13.4% lower than the array efficiency reported by the SCADA system for wind speeds in the range of $6 \leq U_\infty \leq 12$ m s^{-1} ($\eta^{\text{SCADA}}_{\text{array}} = 0.439 \pm 0.005$) [288].

7.2.4 Conclusions

The validation of the WLGD model for power production is based on LES data from the Lillgrund offshore WF, which comprises 48 Siemens SWT-2.3-93 wind turbines, operating under inflow conditions with sectors of $120 \pm 2.5°$. This is an important step to validate the WLGD model, as it includes not only the ABL flow-WT interaction but also the effect of the wake generated by the upstream wind turbines on downstream WTs. The

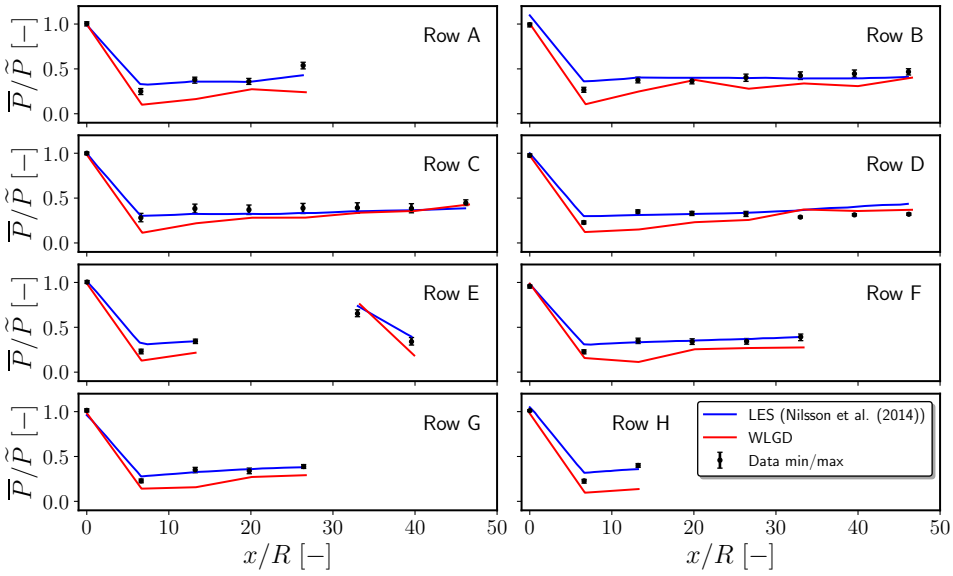

Figure 7.16: Comparison of normalized power, $\overline{P}/\widetilde{P}$, for the inflow angle sector of $120° \pm 2.5°$ and $\overline{U}_{hub} \approx 8$ m s^{-1}, estimated by the WLGD model with LES results and experimental data reported in Nilsson et al. [239]. The mean power production, $\overline{P}$, is normalized by the median of the power production of the front row WTs, $\widetilde{P}$.

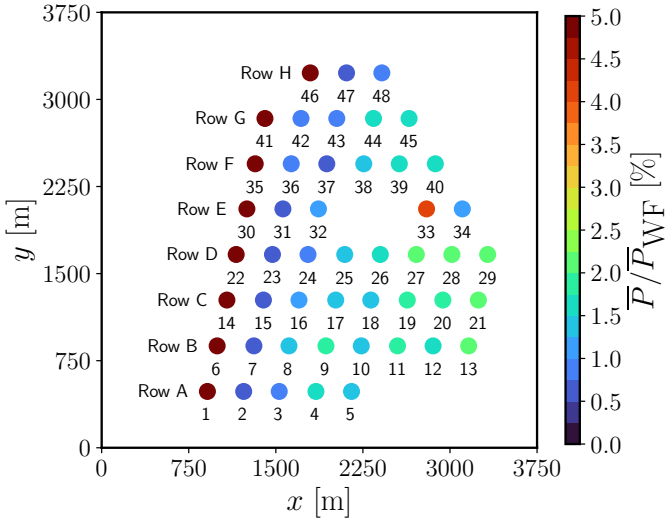

Figure 7.17: An overview of each WT's mean power production, showing the fractional contribution of each WT to the entire WF power production. The numbers, from 1 to 48, indicate the WTs. Wind flow originates from the left.

estimated $\overline{TI}$ level at hub height, which is $\overline{TI}_{hub} = 5.2\%$, is consistent with the measured $\overline{TI}_{hub}$ level, that is $\overline{TI} = 5.7\%$, for the wind sector simulated herein. The results show a quite good agreement with the normalized power production for Rows A-H. The fractional contribution of each turbine to the total power produced by the wind farm shows that the wind turbines located just behind the front row turbines, that are Turbines $2, 7, 15, 23, 31, 36, 42$, and 47, produce the lowest power due to the lower inflow wind velocity and increased turbulence intensity induced by the front row turbines. The spatial gap in the middle of the Lillgrund wind farm allowed the wake from the Turbine 32 to

be recovered before reaching Turbine 33. This means that when the winds are blowing at moderate speeds and perpendicular to the wind turbines, the distance between the wind turbines is not sufficient to completely dissipate the wind turbine wakes before they reach the wind turbines downstream.

By incorporating a simulation of an offshore wind farm, the validation study of the WLGD model addresses a broader range of scenarios to help increase the reliability of model predictions. Additionally, it can provide insights into the performance of the WLGD model in more complex and realistic environments, which can be helpful for future applications of both WLGD and WLGL models when modeling large wind farm flows in realistic atmospheric conditions.

7.3 Case 3: Validation against measurements and LES results under varying ABL stability conditions in flat terrain

To validate both the WLGD and WLGL models under varying atmospheric stability conditions against available LES data and field measurements, a series of idealized large-eddy simulations were performed in turbulent inflow conditions. The performance of Vestas V27 WT has been evaluated paying attention to the wind turbine wake behavior and the aerodynamic performance. Spatial distributions of mean velocity components, their variances, and instantaneous vorticity in the wake of the wind turbine are analyzed by comparing the results from WLGD and WLGL approaches [155]. Results of the wake velocity deficit profiles and wind turbine aerodynamic response have been compared with the experimental ones obtained in the Scaled Wind Farm Technology campaign and available LES data reported in the works of Doubrawa et al. [80] and Jézéquel et al. [142]. The WLGD and WLGL models have been renamed to GAD and GAL for simplicity and clarity. The term WRF-LES encompasses the inflow results from the two models, as both models use the same inflow field.

7.3.1 Measurement campaign: the SWiFT benchmarks

The Scaled Wind Farm Technology (SWiFT) facility [80] located in Lubbock, Texas, USA, is a research-scale wind turbine test center, which consists of two 60 m meteorological masts (hereinafter referred to as met masts) and three horizontal axis wind turbines that are modified versions of the Vestas V27 variable-speed and variable-pitch wind turbine, with a rotor diameter $D = 27$ m and hub height $z_{hub} = 32.1$ m (see Table 7.3). The SWiFT test site is located in flat terrain and is therefore exempt from complex terrain effects (e.g., uniform surface cover) and provides researchers a unique opportunity to validate their numerical simulations in realistic turbulent flows, such as wind turbine wakes under varying atmospheric thermal stratification conditions. Atmospheric stability

Table 7.3: Characteristics of the modified Vestas V27 wind turbine.

Parameter	Hub height	Rotor shaft tilt	Rotor diameter	Wind turbine base elevation	Wind turbine location	Rated power	Power converter	Pitch control
Value	32.1 m	4.05°	27 m	1018 m	33.60795°N, 102.04862°W	225 kW, at 43 RPM	Variable speed, full conversion	Collective

This section relies on the content of two articles that have been published in a peer-reviewed international journal:

- Kale, B., Buckingham, S., van Beeck, J. and Cuerva-Tejero, A., 2022. Implementation of a generalized actuator disk model into WRF v4.3: A validation study for a real-scale wind turbine. *Renewable Energy*, 197, pp. 810-827. DOI: 10.1016/j.renene.2022.07.119.
- Kale, B., Buckingham, S., van Beeck, J. and Cuerva-Tejero, A., 2023. Comparison of the wake characteristics and aerodynamic response of a wind turbine under varying atmospheric conditions using WRF-LES-GAD and WRF-LES-GAL wind turbine models. *Renewable Energy*, 216, p. 119051. DOI: 10.1016/j.renene.2023.119051.

effects become the main driver in the absence of severe weather events such as heavy precipitation, storm, wet-snow icing, and so on. The flatness of the land in the field can be considered as an advantage in terms of reducing the impact of topography and heterogeneous surface cover on the flow.

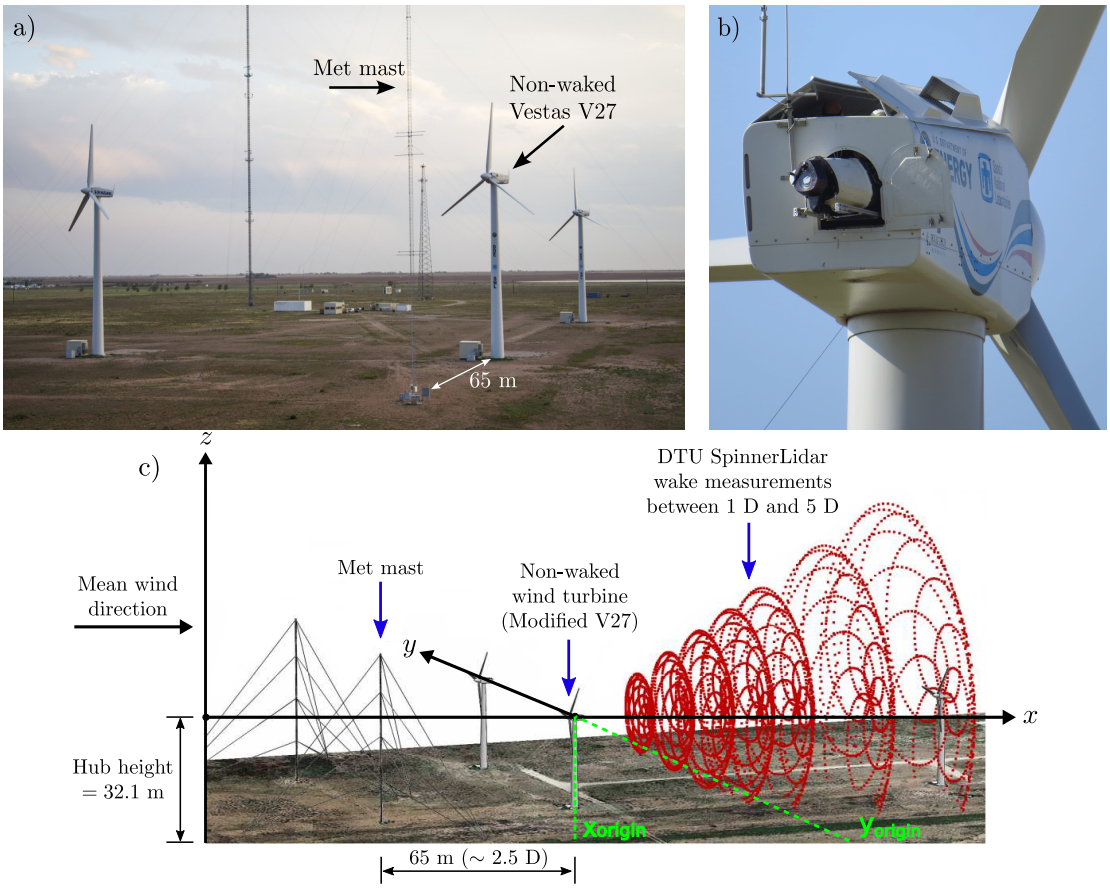

Figure 7.18: The SWiFT facility with three Vestas V27 wind turbines and two 60 m meteorological masts [115] (a) and the rear-facing Technical University of Denmark's (DTU's) SpinnerLidar [216] mounted at the back of the non-waked Vestas V27 wind turbine's nacelle [100] (b), the schematic of the SWiFT facility, showing the three V27 wind turbines, the meteorological towers located south of the wind turbines and one of the DTU SpinnerLidar scanning strategies used for the SWiFT benchmarks [80]. x_{origin} and y_{origin} refer to wind turbine hub location in x and y directions, respectively (c).

The measurements were performed on the southeastern wind turbine (see Figure 7.18a) equipped with a rear-facing, nacelle-mounted lidar (see Figure 7.18b). Wind turbine operation is monitored by multiple sensors placed at the back of the nacelle, measuring wind speed, wind direction, yaw offset, generator power and torque, and blade pitch.

A DTU SpinnerLidar [216] was used to track the wind turbine wake, starting from $2D$ to $5D$ downstream of the wind turbine rotor, for neutral and stable conditions, yet it was limited to $3D$ under unstable conditions. Since investigating the spatial evolution of the wind turbine wake for the neutral and stable cases was the primary objective of these measurements, the lidar sampling period was set to approximately 30-42 s. However, it was reduced to 2 s for the unstable case to resolve the dynamic behavior of the wind turbine

wake flow (e.g., wake meandering). More details can be found in the study by Doubrawa et al. [80]. It was assumed in the in-situ measurements that the beam elevation angle is zero, and the angle between the upcoming wind and rotor axis is approximately zero, meaning that the rotor is always aligned with the upstream flow. As stated by Doubrawa et al. [80], lidar scans return line-of-sight velocity measurements at 984 points in a rosette pattern at a desired downstream location. The origin of the coordinate system was placed onto the nacelle in a fixed frame of reference (FFOR) (see Figure 7.18c for details). In the reference paper, most of the analysis is performed in the FFOR rather than a meandering frame of reference (MFOR), thus the current work compares the WLGD and WLGL results in the FFOR with the corresponding measurement and available LES data.

Several flow characteristics such as mean horizontal wind speed, wind direction, and turbulence intensity at hub height, atmospheric stability parameter, and friction velocity, estimated from uv and vw covariances at 10 m, as well as near-surface kinematic heat flux at 2 m, were determined from the experimental database (see Table 7.4). These parameters were obtained from measurements taken at the 60 m met mast, which is located 65 m upwind of the wind turbine. Ensemble averages of time-averaged field measurements, which were collected from the met mast and sampled at a frequency of 1 Hz over 10-min periods, for neutral, unstable, and stable cases defined in the SWiFT campaign are provided as inflow conditions in Table 7.5. Ensemble averages of six time-averages were used for the neutral and stable cases, and of five ones for the unstable case.

In order to properly reproduce inflow conditions for all cases, the simulated turbulent inflow is calibrated against measurements taken from the met mast (see Figure 7.18a). The comparison is done based on the laterally- and temporally-averaged inflow quantities determined at hub height at freestream. The compared parameters are the horizontal wind speed, $\langle\overline{U}\rangle$, wind direction, $\langle\overline{\beta}\rangle$, and turbulence kinetic energy (TKE), $\langle\overline{e}\rangle = \frac{1}{2}(\sigma_u^2 + \sigma_v^2 + \sigma_w^2)$. In addition, other relevant parameters determined at freestream, like turbulence intensity, $\overline{TI}_{hub} = \sigma_{U_{hub}}/\overline{U}_{hub}$, at hub height, surface kinematic heat flux, $\overline{Q}_s$, at 2 m, and atmospheric stability parameter, $\zeta = z/L$, at 10 m were analyzed for a comprehensive validation of the simulated atmospheric inflow. Here, $\sigma_{U_{hub}}$ is the standard deviation of horizontal wind speed at hub height, $\overline{U}_{hub}$ is the mean horizontal wind speed at hub height, and L is the Obukhov length. This work utilizes inflow fields for different ABL conditions generated following the ensemble-averaged measurement data determined in the SWiFT campaign.

One of the main purposes of this study is to assess the real-world atmospheric forcing

Table 7.4: Locations of the sensors mounted on a 60 m meteorological mast.

Sensor	Sonic anemometer	Cup anemometer	Wind vane	Barometric pressure	Relative humidity	Air temperature
Height above ground level [m]	10, 18, 32, 45 and 58	18, 31.5, and 45	29.5	2.5 and 30	2.5, 30, and 56.5	2.5, 30, and 56.5

Table 7.5: Ensemble averages of horizontal wind speed, $\overline{U}_{hub}$, and turbulence intensity, $\overline{TI}_{hub}$, at hub height, atmospheric stability parameter, ζ, at 10 m above ground, friction velocity, u_*, surface kinematic heat flux, $\overline{Q}_s$, and virtual potential temperature, $\overline{\theta}_v$, defined for each benchmark at the SWiFT facility [80].

Case studies	$\overline{U}_{hub}$ [m s^{-1}]	$\overline{TI}_{hub} = \sigma_{U_{hub}}/\overline{U}_{hub}$ [%]	$\zeta = z/L$ [-]	u_* [m s^{-1}]	$\overline{Q}_s = (\overline{w'\theta'_v})_s$ [K m s^{-1}]	$\overline{\theta}_v$ [K]
Neutral	8.7	10.7	0.004	0.45	−0.002	314.4
Unstable	6.7	12.6	−0.089	0.33	0.023	290.9
Stable	4.8	3.4	1.151	0.08	−0.005	304.2

(e.g., thermal stratification effects) on the wind turbine's aerodynamic performance. The balance between buoyancy production/destruction and shear production of turbulence kinetic energy plays a vital role in defining the state of the ABL. Although atmospheric stability is generally characterized by the ratio between the ABL height, z_i, and Obukhov length, L, it is sometimes defined as the ratio between the sensor measurement height, z, and the Obukhov length as in [78]. In the current study, $\zeta = z/L$ is used to characterize the state of the atmosphere for each benchmark. The ABL is unstable when ($-2.0 \leq \zeta \leq -0.02$) and stable when ($0.02 < \zeta < 2.0$), whereas it is classified as neutral ($|\zeta| < 0.02$, $\Psi_m(\zeta) = 1$) (where $\Psi_m(\zeta) = (\kappa z/u_*)/(\partial\overline{U}/\partial z)$, z being the height, refers to the universal function of momentum flux), and the logarithmic law of the wall becomes applicable [185, 262, 278].

7.3.2 Model evaluation criteria

The numerical results have been compared with the measurements for a set of inflow parameters, wind turbine response, and velocity deficit in the wake. Besides, spectra of longitudinal, u, and lateral, v, velocity components at hub height, $S_i(f)$, are compared with those obtained from full-scale measurements and other LES code results. Spectra for the measurements were estimated for each 10-min time series from sonic anemometers at hub height and $2.5D$ upstream of the corresponding wind turbine. The standard deviation around the mean ensemble spectra, divided by the square root of the number of data sets, is represented by a gray-shaded region in Figure 7.21. For numerical simulations, spectra of the velocity components are obtained from calculated time series sampled at every 1 s through 3600 s simulations considering the time series of the velocity components measured at 50 points in a y direction transect at hub height. The sampling transect is centered at y_{origin} at the met mast location, and the sampling points are evenly distributed over 100 m (see Figure 7.18). Later, spectra are laterally averaged to yield mean spectra to compare with the measurements. Herein, spectra are obtained using the Welch method with a Hann window that spans over 180 s. To compare the energy content of different spectra, each spectrum is normalized as $S_i(z_{hub}\langle\overline{U}_{hub}\rangle)^{-1}$ and frequencies are presented in nondimensional form as $f(z_{hub}\langle\overline{U}_{hub}\rangle^{-1})$.

Instantaneous velocity deficit profiles, VD, as a function of time and space are computed and normalized by the time-averaged freestream wind speed profile at the met mast loca-

Table 7.6: Configuration parameters for three different case studies simulated in the WRF-LES model.

Benchmark	U_{g1}, U_{g2} [m s^{-1}]	$(\overline{w'\theta'_v})_s$ [K m s^{-1}]	Cooling rate [K h^{-1}]	z_0 [m]	z_i [m]	Inversion strength [K m^{-1}]	Spin-up time [h]
Neutral	11.70, -3.97	-0.002	0.00	0.014	1000	0.010	15
Unstable	7.75, -1.88	0.023	0.00	0.010	1000	0.004	10
Stable	5.00, -2.87	0.000	-0.667	0.010	200	0.010	15

Note. U_{g1} and U_{g2} are geostrophic wind velocity components in the longitudinal and lateral directions, respectively, z_0 is the aerodynamic surface roughness length, and z_i represents the initial inversion height.

tion, $\overline{U}_\infty(z)$, given in Equation (7.7) as follows:

$$VD(x, y, z, t) = \frac{U(x, y, z, t)}{\overline{U}_\infty(z)} - 1, \tag{7.7}$$

where $U(x, y, z, t)$ is the instantaneous horizontal wind speed obtained from longitudinal, u, and lateral, v, wind velocity components. For clarity and consistency, temporally-averaged hub height velocity deficit profiles are taken into account for velocity deficit comparison; in other words, one-dimensional velocity deficit profiles (obtained after spatial averaging) are used to evaluate the reduction in the axial momentum of the air passing through the wind turbine rotor.

With regard to wind turbine response, the overall wind turbine performance is assessed by comparing GAD and GAL results with the available experimental data and LES results by means of generator power, generator torque, and rotor speed. Since aerodynamic thrust was not measured during the field tests, this quantity is only compared with other available LES results reported in the reference paper.

7.3.3 Numerical set-up

In this study, two LES domains were employed, as depicted in Figure 7.19. The coarser domain produced atmospheric turbulence, which was then used as input for the finer domain through a one-way nesting approach. Periodic boundary conditions were applied to the parent domain, while the child domain had open boundary conditions. The coarser domain was spun up for several hours to attain a quasi-equilibrium state, driven by prescribed geostrophic wind and surface forcing. After a uniform flow solution was achieved in the x-y plane across the domain, the wind turbine parameterization was activated on the finer domain. Time series of different flow variables and wind turbine outputs were recorded every 1-min. WRF-LES model set-ups for neutral, unstable, and stable conditions are given in Table 7.6. Domain dimensions for each case are given in Table 7.7.

The stability classes defined in each case are abbreviated as follows: NBL for near-neutral ABL, CBL for slightly convective (i.e., unstable), and SBL for very stable ABL. Hereinafter, each simulation incorporating the GAD and GAL models is identified by combining the wind turbine parameterization type and stability class (e.g., GAD-NBL, GAD-CBL, and GAD-SBL, respectively). Parent and child domains use horizontal resolutions

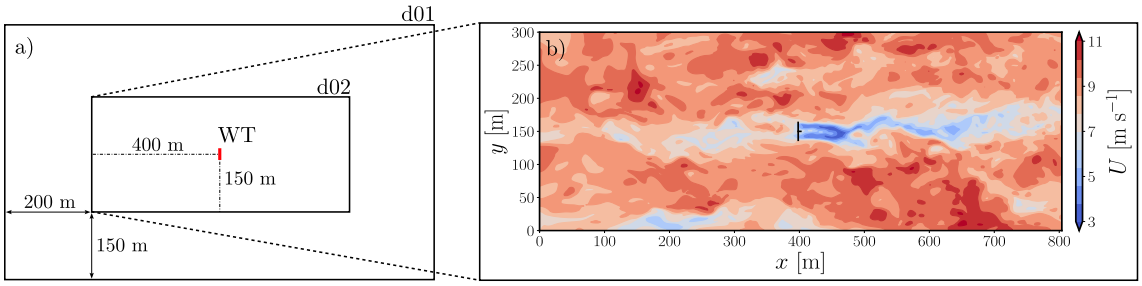

Figure 7.19: A schematic showing the nested domain configuration and location of the wind turbine, indicated by a solid red line (a), a contour plot colored by instantaneous horizontal wind speed at hub height in the horizontal plane from the GAL model, corresponding to a snapshot taken approximately 30-min after initializing the nested domain (b).

of $\Delta x = \Delta y = 6$ m and $\Delta x = \Delta y = 2$ m, respectively. All cases use vertical resolution, Δz, approximately equal to Δx of the nested domain on both domains. For each case, the values of Δz were kept constant up to a height of 60 m and stretched up to the domain top, using a hyperbolic tangential vertical grid stretching algorithm. A zero vertical motion and zero stress boundary conditions were imposed at the model top. A single-layer capping inversion was applied at 1000 m above the ground for NBL and CBL cases, while it was placed at the height of 200 m for the SBL case in order to prevent turbulence from reaching the top boundary [219]. Aerodynamic roughness length, z_0, was set to $z_0 = 0.014$ m for NBL, 0.01 m for CBL and SBL, with a Coriolis forcing of $f_c = 0.805 \times 10^{-4}$ s^{-1} that is representative of the geographic location of the SWIFT site (33.60795°N). In order to account for subfilter scale effects, the second variant of the nonlinear backscatter and anisotropy (referred to as NBA-TKE) model [166] was utilized.

As in other cases presented in Sections 7.1 and 7.2, all simulations were initialized under dry atmospheric conditions without radiation, cloud, or land-surface models. A uniform potential temperature profile was considered up to the initial inversion height, while an inversion layer was positioned above the ABL. To represent the geostrophic wind, a uniform wind profile was applied up to the model top. To suppress spurious vertical motions, a Rayleigh damping layer with a coefficient of 0.003 s^{-1} was implemented in the upper part of the inversion layer. Turbulence was induced by introducing small perturbations of $[-0.5, +0.5]$ K, obtained from a pseudo-random uniform distribution that decreased as

Table 7.7: Domain dimensions of the GAD and GAL simulations for neutral (NBL), convective (CBL), and stable (SBL) benchmarks.

Benchmark	Domain	$N_x \times N_y \times N_z$	$\Delta x = \Delta y$ [m]	Δz [m]	L_x [m]	L_y [m]	L_z [m]	Δt [s]
NBL, CBL	d01	$201 \times 101 \times 141$	6	$\sim$2	1200	600	1695.50	0.06250
	d02	$403 \times 151 \times 141$	2	$\sim$2	806	300	1695.50	0.02080
SBL	d01	$201 \times 101 \times 101$	6	$\sim$2	1200	600	1218.70	0.06250
	d02	$403 \times 151 \times 101$	2	$\sim$2	806	300	1218.70	0.02080

Note. N_x, N_y, and N_z stand for the number of grid points whereas $\Delta x, \Delta y$ and Δz represent the spatial grid resolutions in the x, y, and z directions, respectively. Note that Δz is set close to $\sim$2 m and cannot be directly set equal to $\Delta x = \Delta y = 2$ m, because of WRF's terrain-following eta coordinate system in the vertical direction. L_x, L_y, and L_z represent physical dimensions of the domain in the x, y, and z directions, respectively, and Δt is the computational time-step size.

a cubic function of height, to the initial potential temperature values below the capping inversion [204, 219]. For the fluxes of momentum and heat, the MOST was utilized [227], and the Revised MM5 Monin-Obukhov scheme [145] was employed to parameterize surface fluxes.

For the SBL case, a uniform surface cooling boundary condition was applied at the surface, at the beginning of hour 15, by prescribing the surface temperature as the horizontal average of temperature at the first grid point in the vertical direction [16, 167]. A cooling rate of -0.667 K h^{-1} was applied and the simulation was run for 12 h more. Numerical results were then analyzed to check if the model has reached the observed ensemble-averaged value of kinematic heat flux at the surface. As previously noted in the work of Mirocha et al. [218], imposing surface cooling creates a shift in mean flow direction over several hours. Due to the sensitivity to small changes in the geostrophic forcing during stable conditions, the wind direction was no longer aligned with the rotor after 20 h. The nested domain with the wind turbine model was turned on at the beginning of hour 19 h, and run for 1 h and 10-min. The first 10-min of the nested domain simulations were relegated to make sure that turbulence was well developed on the finer domain. Inflow wind speed and wind direction at hub height, for wind turbine control purposes in both the GAD and GAL models, were obtained at one rotor diameter upstream of the wind turbine rotor, based on running time averages of the instantaneous velocity components. The averaging interval consists of 2880 data points.

7.3.4 Results

Atmospheric inflow calibration

The ensemble-averaged inflow wind speed cannot be directly prescribed in WRF-LES; therefore, the components of the geostrophic wind should be determined iteratively so that the desired horizontal wind velocity component is obtained at the reference upstream position. Besides, laterally- and temporally-averaged vertical profiles of wind speed, wind direction, and turbulence kinetic energy are sampled at hub height at the met mast location and compared with experimental data for inflow calibration analysis.

In Figure 7.20, all neutral ABL simulations predict the observed upstream vertical wind speed and wind direction profiles fairly well; however, none of them are able to predict the negative and positive veer below and above the hub height observed in the measurements. Nevertheless, the magnitude of these wind direction changes is small and negligible. Large deviations in turbulence kinetic energy were observed for different numerical models, e.g., SOWFA-LES and NaluWind-LES. The other models, including WRF-LES, perform better and are able to predict turbulence kinetic energy profiles closely. Furthermore, the highest TKE values for simulations and experiments were found under neutral conditions due to the larger aerodynamic roughness length. In the WRF-LES model, the total kinetic energy profile, which considers the contributions of both the resolved and subfilter parts, was plotted.

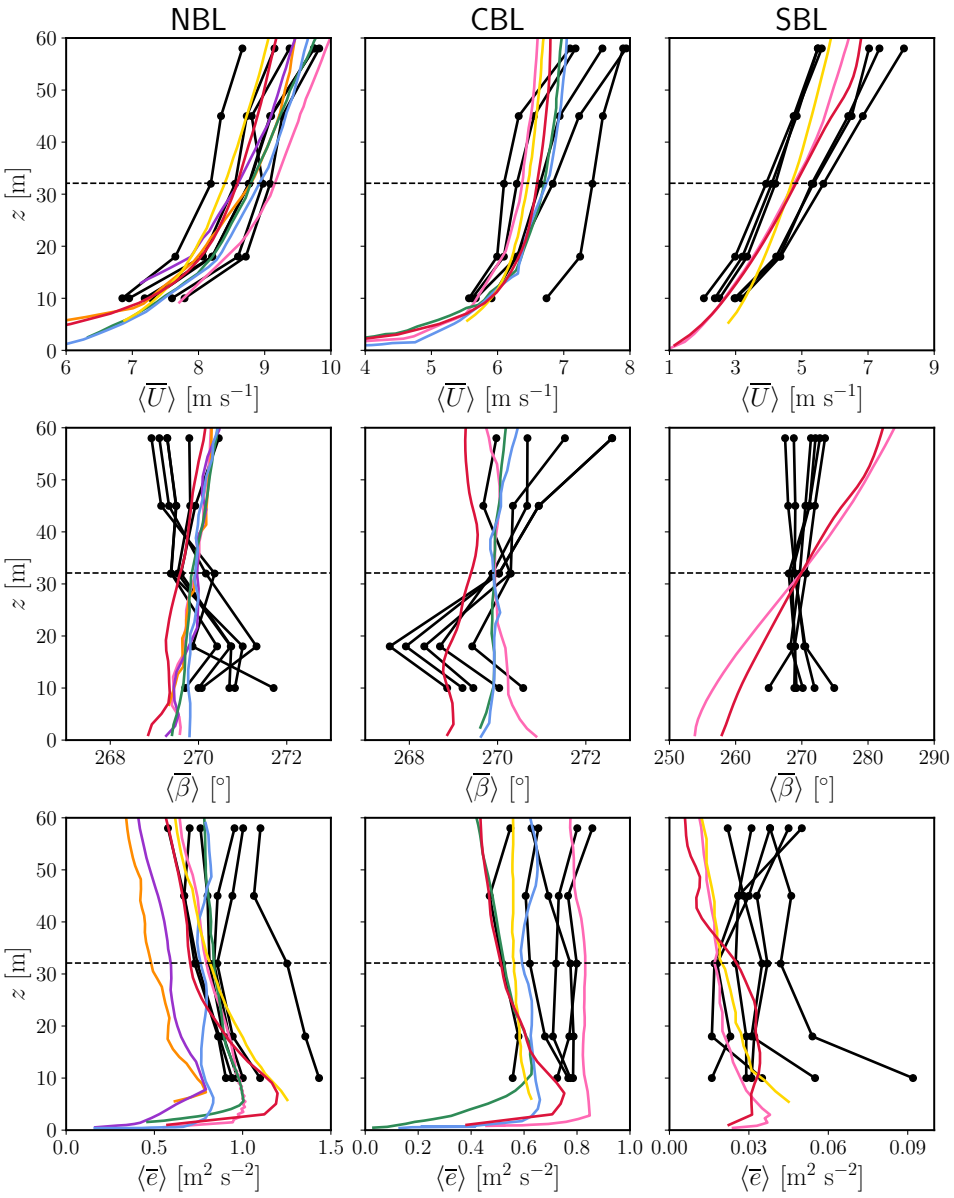

Figure 7.20: Vertical profiles of temporally- and laterally-averaged atmospheric quantities at the met mast location, horizontal wind speed, $\langle \overline{U} \rangle$ (left), wind direction, $\langle \overline{\beta} \rangle$ (middle), and turbulence kinetic energy, $\langle \overline{e} \rangle$ (right) for the three different states of the atmosphere. Each (——) represents 10-min averages of the experimental data. (——): SOWFA-2-LES, (——): SOWFA-LES, (——): NaluWind-LES, (——): PALM-LES, (——): EllipSys3D-LES, (——): Meso-NH-LES, and (——): WRF-LES (- - -) depicts the wind turbine hub height. $\langle \cdot \rangle$ represents the lateral average of the quantity of interest.

For unstable conditions, LES codes have more difficulties in matching the observed upstream wind speed profiles compared to the neutral case, especially above hub height. However, WRF-LES results show a better match for wind veer with a slight mismatch of about 0.7°, compared to the measurements at hub height. On the other hand, simulation results predict slight deviations in TKE because the geostrophic forcing is significantly lower than in the neutral case. The WRF-LES and PALM-LES models show a similar trend across the wind turbine rotor, producing a turbulence kinetic energy of about

Table 7.8: Relative errors (REs), $\mathbb{E}$, between WRF-LES results (obtained from time-series saved every 1-min during 1 hour simulation) and ensemble averages of time-averaged field measurements over 10-min periods for three different atmospheric stability conditions (Six ensemble averages for the neutral and stable cases, and five for the unstable case).

Benchmark	$\mathbb{E}_{U_{hub}}$ [%]	$\mathbb{E}_{\beta_{hub}}$ [%]	$\mathbb{E}_{\sigma_u}$ [%]	$\mathbb{E}_{\sigma_v}$ [%]	$\mathbb{E}_{\sigma_w}$ [%]	$\mathbb{E}_{u_*}$ [%]	$\mathbb{E}_{e_{hub}}$ [%]	$\mathbb{E}_{TI_{hub}}$ [%]
Neutral	-1.342	-0.056	10.838	-25.533	18.692	-21.844	-19.338	-25.453
Unstable	-1.551	-0.262	-11.880	1.709	-9.427	-12.450	-25.451	-29.693
Stable	0.457	0.297	39.159	-57.426	-72.123	5.715	-13.759	-21.239

Note. $\sigma_u, \sigma_v, \sigma_w$ denote the standard deviations of velocity components. All quantities are determined at hub height except for friction velocity, u_*. The relative error is quantified as $\mathbb{E} = 100 \times (A_{LES} - A_{EXP})/A_{EXP}$, where A_{LES} is the quantity of interest obtained from the time series of WRF-LES results saved every 1-min during 1 hour simulation, and A_{EXP} is the quantity of interest obtained from the ensemble averages of time-averaged field measurements over 10-min periods for different benchmarks.

0.5 m^2 s^{-2}, which is less than the ensemble average of experimental data and other LES results.

In the stable case, the WRF-LES model matched the ensemble-averaged value of the surface kinematic heat flux ($\overline{Q}_s = -0.005$ K m s^{-1}) after imposing surface cooling during 4 h. The mean wind speed and wind direction profiles, qualitatively, are well captured by the WRF-LES model, as in the case of SOWFA-2-LES. Considering the size of the rotor, it has been observed that the shift in the mean wind direction corresponds to approximately 12° shift in the mean wake resulting in an ellipsoidal shape. In addition to the upstream wind speed and wind direction profiles, the WRF-LES model underestimates turbulence level in stable conditions, although the surface kinematic heat flux, $\overline{Q}_s$, matched the observed ensemble average, and a close value for friction velocity was obtained (see Table 7.8).

In Table 7.8, relative errors between the ensemble averages of measurements and the WRF-LES results are given. For the neutral and unstable cases, satisfying results were achieved for hub height wind speed, second-order statistics as well as friction velocity, yet simulated turbulence intensity was underestimated by 25% and 29% for the neutral and unstable ABL conditions, respectively. A better match for hub height turbulence intensity was obtained under stable conditions after setting the surface temperature boundary condition. Since the ABL state is very stable, its simulation is very complex due to changes in turbulence dynamics. In stable ABL, internal wave motions strongly affect the depth of the ABL. Because the depth of the stable boundary layer is shallower than that of neutral and unstable boundary layers, the impact of multiple atmospheric physics such as radiative cooling, land-surface interaction, gravity waves, and katabatic flows becomes more significant. In addition to the atmospheric physics involved, the model representation of turbulent transport is significant and highly sensitive to the flux parameterizations and the parameter values used in the turbulence model. Also, increasing the surface cooling rate causes a rapid change in wind speed and wind direction, making inflow-wind turbine alignment highly difficult.

To ensure whether the spatial resolution is sufficient enough to resolve large eddies in LES, the spectra of the longitudinal and lateral velocity components are explored. In general, the energy spectrum represents the energy transfer from larger scales down to the smaller dissipative scales (e.g., Kolmogorov scales [165]), and is affected by the diurnal cycle of the atmosphere (i.e., energy content changes with the atmospheric stability).

Figure 7.21 shows the nondimensional spectrum for longitudinal and lateral components of the velocity at hub height under neutral and unstable conditions. WRF-LES results are compared with both field experiments and other LES results. Details for the calculation of the nondimensional spectra are given in Section 7.3.2.

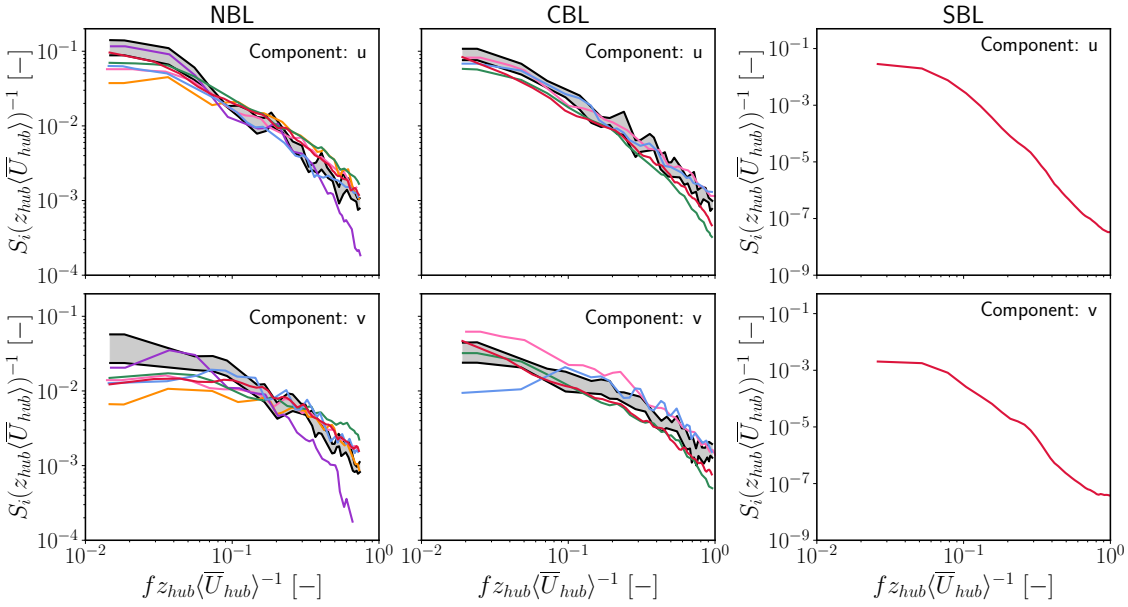

Figure 7.21: Mean spectra of the u and v velocity components for the neutral (a), unstable (b) and stable (c) cases. Longitudinal velocity components are shown at the top, while the lateral components are at the bottom. Note that the y-axis scale for stable conditions is smaller than for neutral and unstable ABL conditions due to lower energy content. The WRF-LES grid cut-off frequency at the effective resolution is $f_{\text{cut-off}} = 0.61$ Hz for NBL, $f_{\text{cut-off}} = 0.47$ Hz for CBL, and $f_{\text{cut-off}} = 0.34$ Hz for SBL. Also note that the WRF-LES model wind velocity is output at 1 s intervals; therefore, the highest resolvable frequency with this time series is 0.5 Hz. Gray region represents the measured spectrum. (—): SOWFA-2-LES, (—): SOWFA-LES, (—): NaluWind-LES, (—): PALM-LES, (—): EllipSys3D-LES, and (—): WRF-LES.

For the longitudinal velocity component, u, the nondimensional spectrum calculated from WRF-LES under neutral conditions fits well with experiments and other simulations starting from mid to high frequencies, but slightly underestimate the energy content at low frequencies, i.e., large-scale turbulent structures are not well resolved. Likewise, the spectrum for the v-component, shows a similar trend with a lower energy content compared to the u-component, from low to mid frequencies. For both nondimensional spectra under neutral conditions, the WRF-LES results are in good agreement compared with experimental spectra and some of the LES codes such as NaluWind, SOWFA, and PALM. Both nondimensional spectra represent the observations and simulations match fairly well the

energy content (i.e., well-matched hub height inflow TKE and turbulence intensity) under neutral conditions. The WRF-LES grid cut-off frequency at the effective resolution ($\approx 7\Delta x$ [303]) is $f_{\text{cut-off}} = 0.61$ Hz for NBL, $f_{\text{cut-off}} = 0.47$ Hz for CBL, and $f_{\text{cut-off}} = 0.34$ Hz for SBL. Note that the model wind velocity is output at 1 s intervals; therefore, the highest resolvable frequency with this time series is 0.5 Hz.

Under unstable conditions, the nondimensional spectrum of the u component is underestimated, like other LES models except for the EllipSys3D-LES model, in the low-mid frequency range. In contrast, from low to mid frequencies for the lateral nondimensional spectrum, the WRF-LES model becomes closer to the experimental results; however, it underestimates the nondimensional spectrum at high frequencies, as observed in the PALM-LES model. A steep energy drop-off was observed at high frequencies in nondimensional spectra for longitudinal and lateral components, while the other LES models either slightly underestimate or match the experimental results fairly well. One possible reason for this energy drop-off might be due to the insufficient spatial resolution used in the unstable simulation. However, the relative error between the simulated and observed energy content is minor; in particular, it can be assumed negligible in the mid-high frequency range.

It should also be noted that the spatial resolution used in the WRF-LES model for neutral and unstable cases is nearly four times coarser than other LES models, and thus, this could have a significant effect on resolving large eddies when validating inflow conditions. Another possible reason for underestimated energy content in unstable conditions is the lower TKE estimated by the WRF-LES model.

As anticipated, lower energy distribution was observed in all frequencies under stable ABL conditions compared to other atmospheric stability conditions for the spectra of longitudinal and lateral velocity components. No experimental results of the energy spectra were available for longitudinal and lateral velocity components for the stable case.

Wake velocity, variance, and vorticity fields

Time-averaged velocity fields in the wake shown in Figure 7.22 for the GAD and GAL models show similarities in terms of wake structures for all the stability conditions. Wake recovers slightly faster under unstable (CBL) conditions than under neutral (NBL) conditions, due to stronger turbulence mixing. As a result of dominant shear effects and weaker turbulence mixing, the wake extends further downstream of the wind turbine under stable (SBL) conditions. The flow velocity fields and wind turbine wake in x-y planes under CBL are asymmetric due to slight misalignment between the inflow direction and wind turbine rotor plane.

The GAD and GAL models impart additional drag on the mean flow due to the presence of nacelle and tower, which can be discernible in x-z planes at resolutions fine enough to model large-scale wind turbines. Vestas V27 is a real-scale wind turbine with a relatively small nacelle compared to other larger wind turbines; thus, the deceleration of flow due to

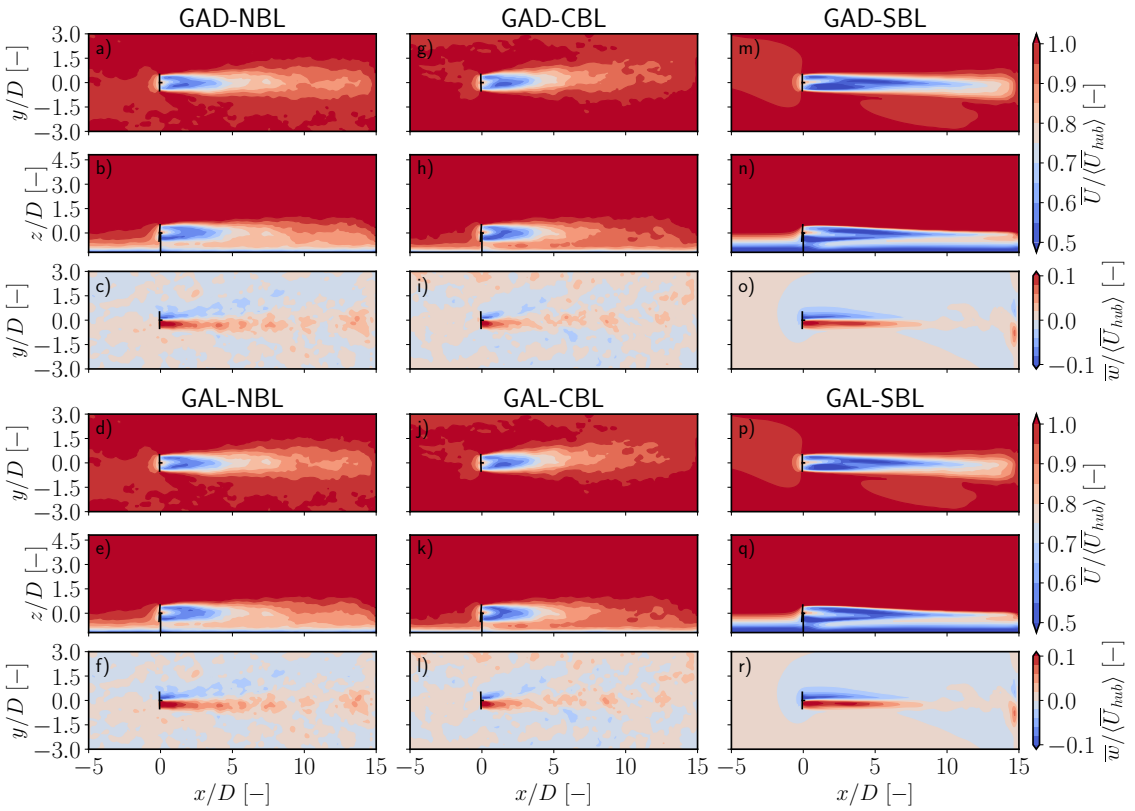

Figure 7.22: Contour plots of normalized and 1-hour averaged horizontal wind speed, $\overline{U}$, in the x-y [(a), (g), (m), (d), (j) and (p)] and x-z [(b), (h), (n), (e), (k) and (q)] planes, and vertical velocity, $\overline{w}$, in the x-y plane [(c), (i), (o), (f), (l) and (r)] for the GAD and GAL models under neutral, unstable, and stable atmospheric conditions, respectively.

the nacelle is not clearly visible at the grid resolution simulated herein. Although there are minor differences between the GAD and GAL model results, these are difficult to distinguish from time-averaged contour plots of normalized horizontal wind speed, $\overline{U}/\langle\overline{U}_{hub}\rangle$, and normalized vertical velocity component, $\overline{w}/\langle\overline{U}_{hub}\rangle$, in x-y and x-z planes.

Figure 7.23a presents the time-averaged and normalized velocity components, whereas Figure 7.23b shows 1-hour variance of velocity components in the y-z plane looking upstream, for the NBL, CBL, and SBL cases, respectively. These contours are plotted at $0.5D$ downstream of the wind turbine in the longitudinal direction. The deficiency in the u velocity component in Figures 7.23a[(a), (g), (m), (d), (j), and (p)] is because of the effects of thrust generated by the rotor. Since the GAD and GAL models reproduce similar thrust, no clear difference between these two models is evident in all the simulated cases. These contour plots also show the tower wake distortion that causes an asymmetry due to wake rotation in the counter-clockwise direction when looking upwind. Similar results were also found in the work of Churchfield et al. [56]. The effect of drag force created by the tower is not so clear due to coarse grid resolution, yet it contributes to the total wake velocity deficit more under SBL than in the other cases, because of lower turbulence mixing. The wake is stretched in the southwest-northeast direction under SBL conditions, due to the addition of surface cooling for several hours after spin-up, which results in

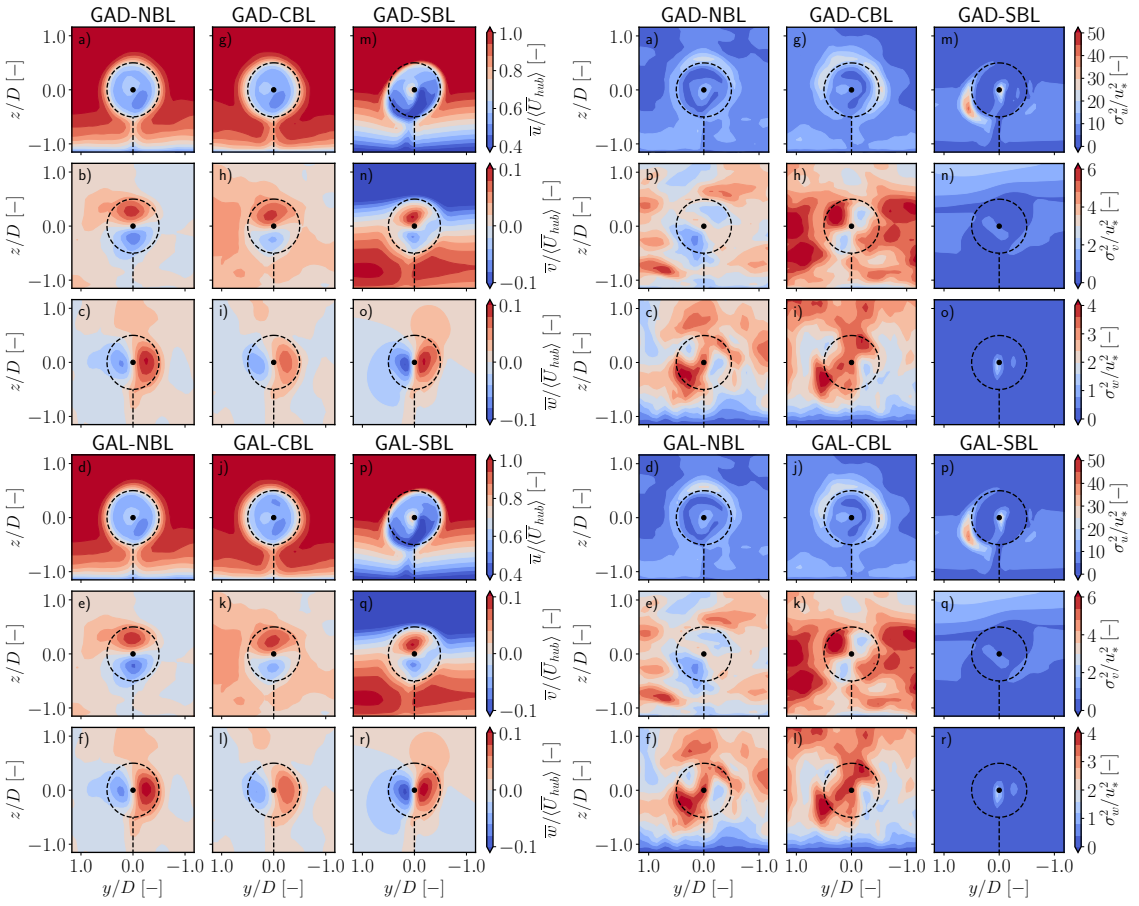

(a) 1-hour averaged velocity components. **(b)** 1-hour variance of velocity components.

Figure 7.23: Contour plots of (a) normalized and time-averaged longitudinal [(a), (g), (m), (d), (j), and (p)], lateral [(b), (h), (n), (e), (k), and (q)] and vertical [(c), (i), (o), (f), (l), and (r)] velocity components, (b) 1-hour variance of longitudinal [(a), (g), (m), (d), (j), and (p)], lateral [(b), (h), (n), (e), (k), and (q)] and vertical [(c), (i), (o), (f), (l), and (r)] velocity components in the y-z plane looking upwind for the GAD and GAL models under neutral, unstable, and stable atmospheric conditions. These planes are $0.5D$ downstream of the wind turbine tower in the longitudinal direction.

numerically-generated wind veer within the rotor-swept area, even though no wind veer was observed during the experimental campaign. Nondimensional and time-averaged $\overline{v}$ and $\overline{w}$ velocity components reproduced by both wind turbine models for all cases, show a physically sound reproduction of the wake rotation due to torque created by rotor tangential forces and the tangential component of the velocity exerted on the flow, associated to the rotor torque. Normalized 1-hour variance fields, computed from velocity components, are also examined to reveal additional differences in the flow characteristics resolved by the two different wind turbine parameterizations, under the three atmospheric stability conditions analyzed in this work. Turbulence around the rotor is well resolved in both the NBL and CBL cases; however, the current grid resolution is not sufficient enough to resolve turbulence in the SBL case, hence the lower inflow turbulence provokes less entrainment of outer flow in the wake leading to less intense wake recovery, and thus larger wake deficit. Normalized variances of the v and w velocity components, σ_v^2/u_*^2 and σ_w^2/u_*^2,

respectively, increase with the increasing height, for all the analyzed cases. Continuous ring-like patterns of normalized variance of u velocity component, σ_u^2/u_*^2, were observed in the GAD and GAL model predictions, as a consequence of coarse grid resolution across rotor diameter (i.e., $\Delta x = 2$ m, $D = 27$ m means ~ 7 grid points per blade). Therefore, both models produce a continuous ring-like region of high values for σ_u^2/u_*^2 at the blade root and tip (slightly larger for GAL), resulting in a similar pattern in the wake. Although a grid resolution of 2 m is sufficient enough to capture smaller-scale motions under certain atmospheric conditions, the stable case considered herein is difficult to simulate because it corresponds to a very stable atmospheric condition with a shallow ABL [78].

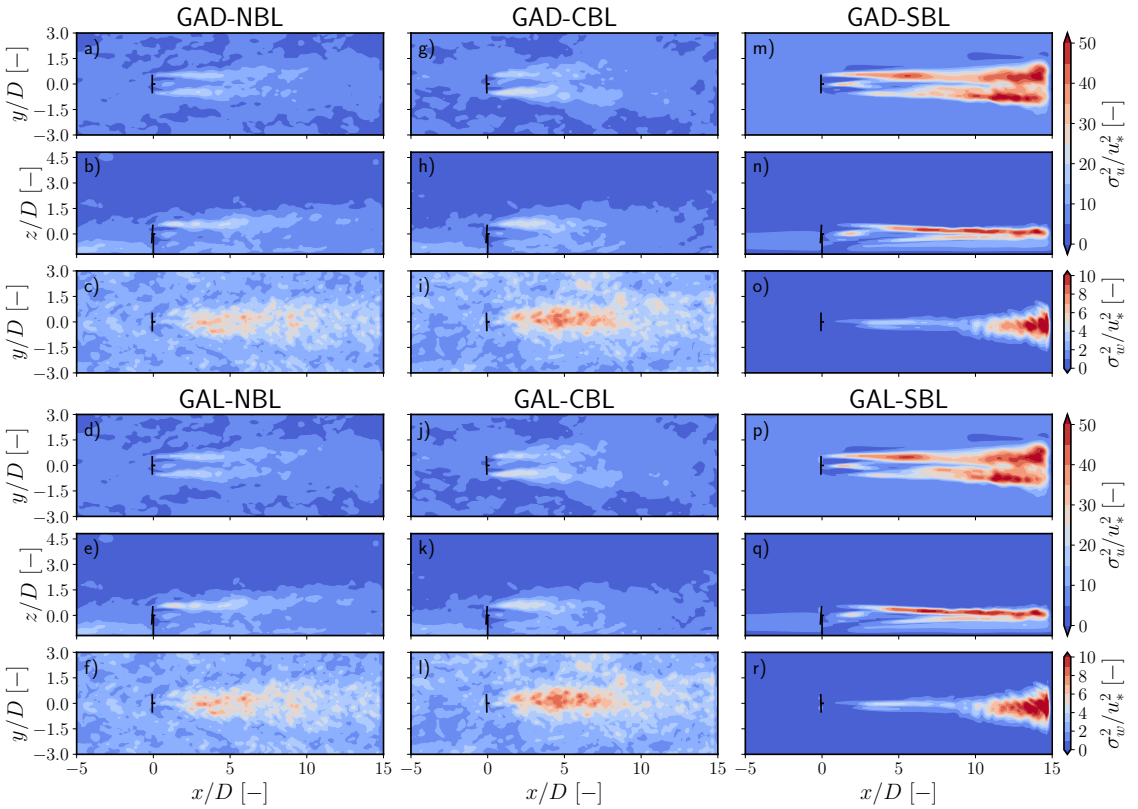

Figure 7.24: Contour plots of 1-hour variance of longitudinal velocity component, σ_u^2, in the x-y [(a), (g), (m), (d), (j), and (p)] and x-z [(b), (h), (n), (e), (k), and (q)] planes and vertical velocity component, σ_w^2, in the x-y plane [(c), (i), (o), (f), (l) and, (r)] for the GAD and GAL models under neutral, unstable, and stable atmospheric conditions. These quantities are normalized by the square of friction velocity, u_*^2, obtained at the met mast location.

Figure 7.24 illustrates the spatial evolution of the variance of longitudinal and vertical velocity components in x-y and x-z planes predicted by the GAD and GAL models, for the three considered stability conditions. At first glance, it is seen that larger variance production is observed under SBL, even though the turbulence intensity is very low. In fact, this is due to the very low friction velocity values used for normalization. Due to the higher inflow turbulence intensity levels, a higher variance was observed in the wake, especially in the wake under CBL, compared to NBL, resulting in a shorter wake. σ_u^2/u_*^2 is largest at the top of the rotor in the x-z plane in the far wake for all cases (see Figures

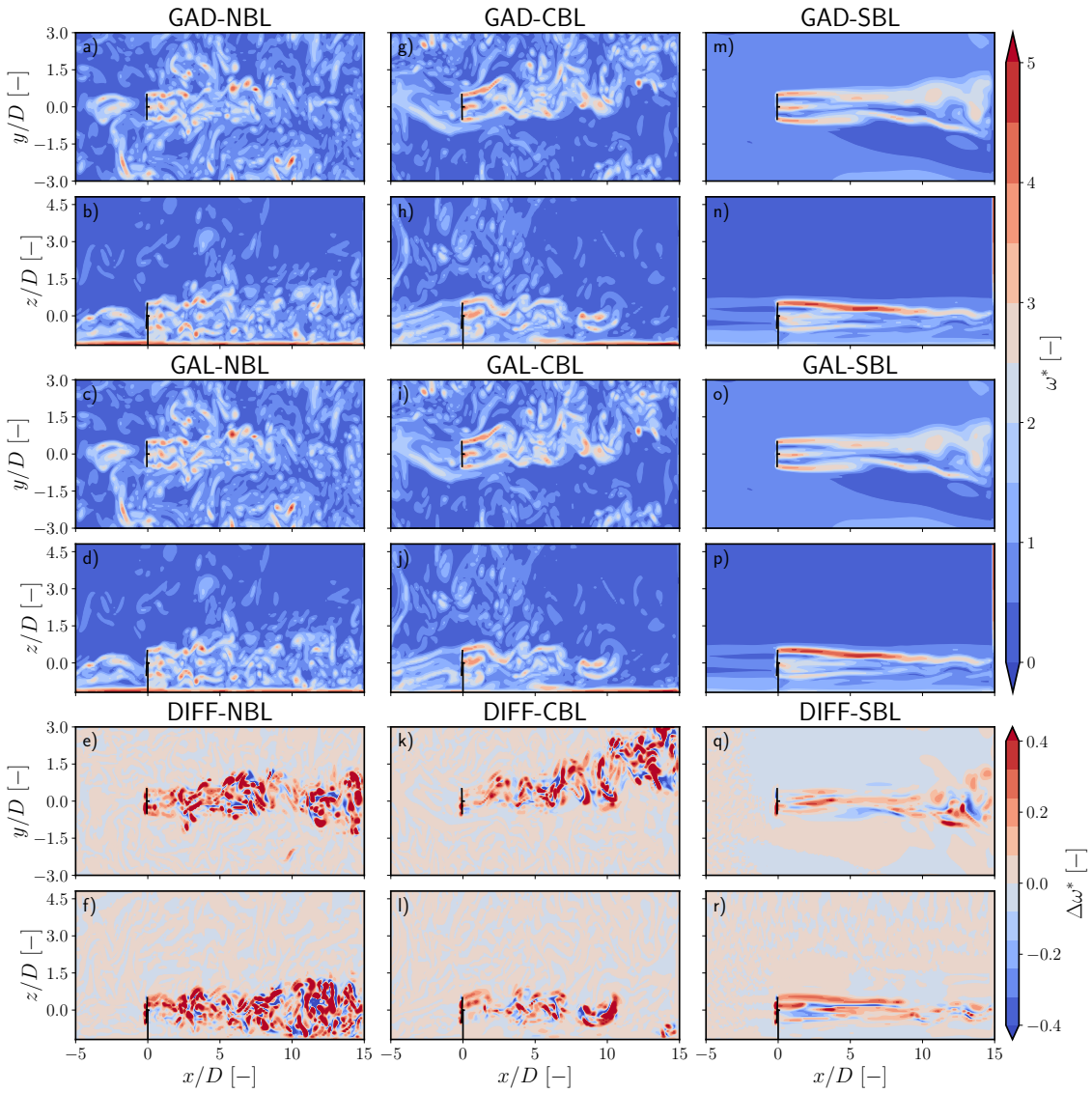

Figure 7.25: Instantaneous contour plots of the magnitude of normalized vorticity, ω^*, in the x-y [(a), (g), (m), (c), (i), and (o)] and x-z [(b), (h), (n), (d), (j), and (p)] planes for the GAD and GAL models under neutral, unstable, and stable atmospheric conditions. The difference in the magnitude of normalized vorticity, $\Delta\omega^*$, between the GAL and GAD models in the x-y plane [(e), (k), and (q)] and in the y-z plane [(f), (l), and (r)] are shown at the bottom. All these results are obtained 60-min after initialization of the nested domain (i.e., 50-min after discarding the first 10-min in each simulation).

7.24[(b), (h), (n)] for the GAD and Figures 7.24[(e), (k), (q)] for the GAL), as a result of larger aerodynamic forces imparted onto the flow due to higher wind speeds at higher vertical levels. σ_u^2/u_*^2 is higher near the nacelle and tower, but lower than the values found close to the top of the rotor. Lower values of σ_u^2/u_*^2 in the x-y plane, for both models, are observed after $\sim 5D$ under NBL and CBL, persisting up to $15D$ under SBL, due to very low inflow turbulence levels (featuring much smaller variance values, especially in the near wake). However, σ_w^2/u_*^2 has lower values up to $\sim 9D$ near the wake center and increases with the transition to turbulence starting from $\sim 10D$. The differences between the GAD and GAL models are visible under SBL conditions in the near wake in Figures

7.24[(m), (n), (o), (p), (q), and (r)], due to the aerodynamic forces applied along the blade representing lines in the GAL model, as opposed to aerodynamic forces averaged over annular elements in the GAD [204].

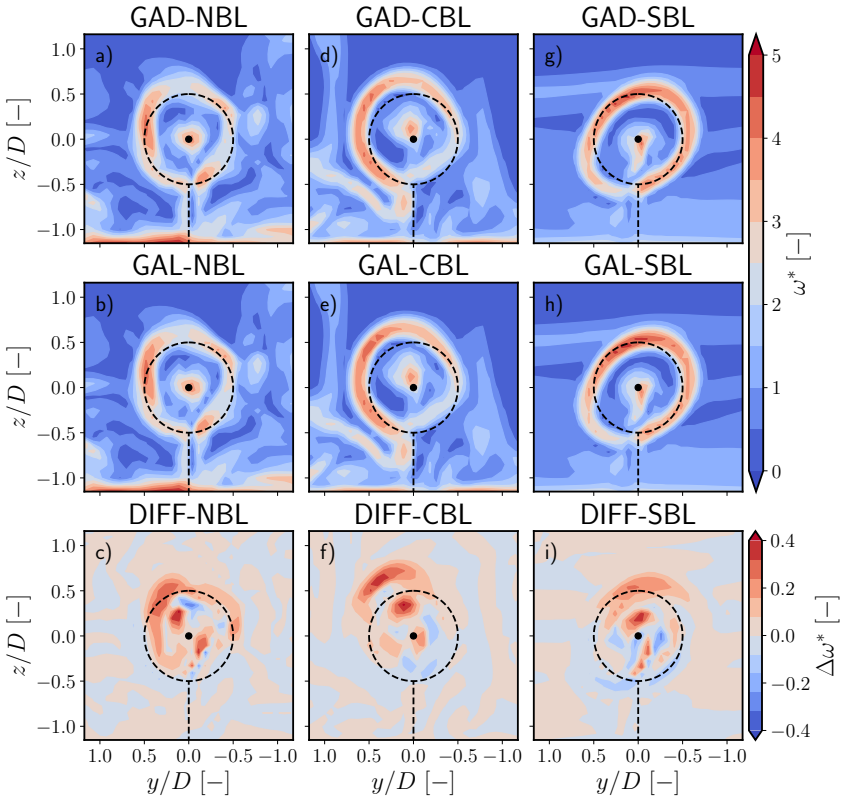

Figure 7.26: Instantaneous contour plots of the magnitude of normalized vorticity, ω^*, in the y-z plane, that is looking upwind and $0.5D$ downstream of wind turbine tower in the longitudinal direction, for the GAD [(a), (d), and (g)] and GAL [(b), (e), and (g)] models under neutral, unstable, and stable atmospheric conditions. Difference in the magnitude of normalized vorticity, $\Delta\omega^*$, between the GAL and GAD models [(c), (f), and (i)] are shown in the last row.

The normalized vorticity fields, $\omega^* = ||\vec{\omega}||z_{hub}\langle\overline{U}\rangle_{hub}^{-1}$, with $||\vec{\omega}||$ being the vorticity magnitude, calculated 60-min after initialization of the finer domain, for both wind turbine models and the three stability cases. These vorticity fields, along with the difference in nondimensional vorticity field from both models denoted by $\Delta\omega^* = \omega^*_{GAL} - \omega^*_{GAD}$ are shown in Figure 7.25 [(e), (f), (k), (l), (q), and (r) for the NBL, CBL, and SBL cases, respectively]. Vorticity fields from the GAD and GAL models slightly differ as root and tip vortices are shed away from the blade representing lines in the GAL model, although this is not easily detectable in Figures 7.25a and 7.25b. However, despite the coarse grid resolution, prominent vortex patterns are seen in the wakes produced by the GAL model compared to GAD, especially near the blade tip (Figures 7.25(e), (f), (k), (l), (q), and (r)). For instance, the vorticity fields under CBL show more spatial variability/irregularity, due to higher turbulence levels, resulting in more deviation in the propagated wake direction. This is less pronounced under NBL and the roll vortices at the blade tip from the GAL model are not clearly visible. As expected, large vorticity values around the nacelle and

tower, as well as in the downstream wake were observed under all atmospheric conditions. Due to insufficient grid resolution, continuous vortex structures persist up to $\sim 5D$ in the x-y plane and $\sim 9D$ in the x-z plane under SBL and break down in the far wake where wake instability growth leads to much higher turbulence levels. For both wind turbine models, all simulations manifest an increase in vorticity at the root and tip of the blades. Deflection in the vorticity field under CBL is due to the inflow-wind turbine misalignment and higher turbulence mixing, whereas it is due to wind veer in the SBL case (Figure 7.26).

Spectra and cross-spectra of velocity components in the wake

In order to quantitatively analyze the evolution of the wake in the longitudinal direction, time-averaged spatial spectra of three velocity components, that are $\overline{E}_{(uu)_y}, \overline{E}_{(vv)_y}$ and $\overline{E}_{(ww)_y}$, and time-averaged spatial cross-spectra of longitudinal and vertical velocity components, $\overline{E}_{(uw)_y}$, normalized by κ_y/u_*^2, with κ_y being the wavenumber in the lateral direction, were computed from the GAD and GAL model results. All the spatial spectra illustrated in Figures 7.27 and 7.28 were calculated based on the same methodology used in the work of [59]. Only the real part of the cross-spectra of the longitudinal and vertical velocity components is shown in Figures 7.27 and 7.28. In short, the spatial spectra and co-spectra at different downstream locations are obtained by calculating the spatial spectra in terms of the lateral component, κ_y, of the wavenumber vector, corresponding to the instantaneous spatial series along the y coordinate. This is done for each time instant. All spatial spectra are, then, time-averaged over 1-hour. A moving average algorithm with a window size of 25 points in the lateral direction (wavenumber space) was applied to obtain a smoother representation of both spectra and co-spectra. The WRF-LES grid κ_y cut-off value is $\kappa_{y_{\text{cut-off}}} = 2\pi/7\Delta x = 21.43\ \text{m}^{-1}$.

As expected, the highest energy content in the wake based on $\kappa_y\overline{E}_{(uu)_y}/u_*^2$ was found immediately after the wind turbine rotor at $x = 1D$, with the lowest energy in the far wake in all cases (Figure 7.27). The highest energy levels distributed over a wide range of wavenumbers in $\kappa_y\overline{E}_{(vv)_y}/u_*^2$ and $\kappa_y\overline{E}_{(ww)_y}/u_*^2$ were found to be between the mid and far wakes under NBL and CBL, while higher energy levels in $\kappa_y\overline{E}_{(vv)_y}/u_*^2$ and $\kappa_y\overline{E}_{(ww)_y}/u_*^2$ were observed in the near and far wakes under SBL conditions, respectively. The time-averaged nondimensional co-spectra of u and w velocity components, $\kappa_y\overline{E}_{(uw)_y}/u_*^2$, in the wake exhibit a similar trend for all atmospheric stability conditions, except in the inertial subrange of the co-spectra for the SBL case. As anticipated, the lowest energy content was observed at $2.5D$ upstream of the wind turbine. The covariance between u and w velocity components directly relates to turbulence production due to upward-downward momentum transport.

A closer look at flow evolution in the near wake obtained from the GAD and GAL models under NBL, CBL, and SBL conditions is given in Figure 7.28. In all simulations of the GAL model, higher energy levels were found in the mid-to-high nondimensional wavenumber range, compared to the predictions of the GAD model. This may be due to the larger aerodynamic forces projected onto the flow field (see also Figure 7.31 for aerodynamic load

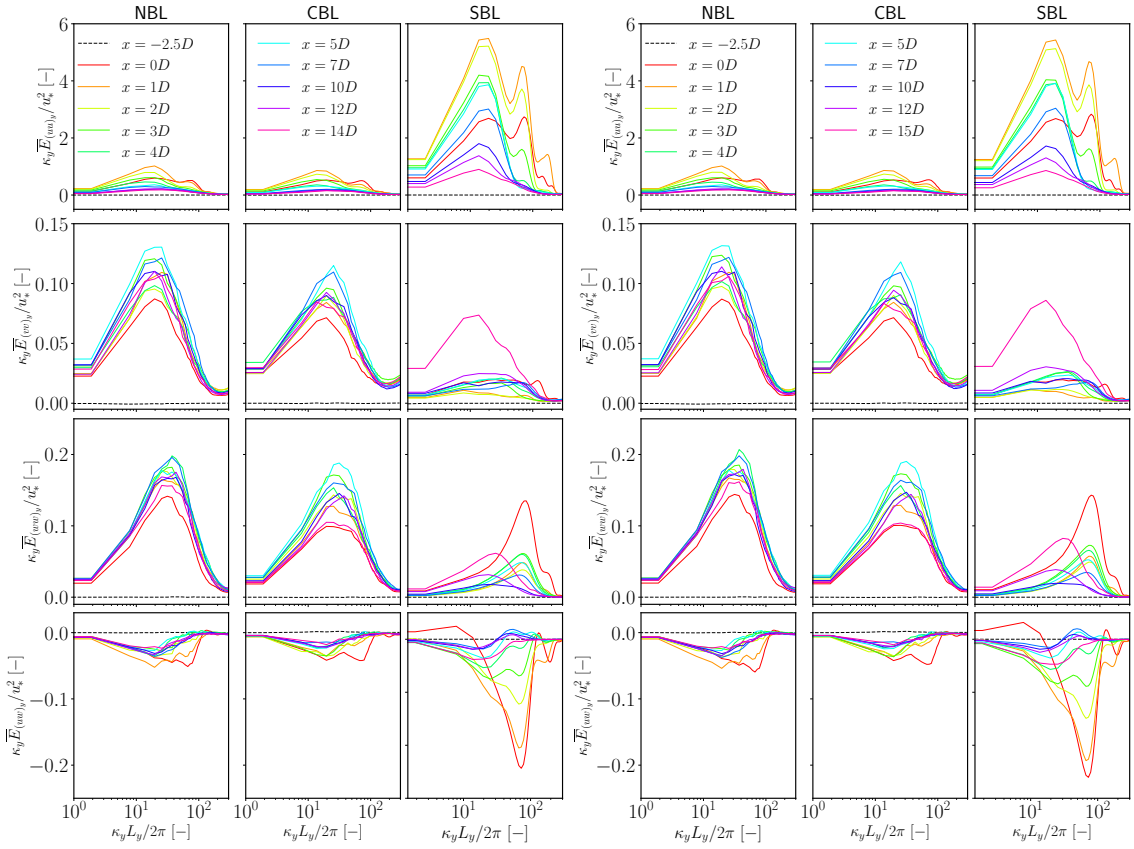

(a) GAD. **(b)** GAL.

Figure 7.27: Time-averaged nondimensional energy spectra obtained from three velocity components, that are $\kappa_y \overline{E}_{(uu)_y}/u_*^2$, $\kappa_y \overline{E}_{(vv)_y}/u_*^2$ and $\kappa_y \overline{E}_{(ww)_y}/u_*^2$, and cross-spectra of u and w velocity components, $\kappa_y \overline{E}_{(uw)_y}/u_*^2$, as a function of nondimensional spanwise wave number, $\kappa_y L_y/2\pi$, with $L_y = 300$ m being domain width, at various locations in the longitudinal direction for the GAD and GAL models under different atmospheric stability conditions. The dashed line denotes the spectra and co-spectra at $2.5D$ upstream of the wind turbine rotor, whereas other colored lines refer to the spectra and co-spectra at different downstream locations. Note that only the real part of the cross-spectra is shown. The WRF-LES grid κ_y cut-off value is $\kappa_{y_{\text{cut-off}}} = 2\pi/7\Delta x = 21.43$ m^{-1}.

comparison of the GAD and GAL models). The evolution of the spectra of the velocity components along the wake, reproduced by the two wind turbine models, shows self-similar features in the energy-containing range (low wavenumbers), despite the oscillatory patterns observed for wavenumbers in the inertial subrange (mid-to-high wavenumbers) under SBL. In contrast to the similar energy levels predicted by the models for the NBL and CBL conditions, higher energy levels are observed in the far wake under SBL, as a consequence of the delayed occurrence of intense wake instabilities (see also contour plots of variances of the u and w velocity components in the x-y plane under SBL conditions in Figure 7.24).

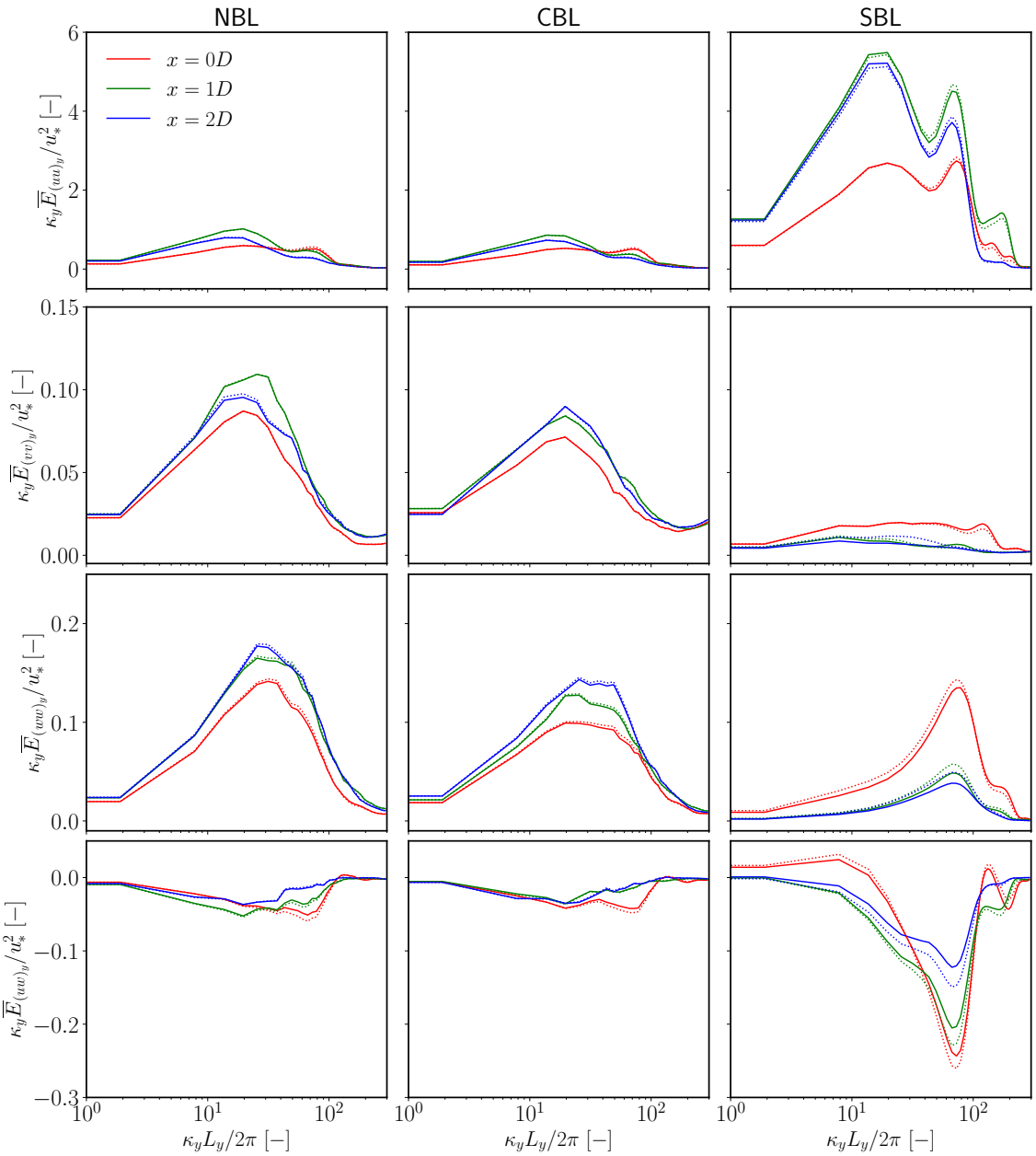

Figure 7.28: Same as in Figure 7.27, but with a zoomed view. Solid lines denote the results from the GAD model, whereas dashed lines denote the GAL model results in all cases. The WRF-LES grid κ_y cut-off value is $\kappa_{y_{\text{cut-off}}} = 2\pi/7\Delta x = 21.43$ m^{-1}.

Wake velocity deficit profiles

Time-averaged values of instantaneous velocity deficit profiles, $\overline{VD}$, are plotted in Figure 7.29. The horizontal profiles of $\overline{VD}$ are obtained at hub height, whereas the vertical profiles of $\overline{VD}$ are obtained along the tower at zero span. Both $\overline{VD}$ profiles are obtained in a fixed frame of reference on a coordinate system centered at the nacelle. Numerical results obtained from different LES codes were compared with the measurements, which vary in the 95% confidence interval for all cases. Wake velocity deficit results of LES codes reported in the work of Doubrawa et al. [80] were averaged into a single curve in both horizontal and vertical directions, and plotted with minimum and maximum deficits around

the mean value in Figure 7.29. Experimental wake velocity deficit profiles were distorted in the near wake; therefore, only measurements starting at $x = 2D$ were considered in this work. However, velocity deficit profiles from the GAD and GAL models at $x = 0D$ and $x = 1D$ behind the wind turbine rotor were also plotted in Figures 7.29a and 7.29b for a more complete near wake analysis. It is not clear whether the aerodynamic effects of nacelle and tower were modeled in LES codes reported in the reference paper; however, these aerodynamic effects were modeled in the Meso-NH-LES [142] and WRF-LES models. Horizontal and vertical profiles of velocity deficit at $x = 0D$ from the GAL model in Figures 7.29a and 7.29b show slightly higher velocity deficit values than the GAD model, in agreement with the literature results on the comparison of the GAD and GAL models [204, 269, 322].

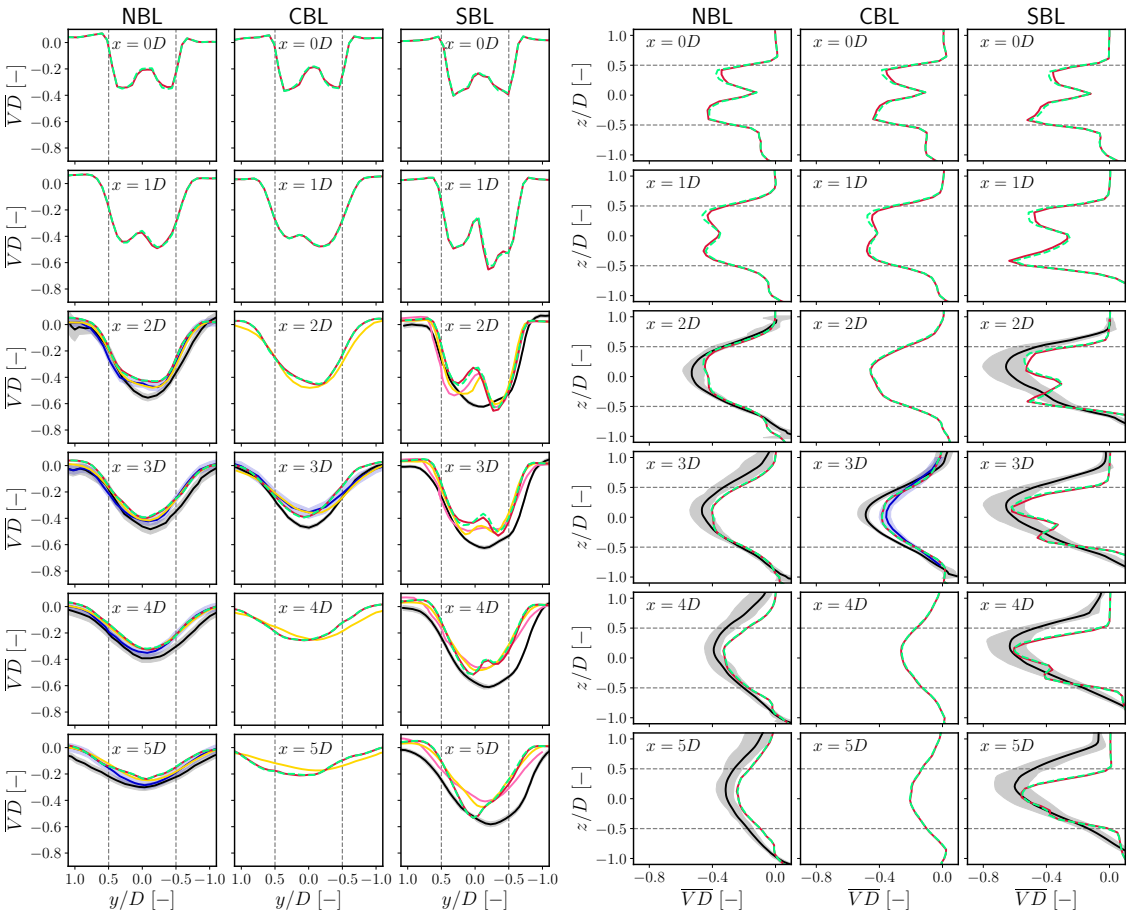

(a) Horizontal profiles of $\overline{VD}$. **(b)** Vertical profiles of $\overline{VD}$.

Figure 7.29: Comparison of time-averaged and normalized wake velocity deficit, $\overline{VD}$, profiles in the (a) lateral and (b) vertical directions for the neutral, unstable, and stable ABL cases. (——) with gray shaded regions show measurements and 95% confidence interval. (——) refers to the mean values of the LES model results reported in Doubrawa et al. [80]. (——): SOWFA-2-LES, (——): Meso-NH-LES, (——): GAD, and (- - -): GAL models. The light blue shaded region in the simulation data shows the minimum and maximum range of other LES code predictions. The horizontal velocity deficit profiles shown here are upwind representations. The wind turbine rotor lays in between two of the dashed black lines.

In Figure 7.29a, starting from $x = 1D$, the discrepancy in the predictions of the velocity deficits between the GAD and GAL models disappears in all cases. Simulation results of the GAD and GAL models agree reasonably well with results from other LES codes and measurements between $x = 2D$ and $x = 5D$ under NBL conditions, with only a small difference in the magnitude of the velocity. The results of the CBL and SBL cases show asymmetrical profiles at hub height due to the non-uniformity of the incoming flow and the presence of wind veer across the wind turbine rotor in the simulations, respectively. Higher surface kinematic heat flux produces extra turbulence and this increases the wake recovery under CBL (i.e., higher turbulence levels). The predicted freestream turbulence intensity was slightly higher than the experimental value and SOWFA-2-LES model results under SBL conditions; consequently, the wake was expected to recover faster than what was observed in measurements and in the simulations of the SOWFA-LES-2 model. One possible reason for the longer wake prediction is the coarse grid resolution used herein, which plays a vital role in how the wake attenuation is reproduced under very stable ABL conditions. It is also possible to judge the adequacy of the grid size utilized in the stable ABL case, the Ozmidov length scale, L_O, or the buoyancy length scale, L_b, given by Equations (3.26) and (3.27) can also be calculated. The smallest Ozmidov length scale below hub height is 0.5 m and the largest buoyancy length scale below hub height is 4.6 m. Although a few previous studies have shown that some SFS models, like the Smagorinsky model, can still work well for grid resolutions that are sufficiently less than L_b but still greater than L_O [160, 329]. Although both the vertical and horizontal grid resolutions used in the present stable case simulation, $\Delta = 2$ m, fall between $L_O < \Delta < L_b$, these grid resolutions are too coarse to capture the turbulent flow dynamics near the surface. It may be better to employ a minimum grid resolution smaller than the smallest Ozmidov scale to rely on the LES of stable ABL flow to capture the stratified energy cascade [160, 231].

Figure 7.29b compares the vertical velocity deficit profiles at several positions downstream of the wind turbine rotor. Unlike the symmetric profiles found at $x = 0D$ in Figure 7.29a, the influence of the tower can be discerned as the inclusion of the aerodynamic effects from the tower increases the velocity deficit and creates an asymmetrical wake profile in the vertical direction. Due to the absence of the LES results of vertical velocity deficit profiles, except at $x = 3D$ for CBL, the GAD and GAL results are compared with measurements only. The results from both models are in agreement with the measurements for all stability conditions.

Figure 7.30 quantifies the bias and RMS errors of the horizontal and vertical profiles of velocity deficit, $\overline{VD}$, at several downstream locations between the GAL model and experimental data. Due to similar profiles obtained from both models, only errors from the GAL model are given. Both datasets were sub-sampled within the ranges of $[-1.0, +1.0]$ and $[-0.75, +0.75]$ in the horizontal and vertical directions, respectively, for the velocity deficit profiles. Subsequently, linear interpolation was applied to these sub-sampled data to obtain values at point i. The bias and RMS errors in the horizontal profiles of $\overline{VD}$ under NBL conditions are approximately constant at all downstream locations, yet the

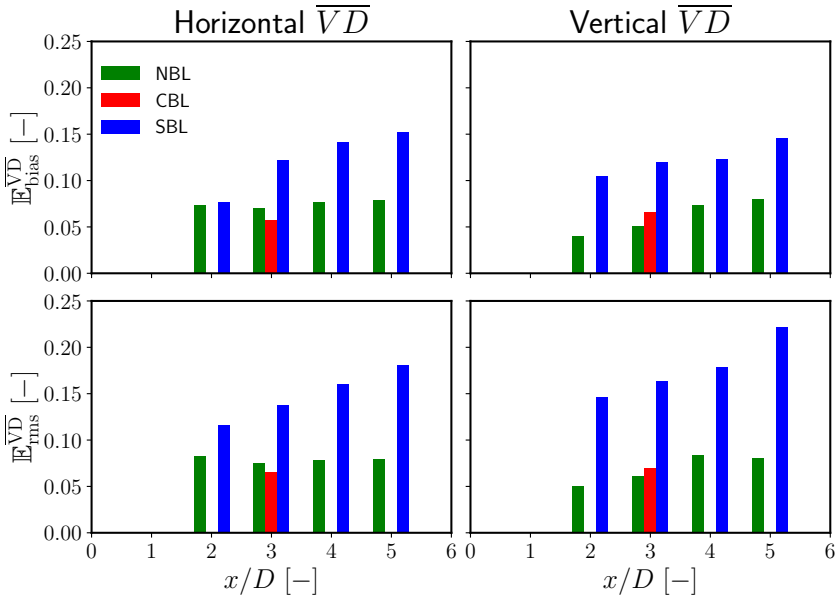

Figure 7.30: Bias, $\mathbb{E}_{\text{bias}}$, and root mean square (RMS), $\mathbb{E}_{\text{rms}}$, errors of horizontal (left) and vertical (right) velocity deficit between the GAL model and experimental data from different ABL cases. Bias and root mean square errors are calculated using Equations (2.25a) and (2.25c).

errors gradually increase in the vertical profiles of $\overline{VD}$. Under SBL conditions, all the errors increase when moving further downstream. In contrast, although there is only one measurement location available, the errors are roughly constant across different locations under CBL conditions.

Aerodynamic performance

Radial distributions of time- and disk-averaged angle of attack, $\overline{\alpha}$, nondimensional normal and tangential forces, $\overline{F}^*_n$ and $\overline{F}^*_t$, which are given as

$$\overline{F}^*_n = \frac{\overline{f}_n}{0.5\rho c\langle\overline{U}_{hub}\rangle^2}, \tag{7.8}$$

and

$$\overline{F}^*_t = \frac{\overline{f}_t}{0.5\rho c\langle\overline{U}_{hub}\rangle^2}, \tag{7.9}$$

where $\overline{f}_n$ and $\overline{f}_t$ are mean normal and tangential forces per unit length, respectively, are plotted in Figure 7.31. Although similar local angle of attack distributions were found in all simulations, minor differences were found in aerodynamic force distributions, starting from mid-span at $r/R \approx 0.3$ close to the blade tip, $r/R \approx 0.9$, in all cases. The local maxima in normal force at approximately $0.85R$ yields two local minima in the velocity deficit profiles (roughly at similar locations along the blades where the largest force gradients occur) [263]. This effect vanishes in the far wake due to turbulence mixing and the double Gaussian-shaped velocity deficit profile transforms into a single profile that is approximately Gaussian in shape [204].

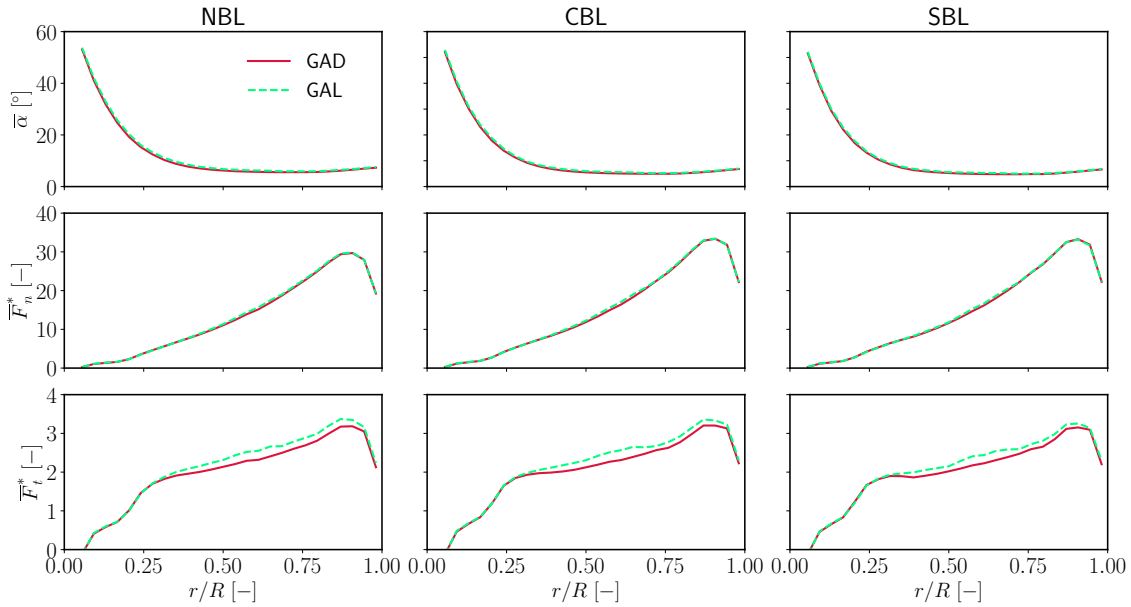

Figure 7.31: Time- and disk-averaged angle of attack, $\overline{\alpha}$, (first row), nondimensional normal, $\overline{F}_n^*$ (second row), and tangential, $\overline{F}_t^*$ (third row), as a function of the nondimensional radial distance along the blade using the GAD and GAL models under varying atmospheric conditions. The radial distance is made nondimensional by dividing by the radius of the blade.

In Figure 7.32, the predictions of different wind turbine performance variables estimated by the GAD and GAL models are compared with the published LES data from six different codes and experimental results, under NBL, CBL, and SBL conditions. The analyzed variables are: rotor speed, Ω, generator power, P_g and torque, M_g, and aerodynamic thrust coefficient, C_T. A fixed blade-pitch angle, that is $\theta_p = -0.75$, was utilized, whereas the rotor speed was adjusted based on running averages of hub height wind speed calculated at $1D$ upstream of the wind turbine through a look-up table for Vestas V27. The GAD and GAL models predict the measured rotor speed quite well compared to other LES codes. However, the generator power and torque estimations from other LES codes differ significantly under all atmospheric conditions. The mean generator power predicted by the GAD and GAL models lies within the standard deviation around the mean value of the experimental data under all conditions.

The relative errors, $\mathbb{E}$, of wind turbine response quantities between numerical models and ensemble averages of time-averaged field measurements over 10-min periods for three different atmospheric stability conditions are shown in Table 7.9. With the exception of PALM-LES-GAL and GAD models, all models overestimate the generator power and torque, with variations of about 38% and 42% for NBL, 26% and 16% for CBL, and 50% and 38% for SBL, respectively. The difference between the GAL and GAD models in predicted generator power and torque is roughly 7% and 7% under NBL, 6% and 7% under CBL, and 6%, and 7% under SBL conditions, respectively. This overestimation observed in the predictions from the GAL model for all atmospheric stability conditions is also observed in nondimensional tangential aerodynamic force distributions along the

blade depicted in Figure 7.31. The aerodynamic thrust coefficients estimated by the GAD and GAL models under different atmospheric stability conditions are in the range of 0.74-0.80, which is in good agreement with the results of other LES codes. The relative error between the GAL and GAD models is less than 1.5% for NBL, 1.6% for CBL, and 1.1% for SBL, respectively. No in-situ measurements of aerodynamic thrust were available.

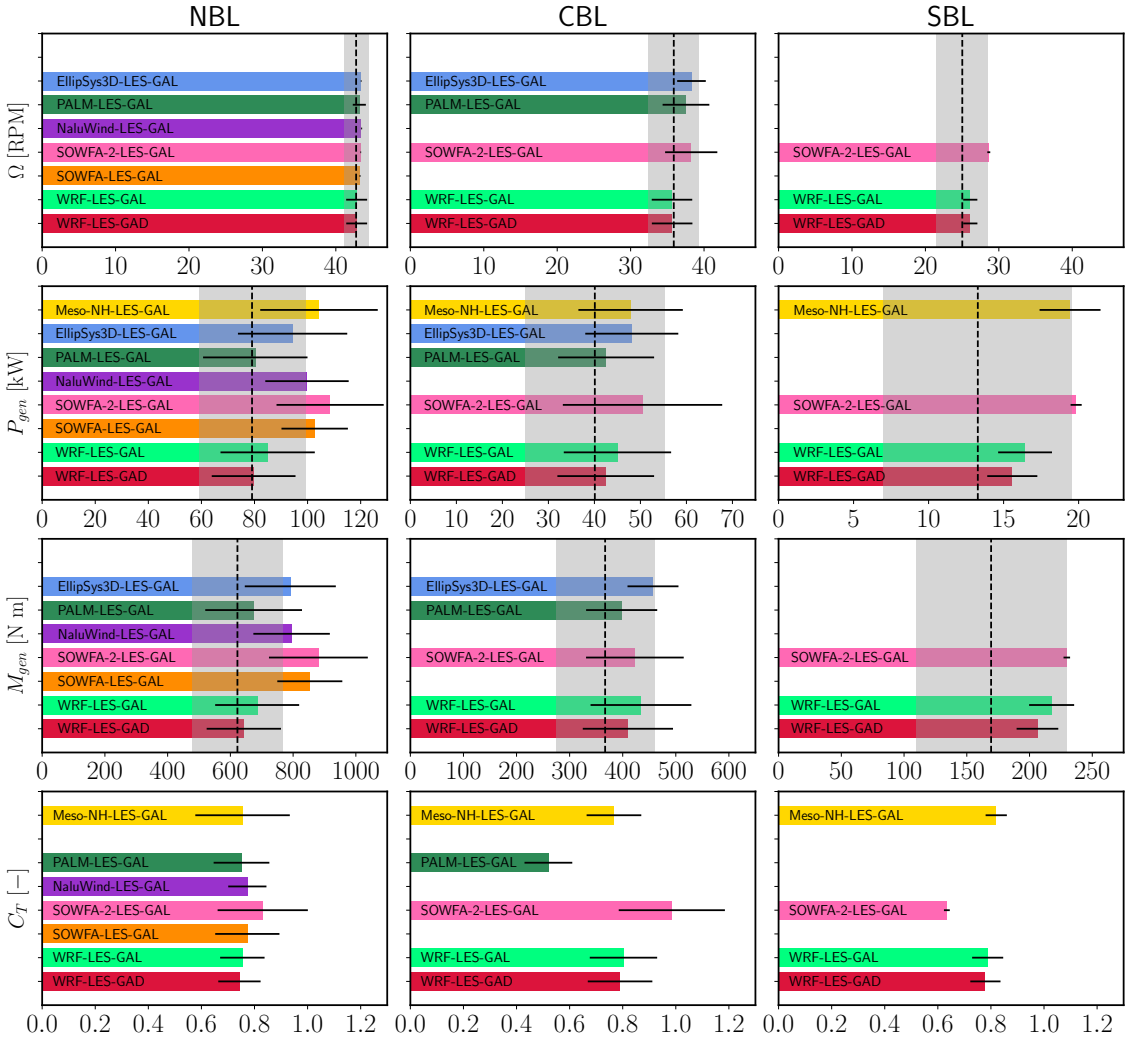

Figure 7.32: Comparison of mean and standard deviations of rotor speed, generator power, generator torque and aerodynamic thrust coefficient for different atmospheric conditions. Vertical black dashed lines show the mean value of measurements, whereas gray shaded regions represent the mean ± standard deviation. Colored horizontal bars show simulation results, and black horizontal lines depict the mean ± standard deviation.

7.3.5 Conclusions

A comprehensive multi-model comparison analysis on the performance of the GAD and GAL models, including the aerodynamic effects of nacelle and tower, has been presented for different atmospheric stability conditions observed in the SWiFT campaign. The effects of the wind turbine parameterization type on the predicted wake characteristics such as mean velocities, variances, vorticity, velocity spectra and co-spectra of u and w velocity components, and distribution of the angle of attack and aerodynamic load along the blade

Table 7.9: Relative errors (REs), $\mathbb{E}$, of wind turbine response quantities between numerical models and ensemble averages of time-averaged field measurements over 10-min periods for three different atmospheric stability conditions (Six ensemble averages for the neutral and stable cases, and five for the unstable case).

LES Model	Neutral			Unstable			Stable		
	$\mathbb{E}_\Omega$ [%]	$\mathbb{E}_{P_g}$ [%]	$\mathbb{E}_{M_g}$ [%]	$\mathbb{E}_\Omega$ [%]	$\mathbb{E}_{P_g}$ [%]	$\mathbb{E}_{M_g}$ [%]	$\mathbb{E}_\Omega$ [%]	$\mathbb{E}_{P_g}$ [%]	$\mathbb{E}_{M_g}$ [%]
EllipSys3D-LES	1.602	19.319	27.077	6.718	20.034	24.570	–	–	–
PALM-LES	1.017	1.548	8.295	4.630	6.121	8.487	–	–	–
NaluWind-LES	1.602	26.179	27.743	–	–	–	–	–	–
SOWFA-2-LES	1.485	37.201	41.463	6.617	25.853	15.281	15.225	49.352	37.165
SOWFA-LES	1.071	29.849	37.067	–	–	–	–	–	–
WRF-LES-GAD	0.178	0.757	3.274	−0.623	5.912	11.688	4.821	17.310	21.805
WRF-LES-GAL	0.165	7.439	10.107	−0.679	12.265	18.400	4.349	23.718	28.483

Note. Ω, P_g, and M_g denote the rotor speed, generator power, and generator torque, respectively. The relative error is quantified as in Table 7.8.

were examined. In addition, the resultant aerodynamic quantities such as rotor speed, generator power and torque, and aerodynamic thrust coefficient, as well as wake velocity deficit profiles, have been compared with results from existing LES codes and experimental data reported in Doubrawa et al. [80], Jézéquel et al. [142]. The results from the GAD and GAL models, including the aerodynamic effects of the nacelle and tower, agree fairly well with other LES codes and measurement data under all conditions, and no significant difference was found between the GAD and GAL models.

The inflow conditions simulated herein highly differ from neutral and unstable conditions, making the stable case challenging to simulate, due to the low turbulence intensity and high shear, although relative errors of turbulence kinetic energy and friction velocity are very small (see Table 7.8). The fact that unrealistic results were obtained for the velocity deficit under stable ABL conditions shows the evidence of wind veer in the simulation between the lower and upper portions of the wind turbine. It has been previously reported in the literature that not only numerical studies [199] but also field experiments [37] have revealed similar results downwind of the wind turbine in stable ABL conditions. There are also analytical models proposed to determine the wake shape in the presence of wind veer [2].

The GAD and GAL models gave similar results by means of wake velocity deficit for all the ABL conditions tested. However, under stable ABL conditions, wake recovery was not as fast in the SOWFA-2-LES model for all reference planes, starting from $x = 3D$. This may be due to improper tuning of the Gaussian kernel width, influencing how aerodynamic forces are smeared onto the computational grid. Also, the differences in the numerical discretization of the models and the coarser spatial resolution used in the current setup can affect the prediction of wake attenuation. For instance, the grid spacing used in the SOWFA-2-LES model for the stable condition was $\Delta x = \Delta y = \Delta z \approx 0.375$ m, which is about six times more refined than in the present GAD and GAL simulations. Such fine

resolutions are required to accurately model very stable atmospheric boundary layers but could not be achieved in the present case due to the limited availability of computational resources. Details of the computational setup of other LES codes can be found in Doubrawa et al. [80]. Since the main focus was given to comparing the GAD and GAL models at a relatively coarse grid resolution, detailed flow features such as root and tip vortices were not captured, and thus advantages of the GAL model over GAD were not evident in the simulations. It should be noted that a direct comparison of the codes is difficult, as all LES codes feature differences in terms of spatial and temporal discretization, grid resolutions, forcing (i.e., inflow conditions), wind turbine parameters, such as the aerodynamic force projection type and kernel width regulating the amplitude of the aerodynamic force and the blade root and tip correction capability, and so on.

The current study reveals that either GAD or GAL model can be used for wake modeling and aerodynamic load assessment of a wind turbine since the relative error between these models is less than 5% under all conditions when a reasonably fine grid resolution with the same inflow field is used. Similar findings, based on the comparison of actuator disk and actuator line models at relatively coarse grid resolutions, have also been reported by other researchers [238, 269]. It can be concluded that the GAD and GAL models have been validated against the results from other LES models and measurement data on the basis of the analyses of the near and far wakes and the aerodynamic response of a single, small-scale wind turbine in stratified ABL flows in flat terrain.

Unlike standard actuator disk modeling approaches where the rotor plane is divided into rings and segments, e.g., the PALM-LES model [205], the current implementation of the GAD model does not adopt a ring-segment approach. In the ring-segment approach, the rotor plane is divided into rings and segments, ensuring that the segments have equal sizes determined by the grid spacing. The process involves calculating the local lift and drag forces per unit area for each segment. Subsequently, these forces are smoothed and interpolated from the center of the rotor segment to each grid point. The omission of fixed radial lines in the rotor plane results in a more computationally efficient representation of the rotor, requiring fewer actuator points compared to the current GAD model. However, at coarse grid resolutions (e.g., 10-20 m), the GAD model is likely to outperform other actuator disk models that use rings and segments to represent the rotor because it contains more actuator points, and therefore a more accurate projection of aerodynamic forces when using a similar computational setup. At relatively fine grid resolutions (e.g., 1-5 m), the GAD model's predictions are as accurate as the GAL model, but the computational overhead is higher. Nevertheless, a thorough analysis is necessary to draw a concrete conclusion. Overall, the GAD and GAL models are able to reproduce the observed wake behavior and the aerodynamic response of the Vestas V27 for the atmospheric conditions tested.

Chapter 8

Applications of the WRF-LES-GAL (WLGL) model: Aerodynamic and aeroacoustic modeling

This chapter presents two real-world applications of the WRF-LES-GAL (WLGL) model to turbulence-resolving simulations of realistic ABL flows over both complex and relatively flat terrains. One of the aims of this chapter is to evaluate the ability of the WLGL model to simulate the interaction between terrain-induced atmospheric boundary layer flows and wind turbines, as well as wind turbine aerodynamic response in complex terrain. First, the WLGL model was forced with realistic large-scale atmospheric turbulence and used to simulate the flow field around a standalone wind turbine under various atmospheric stability conditions observed during the Perdigão campaign in 2017. Second, the Høvsøre wind energy research facility, located in flat terrain in Denmark, was chosen to study the wind turbine wake behavior and noise emissions from an SWT-2.3-93 wind turbine under realistic unstable atmospheric boundary layer conditions observed during a field campaign in May 2006.

Overall, the chapter provides valuable insights into the capabilities of the WLGL model and its potential for improving the understanding of wind turbine wake behavior, as well as the aerodynamic and aeroacoustic response of a real-scale wind turbine in flat and complex terrains, and may help advance the development of more efficient and reliable wind turbine technologies.

8.1 Complex terrain: The Perdigão benchmark

Comparing numerical simulations of wind turbine wakes in realistic ABL flows over complex terrains with full-scale experiments is not always straightforward. Thereby, this section is devoted to presenting some insights into how a single WT and its wake behavior under neutral, unstable, and stable ABL conditions in complex terrain. The Perdigão valley in Portugal, shown in Figure 8.1, was chosen as the test case as it is an excellent case study of three-dimensional flow in complex terrain, specially appropriate to validate numerical simulations of WT wake with experimental data, due to the availability of extensively deployed remote sensing equipment (e.g., German Aerospace Center (DLR) and DTU multi-Doppler lidars). The WLGL model is utilized in order to simulate the period of interest with a multi-scale modeling approach which makes use of five nested domains, with the finest domain having a spatial resolution of 5 m, that are used to dynamically downscale mesoscale flow features to microscale. The WLGL model results have been compared with the experimental data obtained from lidars and met masts.

This section is organized as follows: Section 8.1.1 introduces the motivation of this study. It is followed by a short description of the Perdigão field campaign and selection of the test cases (Section 8.1.2), and some key points on mesoscale-microscale modeling (Section 8.1.3), including the wind turbine parameterization using the WLGL model (Section 8.1.4). In Section 8.1.5, validation of the simulated ABL flow in terms of the time series of wind speed, wind direction, and potential temperature, as well as flow turbulence characteristics, from the WLGL model are compared with experimental data obtained at three 100 m height met masts. In Section 8.1.6, the wake velocity field obtained from the WLGL model, and from the DLR and DTU lidar scans across vertical planes, are compared for the three ABL stability conditions. Simulated one-hour time series of wind turbine power output and thrust are also presented. Conclusions are drawn in the final section (Section 8.1.7).

8.1.1 Motivation

Complex terrains with high wind resources are interesting sites for wind farms, as they are far from the urban environment and, therefore, exempt from strict regulations regarding wind turbine installation on flat terrains close to residential areas [5]. Also, these terrains

This section draws upon the content of an article published in a peer-reviewed international conference proceedings, complemented by another article currently in preparation for submission to a peer-reviewed international journal:

- Kale, B., Buckingham, S., van Beeck, J. and Cuerva-Tejero, A., 2023, May. Multi-scale modeling of a wind turbine wake in complex terrain. In *Journal of Physics: Conference Series* (Vol. 2505, No. 1, p. 012012). IOP Publishing. Paper presented at the Wake Conference 2023, Visby, Sweden, 20-22 June, 2023. DOI: 10.1088/1742-6596/2505/1/012012. Paper presented at the Wake Conference 2023, Visby, Sweden, 20-22 June 2023.
- Kale, B., Buckingham, S., van Beeck, J. and Cuerva-Tejero, A., 2023. Unveiling the impact of complex terrain and atmospheric stability on wind turbine wake dynamics and aerodynamic performance: A quantitative assessment with the WRF-LES-GAL model in a multi-scale modeling approach. *Wind Energy Science* (in preparation).

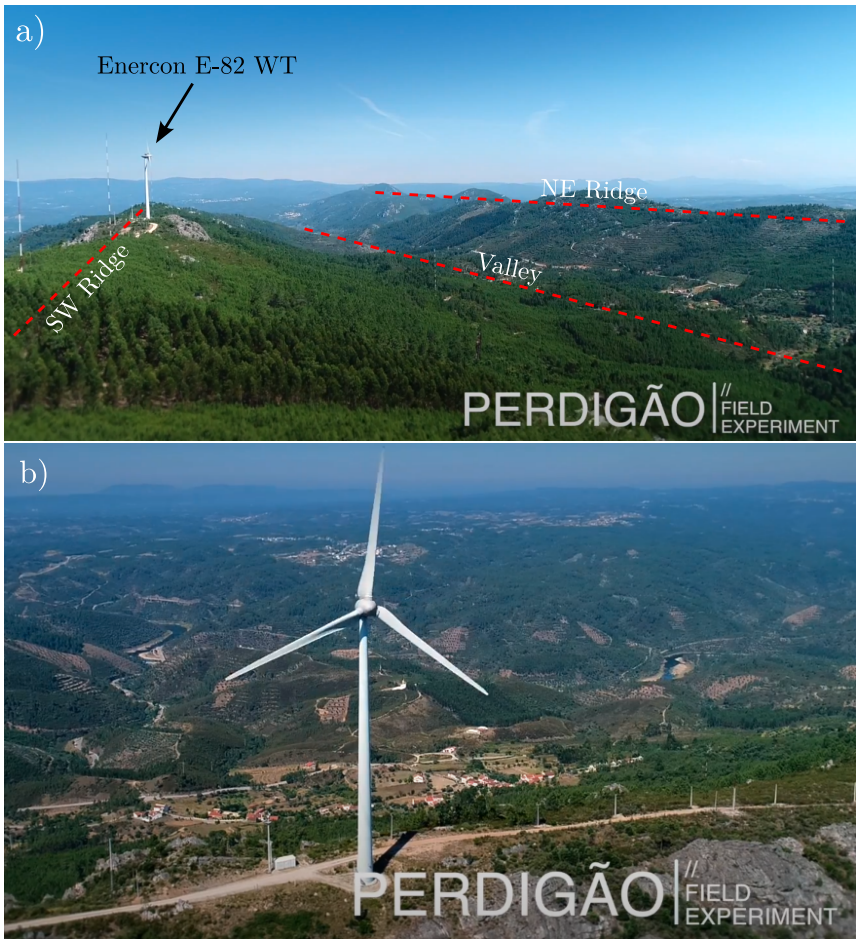

Figure 8.1: Photos of the Perdigão site when looking from the southwest ridge (a) and Enercon E-82 WT installed in the test site (b). Images have been reproduced from the official trailer of the Perdigão 2017 Field Experiment [84].

are better suited for extracting maximum kinetic energy from the wind because the flow in specific locations on mountainous areas (e.g., on ridges) tends to accelerate, enabling wind turbines to generate more power, especially when the winds are perpendicular to mountain ranges [97]. At the top of a hill and downstream from a ridge, there are regions with higher average wind speeds, leading to the higher power output of the wind turbines installed in these areas. However, steep topography can also lead to high flow slope angles and high turbulence regions (even flow recirculation areas) [64, 151, 378], which may cause an increase in wind turbine loading and power variability if the wind turbine location is not carefully decided. The topology of the flow in these regions is affected not only by the topography but also by the stability conditions of the atmosphere [151]. As a result of the dynamic behavior of the ABL during the diurnal cycle, wind turbine performance and wake propagation are affected by the change in atmospheric stability, as the terrain-induced flow and wind turbine wake interact dynamically.

Gaining insight into the wind turbine wake characteristics induced by flow over complex terrains is essential to better assess terrain-wake interaction and maximize the wind energy harvesting from a well-located wind turbine while keeping the WT loading at acceptable

levels. Large changes in topography cause flow separation and recirculation zones downhill of steep terrain [377], being one of the causes that make it difficult to model atmospheric flows over complex terrain. High turbulence levels, gustiness, and sudden changes in wind speed and wind direction found in these regions mean a serious challenge to be reproduced numerically with the accuracy required by wind energy applications [58].

The aim of this study is to validate the WLGL model against field measurements by investigating the ability of the WLGL model to capture a single wake of a wind turbine under neutral, unstable, and stable atmospheric conditions in complex terrain. This study also analyzes the aerodynamic performance of a wind turbine at the Perdigão site. The neutral ABL conditions examined herein are chosen as a reference case for further analysis of unstable and stable ABL conditions. Purely neutral atmospheric stability conditions are rarely found in the atmosphere, as the characteristics of the ABL change during the diurnal cycle [156]. This choice also serves as a good reference case because it involves minimal (sometimes near zero) thermal effects for near-neutral ABLs, simplifying the atmospheric physics to be modeled. Special attention is paid to the understanding of turbulence characteristics, wake propagation, characterization of aerodynamic loads on the wind turbine, and power generation for all the ABL conditions tested. The predicted microscale flow structures and wake behavior of the wind turbine are validated by directly comparing the WLGL model results with high-frequency experimental data from two met masts on the ridges and one met mast in the valley, as well as remote sensing data from DLR and DTU lidars.

8.1.2 The Perdigão field campaign and selection of the test cases

As a part of the New European Wind Atlas (NEWA) validation experiment, funded by the European Union [203], an Intensive Operation Period (IOP) campaign took place in 2017, from May 1^{th} to June 15^{th}, during the Perdigão field experiment in Portugal [97]. A large group of scientists, engineers, and research organizations from all around the world, worked in collaboration to explore the microscale flow over a complex terrain region in Perdigão Valley, which consists of two parallel mountain ridges at about 460 m above sea level that extends over 2 km distance [271]. The prevailing wind direction was perpendicular to the orientation of the ridges in general (southwesterly winds) [97].

A rich variety of flow types such as buoyancy-driven anabatic (upslope) and katabatic (downslope) flows, valley flows driven by large temperature gradients along the valley, and separated flows on the ridges that are caused by the interaction of topography with synoptic flows are observed at the test site. Due to the comprehensive deployment of experimental means, the Perdigão database offers a unique opportunity to investigate the wind turbine wake dynamics under various atmospheric stability conditions in complex terrain [97].

Time series of different flow variables, such as wind speed, wind direction, temperature, and so on, at several locations at the Perdigão test site were collected from met masts,

lidars, sodars, radiosondes, microphones, a tethered lifting system (TLS), etc., installed by several research groups from different institutions [97]. A single Enercon E-82 2MW WT is located on the southwest ridge.

In the present work, the ABL flow over Perdigão valley has been modeled for a one-hour period when the actual atmospheric conditions at the site were observed to be near-neutral (measurement period on 09/05/2017 between 22:00-23:00 (UTC)), unstable (measurement period on 28/05/2017 between 16:00-17:00 (UTC)) and stable (measurement period on 09/05/2017 between 04:00-05:00 (UTC)). 24-hour time series of horizontal wind speed, U_h (a-b) and wind direction, β (c-d) at hub height, 100-10 m potential temperature gradient, $d\theta/dz$ (e-f), kinematic heat flux, $\overline{w'\theta'}$ (g-h), and Obukhov length, L, at 10 m (i-j), obtained from TSE04 met mast for neutral, unstable, and stable ABL conditions, are given in Figure 8.2. The periods of interest for all the atmospheric stability conditions are highlighted in blue, green, and red. Experimental data have been subsampled to 5-min intervals.

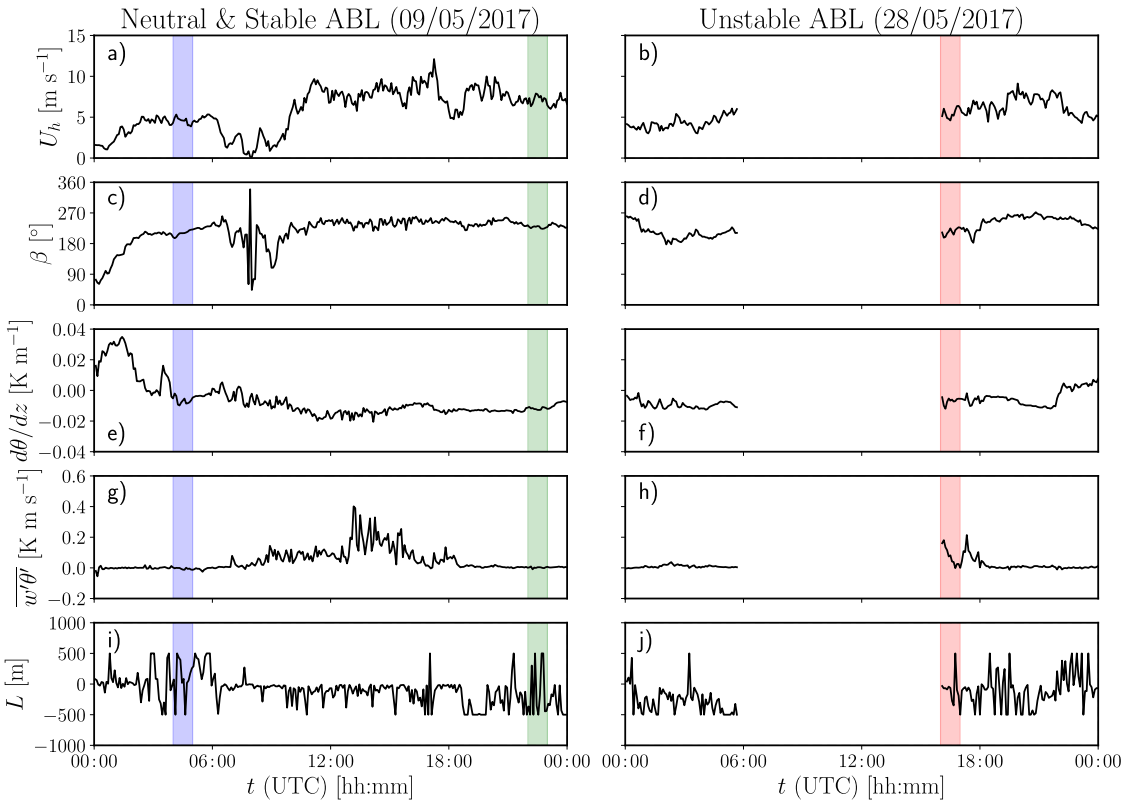

Figure 8.2: 24-h time series of horizontal wind speed, U_h (a-b), and wind direction, β (c-d) at hub height, 100-10 m potential temperature gradient, $d\theta/dz$ (e-f), kinematic heat flux, $\overline{w'\theta'}$ (g-h), and Obukhov length, L, at 10 m (i-j), obtained from the TSE04 met mast for the neutral, unstable, and stable ABL conditions. (▭), (▭), and (▭) shaded regions indicate the periods of interest for the stable, neutral, and unstable cases, respectively. t (UTC) stands for Coordinated Universal Time in hours and minutes. Data have been subsampled to 5-min intervals. Values of L are confined to the range $-500 \leq L \leq 500$ to avoid extremely small and large values.

In order to determine the state of the ABL, several parameters such as the Obukhov length, L, which is the ratio between buoyant and mechanical effects on the atmospheric turbu-

lence defined in Equation (3.19), can be estimated. In complex terrain, nondimensional Froude number, $\mathrm{F_L}$, can also be used to determine the atmospheric stability in areas where hills or mountainous regions occupy a significant portion of the ABL [326]. It is defined as

$$\mathrm{F_L} = \frac{\pi V}{N_{BV} L_h}, \tag{8.1}$$

with V being the characteristic velocity in the ABL, N_{BV} is the Brunt-Väisälä frequency given by Equation (3.25) and L_h is the characteristic downwind length of the hill (e.g., mountain ridge width). In this work, potential temperature gradient, $\partial\overline{\theta}/\partial z$, is calculated from the potential temperature gradient between 100 and 10 m, while other values are calculated at 100 m, with $L_h = 586.5$ m at the southwest (SW) ridge and $L_h = 530.0$ m at the northeast (NE) ridge, respectively [253, 367]. The Froude number is sometimes defined without the factor π [151].

For $\mathrm{F_L} \gg 1$, the wind flow is supercritical, meaning that boundary layer separation may occur on the lee side of the mountain due to strong winds. $\mathrm{F_L} \ll 1$ corresponds to subcritical flow and the ABL is statically very stable and mountain waves may form [326]. In the case of $\mathrm{F_L} \approx \infty$, the state of the ABL can be classified as either unstable or neutral and recirculation regions may form [367]. Measured stability parameters obtained from different met masts at Perdigão test site are given in Table 8.1. The state of the ABL can be classified based on the parameters given in Table 3.1. According to the stability parameters tabulated in Table 8.1, the periods of interest for all the cases considered in this work can be classified as near-neutral, unstable, and stable, based on the stability parameters obtained from TSE04 mast. The prevailing wind direction at hub height is approximately perpendicular to the SW ridge, and thus other met masts stay in the wake of the first ridge during the periods of interest. Although the mean values of Obukhov length and kinematic heat flux indicate that the state of the ABL was stable during the period of interest, the 100-10 m temperature gradient presented negative values, resulting in an infinite average value of Froude number calculated from TSE04 met mast. In addition, the stability parameter, z/L, evidences that the state of the ABL was not completely neutral, unstable, or stable due to the transition from one stability state to another for the respective periods; therefore, for clarity and convenience, all states are classified as neutral, unstable, and stable.

Sonic anemometers installed at different heights above ground level are utilized to acquire 20 Hz data from the three 100 m met masts (TSE04, TSE09, and TSE13 that are located on the SW ridge, in the valley, and on the NE ridge, respectively (see Figure 8.5). These high-frequency measurement data (NCAR/EOL Quality Controlled High-rate Integrated Surface Flux System (ISFS) surface flux data, geographic coordinate, tilt corrected, version 1.1 [349]) are used as a reference to validate the WRF-LES results in terms of horizontal wind speed, wind direction, spectra and cross-spectra of flow velocity components, and cross-spectra of vertical momentum and heat flux, respectively.

Lidar data from two systems installed by DLR (DLR85 and DLR86, which are located in

Table 8.1: Mean hub height horizontal wind speed, $\overline{U}_h$, friction velocity, u_*, surface kinematic heat flux, $(\overline{w'\theta'})_s$, Obukhov length, L, turbulence intensity, $\overline{TI}$, stability parameter, z/L, and nondimensional Froude number, $\mathrm{F_L}$, obtained from experimental data at different met mast locations for neutral, unstable, and stable ABL conditions.

		Case 1: Neutral			Case 2: Unstable			Case 3: Stable		
Parameter	Unit	TSE04	TSE09	TSE13	TSE04	TSE09	TSE13	TSE04	TSE09	TSE13
$\overline{U}_h$	[m s^{-1}]	7.3	2.4	6.3	5.5	2.6	5.0	5.2	2.5	5.4
u_*	[m s^{-1}]	0.31	0.40	0.57	0.49	0.45	0.43	0.33	0.30	0.42
$(\overline{w'\theta'})_s$	[K m s^{-1}]	0.002	−0.004	0.009	0.073	0.050	0.080	−0.006	−0.010	−0.007
L	[m]	1022.3	58.6	−333.3	−106.2	−285.8	−99.8	84.5	11.4	242.6
$\overline{TI}$	[%]	8.1	42.6	21.4	14.1	40.9	18.6	9.0	21.2	8.7
z/L	[−]	0.010	0.171	−0.030	−0.094	−0.035	−0.100	0.118	0.877	0.041
$\mathrm{F_L}$	[−]	∞	–	2.2	∞	–	2.5	∞	–	1.3

Note. $\overline{U}$ and $\mathrm{F_L}$ are calculated at 100 m, while u_*, $(\overline{w'\theta'})_s$, and L are calculated at $z = 10$ m. $\overline{TI}$ is calculated at 80 m and includes the contribution of the three velocity components. Experimental values are calculated from the experimental data subsampled to 5-min intervals. Values of L are confined to the range $-500 \leq L \leq 500$ to avoid extremely small and large values. TSE04, TSE09, and TSE13 towers are located on the southwest ridge, in the valley and on the northeast ridge, respectively (see Figure 8.5).

the valley and on the NE ridge, respectively, are also employed for comparison of experimental and numerical data presented in this work [364]. These lidars are of the Range Height Indicator (RHI) type and scan the flow velocity field along radial directions in a vertical plane containing the wind turbine tower. This layout allows the structure of the WT wake and valley flow to be captured when the wind blows in the WT-lidar direction. The azimuth angle of DLR lidars in the horizontal plane is approximately constant; thus, the scanning trajectory is perpendicular to the wind turbine rotor. Likewise, DTU lidars have a constant azimuth angle but scan the offset transect (see Figure 8.5). However, as the terrain has a similar topography along the nearly parallel transects (the actual distance between these transects is roughly 182.4 m on the first ridge and 129.6 m on the second ridge), DTU lidar scans can provide information about wind flow topology along the offset transect without being affected by the wind turbine wake. Note that, DLR85 and DLR86 lidar scans (sweeps) take about 53 s and 113 s, while a DTU multi-Doppler lidar completes a single sweep in about 24 s. Besides, the radial velocities measured by the lidars have been converted into horizontal velocities for comparison. Converting radial velocity to horizontal velocity leads to larger errors at higher elevation angles but smaller errors along the valley near the wind turbine where the lidar beam is nearly horizontal [367]. This transformation ensures that the vertical positions along the lidar beam, perpendicular to the mean flow direction at the lidar location, have zero horizontal velocity.

8.1.3 Mesoscale-microscale modeling using WRF-LES model

The five-domain nested multi-scale simulation set-up for the WLGL model is shown in Figure 8.3 and details are provided in Table 8.2. An online mesoscale-microscale coupling approach, with five one-way nested domains provided by the WRF model, was utilized.

Mesoscale simulations were performed with two nested domains, with horizontal resolutions of $\Delta x = 5000$ m and 1000 m, using the S-H PBL scheme. Three microscale domains, with horizontal resolutions of $\Delta x = 125$ m, 25 m, and 5 m, were run in LES mode using

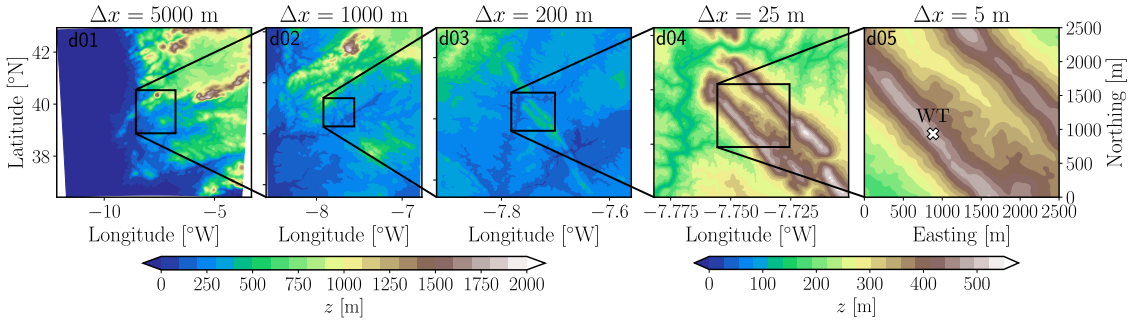

Figure 8.3: Nested domain configuration from the multi-scale WRF-LES simulation. All nested domains centered on the Perdigão site are colored by terrain height where $z = 0$ m corresponds to sea level. The five domains have spatial resolutions of 5000 m, 1000 m, 200 m, 25 m, and 5 m. Domain dimensions and other model configuration parameters are given in Table 8.2.

a 1.5-order TKE SFS turbulence scheme [71]. Vertical grid nesting was applied to all domains to allow for vertical grid refinement over nested domains by reducing the overall time required to run the model.

Temporal discretization was achieved by using a third-order Runge-Kutta scheme, with fifth-order horizontal and third-order vertical advection schemes. Physical parameterizations include the Eta (Ferrier) scheme for microphysics [280], the Noah land surface model [47], the Rapid Radiative Transfer Model for longwave radiation [221] and the Dudhia shortwave radiation model [86]. Revised MM5 surface layer scheme was used on all domains [145]. Shading effects on the surface heat flux were enabled by setting the *topo_shading* parameter to 1. The model top was placed at 150 hPa (about 13.5 km in altitude) to take into account radiation and cloud effects at the tropopause [355], and for the upper 5 km of the domain, a Rayleigh damping layer was used to dampen the spurious waves that could be reflected from the model top.

A high-resolution reanalysis dataset (e.g., European Centre for Medium-Range Weather Forecasts (ECMWF ERA5) [128]) for initial and lateral boundary conditions was used to provide the atmospheric forcing required on all domains. The Cell Perturbation Method (CPM) [234], was applied to trigger the generation of realistic atmospheric turbulence on

Table 8.2: Domain dimensions and model configuration parameters for the analysis of the ABL flow in Perdigão valley.

Domain	$N_x \times N_y \times N_z$	Δx [m]	Δz [m]	Δt [s]	Turb. model	CPM	Spin-up [min]
d01	$141 \times 141 \times 41$	5000	∼80	30	S-H	No	600
d02	$151 \times 181 \times 61$	1000	∼50	6	S-H	No	600
d03	$241 \times 241 \times 81$	125	∼30	0.6	1.5-order TKE	Yes	420
d04	$271 \times 271 \times 121$	25	∼15	0.06	1.5-order TKE	Yes	60
d05	$501 \times 501 \times N_z$	5	∼5	0.0075	1.5-order TKE	Yes	10

Note. N_x, N_y, and N_z stand for the number of grid points whereas $\Delta x, \Delta y$, and Δz represent the spatial grid resolutions in the x, y, and z directions, respectively. For d05, $N_z = 201$ for the neutral case and $N_z = 271$ for the other stability cases. Note that $\Delta x = \Delta y$ and Δz is set close to the values given in the table, because of WRF's terrain-following eta coordinate system in the vertical direction. Δt is the computational time-step size. CPM denotes the Cell Perturbation Method [234].

the LES domains. The Coordination of Information on the Environment (CORINE) Land Cover (CLC) 2012 raster dataset with a spatial resolution of 100 m [26] was used to account for tall vegetation. These data are transformed into United States Geological Survey (USGS) land use types to obtain surface roughness lengths for WRF [264]. The latest CORINE database, CLC 2018, was not used in the ABL flow analysis in Perdigão because the vegetation was affected by an intense fire incident after the Perdigão measurement campaign took place [57]. In order to resolve flow features in the valley surface, high-resolution terrain data from the Shuttle Radar Topography Mission (SRTM) with a spatial resolution of 30 m was also used [95].

The spin-up of the nested domains was achieved by performing a set of restart model runs. This is necessary to obtain well-developed turbulent structures within the finest resolution domain, which contains the modeled wind turbine. Domains d01 and d02 were spun up for three hours, prior to activating d03. Three domains were then spun up for an additional six hours period before starting d04. All four domains were spun up for another 50-min. Next, the finest resolution LES domain, d05, including the WLGL model, was activated to allow the development of fine-scale turbulent structures within the atmospheric boundary layer. The final restart run, which is the run analyzed herein, took 70-min (e.g., for the neutral case, these results correspond to the time window between 21:50-23:00 (UTC) on 09/05/2017). The first 10 minutes of the final restart run were discarded to allow the turbulent flow field to be thoroughly mixed across domain d05, prior to running the actual simulation for the corresponding time frame.

8.1.4 Wind turbine wake modeling using the WLGL model

The wind turbine operating in the test field is an Enercon E-82 2MW. Unfortunately, the design data required for proper GAL-based modeling is unavailable. Hence, a publicly available design database of a similar wind turbine, the generic Vestas V80 2MW machine [54], was used. The Enercon WT has 80 m hub height and 82 m rotor diameter, whereas the Vestas wind turbine has 78 m hub height and 80 m rotor diameter. Nacelle and tower aerodynamic effects were parameterized utilizing an approach similar to that of the WLGL model.

The current WLGL model uses a five-region rotor angular velocity controller algorithm [147]. Furthermore, a simple pitch controller mechanism was used to control the blade pitch angle at speeds above rated wind speed. The pitch controller was active only for a limited time when the inflow wind speed seen by the rotor at $1D$ upstream exceeded the rated rotor speed. Minor differences between the two wind turbines are not expected to significantly affect the results because the mean wind speed considered during the periods of interest is below the rated speed of the modeled WT, and for those wind speeds, the C_T curves for both wind turbines are very similar. The stationary curves of power, thrust, as well as their coefficients, versus wind speed, are presented in Figure 8.4 for both wind turbines.

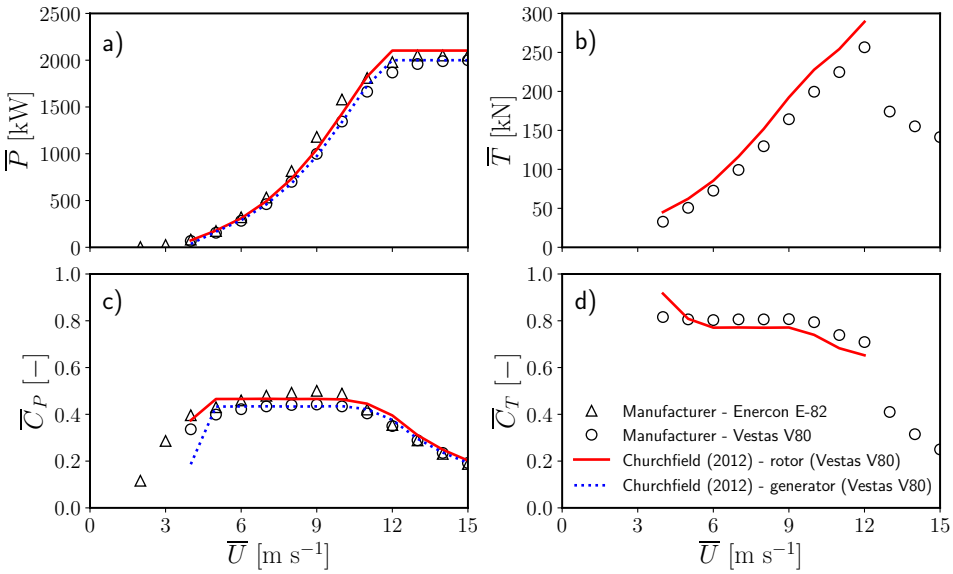

Figure 8.4: Stationary curves of mean power, $\overline{P}$ (a), thrust, $\overline{T}$ (b), power coefficient, $\overline{C}_P$ (c) and thrust coefficient, $\overline{C}_T$ (d), versus mean wind speed, $\overline{U}$, of the generic Vestas V80 2MW [54] and Enercon E-82 2MW [366] wind turbines.

8.1.5 Validation of the ABL flow in the Perdigão site

Figure 8.5 shows the terrain elevation and layout over the Perdigão valley, including the locations of the wind turbine, met masts, and lidars at the test site. Wake and offset transects, indicated by dotted and dashed black lines, respectively, are used to analyze the wind flow field in vertical planes, whereas time series and vertical profiles of horizontal wind speed, wind direction, and potential temperature gradient are obtained from 100 m DTU met masts (TSE04, TSE09, and TSE13) and are used as a reference to validate the WLGL results.

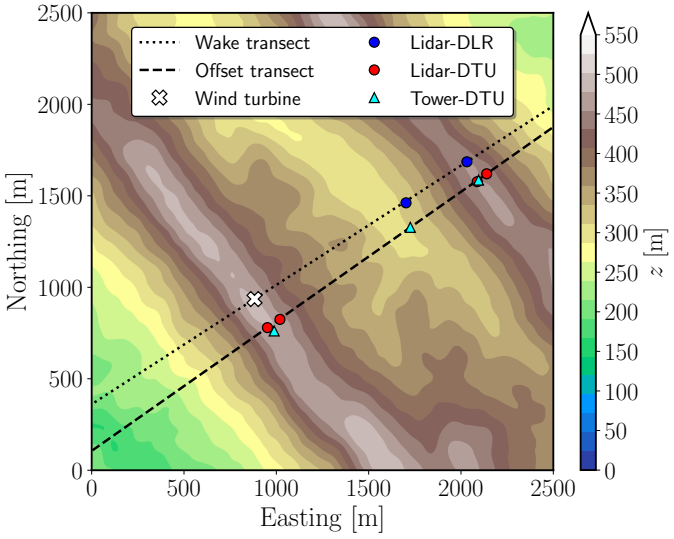

Figure 8.5: WRF-LES-d05 domain showing the locations of the wind turbine, DLR and DTU lidars, 100 m DTU met masts, wake and offset transects. The figure is colored by terrain height where $z = 0$ m corresponds to sea level.

Time series and vertical profiles

For all the cases analyzed herein, the sampling frequency of the met mast measurements is 20 Hz, whereas the WRF-LES outputs are recorded every time step during 1-hour simulation period, corresponding to a sampling frequency of about 133 Hz; therefore, the numerical data were subsampled to 0.05 s intervals to match the experimental data.

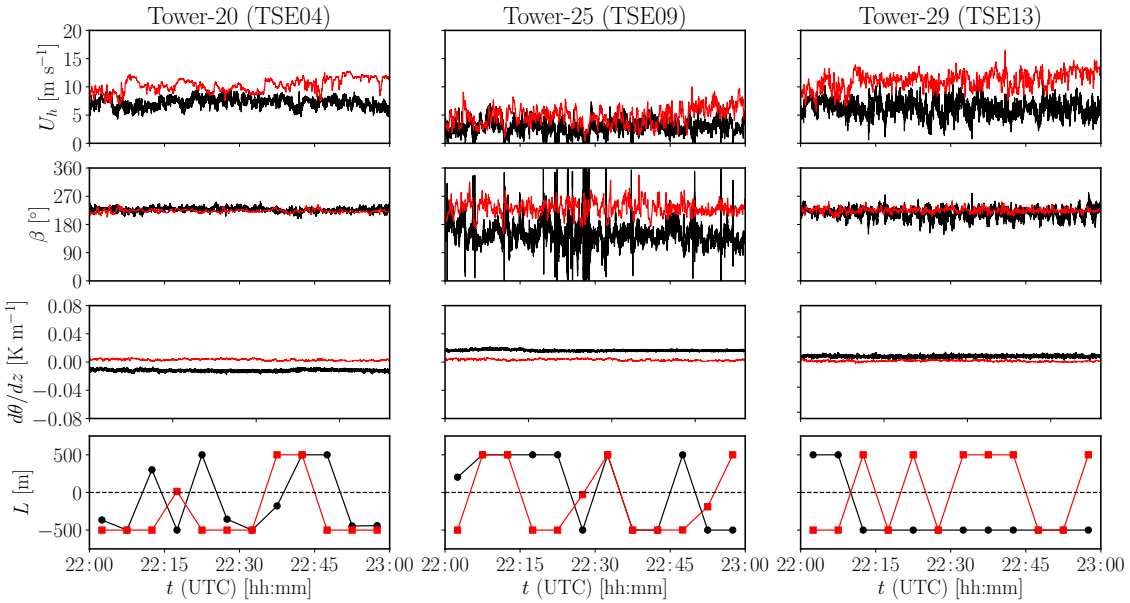

Figure 8.6: Comparison of time series of horizontal wind speed, U_h (first row), wind direction, β (second row) at hub height, the potential temperature gradient, $d\theta/dz$ (third row), and the Obukhov length, L (fourth row) at 10 m, from TSE04 (first column), TSE09 (second column), and TSE13 (third column) met masts, along with corresponding numerical results from WRF-LES-d05. Note that the numerical data were subsampled to 0.05 s intervals for U_h, β, $d\theta/dz$ and 300 s intervals for L to match the experimental data. t (UTC) stands for Coordinated Universal Time in hours and minutes. (——) corresponds to experimental data and (——) denotes the WRF-LES results from domain d05. The results correspond to the neutral case. The values of L are constrained within the range of $-500 \leq L \leq 500$ to prevent the occurrence of exceedingly small or large values.

Figure 8.6 presents time series of horizontal wind speed and wind direction at hub height, 100-10 m potential temperature gradient, and the Obukhov length at 10 m from the three DTU met masts and WRF-LES model for the 1-hour period analyzed during the neutral conditions. Simulated horizontal wind speeds at hub height were overestimated compared to the experiments. Also, the WRF-LES model predicted the wind direction on the ridges (TSE04 and TSE13) reasonably well, yet large variations were observed in the valley (TSE09), most probably due to the difficulties in capturing the larger turbulence mixing in this region. Positive potential temperature gradients close to zero and Obukhov lengths greater than $|L| \geq 500$ (slightly greater than $L > 0$ around 22:15 (UTC)) were observed in the model results, meaning that near-neutral (sometimes near-neutral-stable) conditions were modeled during the period of interest. The experimental data collected from the met masts suggests a transitional atmospheric regime prevailing across the ridges, characterized by a negative temperature gradient and an Obukhov length, indicating a transition zone

between unstable and stable ABL conditions.

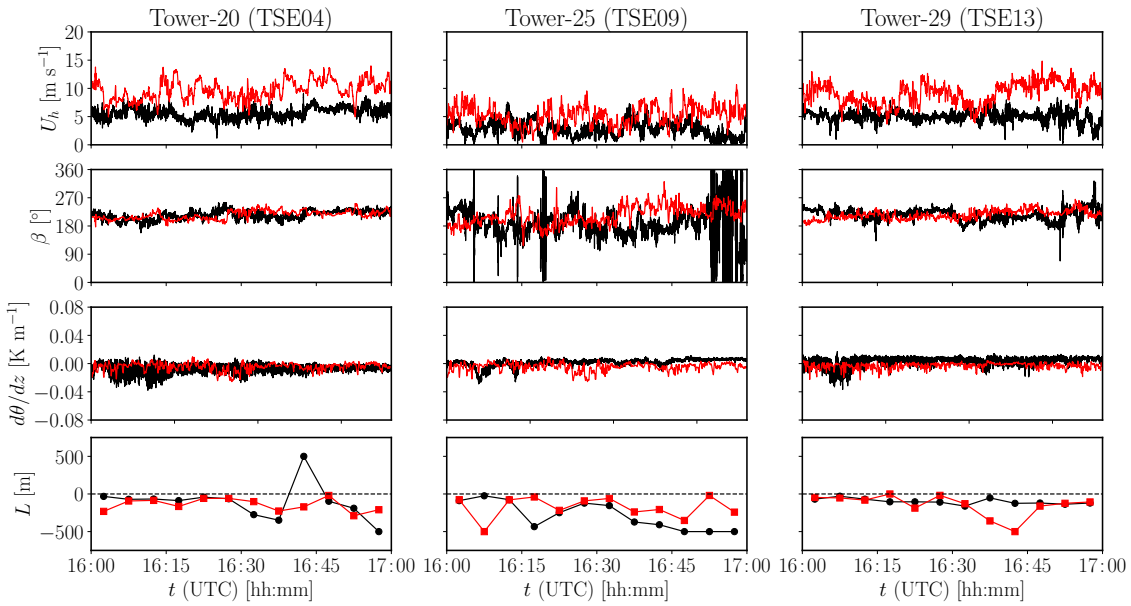

Figure 8.7: Same as in Figure 8.6, but for the unstable case.

Figure 8.7 shows the time series of the aforementioned atmospheric quantities for the unstable case. The WRF-LES model overpredicted the magnitude of the horizontal wind speed on the ridges, as in the neutral case. For the wind direction and 100-10 m temperature gradient, the results from the WRF-LES model match the experimental data quite well at all tower locations. The time series of $d\theta/dz$ exhibited significant variations both on the ridges and in the valley, while the time series of U_h and β displayed increased variability, particularly within the valley. Both the experimental and modeled data consistently show lower negative values of L, indicating unstable ABL conditions during the respective period of interest.

Wind speed and wind direction at hub height and potential temperature gradient between 100 m and 10 m, as well as the Obukhov length calculated at 10 m above ground for the stable case, are also compared with measurements from met masts in Figure 8.8. The modeled wind speed at 80 m follows the observations in general, with a slight overestimation in the valley and on top of the NE ridge. The hub height wind direction results from the WRF-LES model agreed quite well with the observations at all tower locations, except for the first 15-min where an overestimation of about 40° on top of the two ridges and $\sim$120° in the valley was observed. The modeled potential temperature gradient overestimated the experimental data on the SW ridge, showing stably stratified ABL conditions over the period of interest, while the measured potential temperature gradient was indicative of a transitional atmospheric state that varied between near-stable and near-unstable ABL conditions. Both the WRF-LES model and observations concur that the ABL was in a stable state in the valley and on top of the NE ridge, as substantiated by the presence of lower values of L.

1-hour mean vertical profiles of various variables with their respective standard deviations

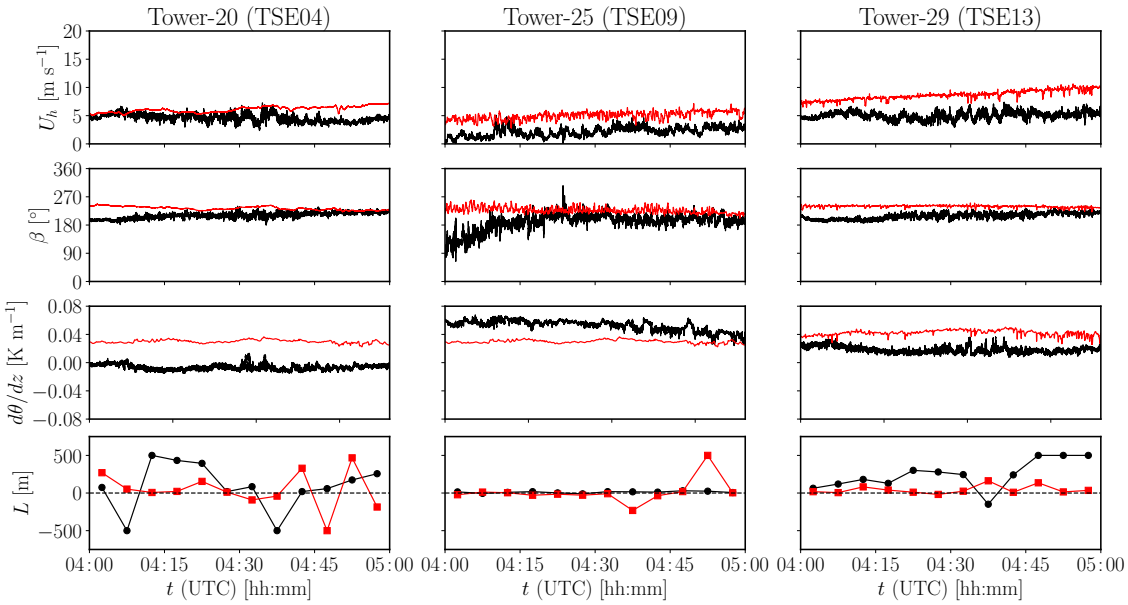

Figure 8.8: Same as in Figure 8.6, but for the stable case.

over the period of interest, for the neutral case, are presented in Figure 8.9. The overprediction of wind speed exhibited by the WRF-LES model on the ridges is likely due to the overestimated flow acceleration on the slopes. Nevertheless, model estimates agree fairly well with the TSE09 met mast data below hub height. The wind speed in the valley does not increase monotonically with height, probably due to the presence of height-dependent transient atmospheric processes and forcing. WRF-LES model predicts the wind direction reasonably well at different heights on the ridges. This is expected because, as it has already been described, the predominant wind direction in the test field is approximately perpendicular to the orientation of the ridges, according to the annual climatology at Perdigão [97]. Nonetheless, a significant bias prevailed within the valley, rendering the WRF-LES model unable to accurately capture the observed wind veer at the TSE09 met mast location. The vertical profiles of the 1-hour average potential temperature predicted by the numerical model do not vary significantly at the met mast locations. Turbulence intensity profiles demonstrate a strong agreement along the SW ridge and within the valley (up to 60 m), but it's notable that the modeled turbulence intensity levels consistently underestimate those observed at all measurement heights along the NE ridge. The relative errors between the modeled and measured values are depicted in Table 8.3.

In Figure 8.10, mean vertical profiles of the variables mentioned above, with their respective standard deviations, throughout the period of interest for the unstable case are presented. Although modeled vertical wind speed profiles at met mast locations overpredicted the experimental data at all heights, the WRF-LES model accurately predicted the mean wind direction and its variability on the ridges. Yet, an overestimation was observed with acceptable variation in the modeled wind direction in the valley. For potential temperature, the model predictions in the valley were better than those on the ridges, as opposed to the predicted wind direction levels at these particular locations. Nevertheless,

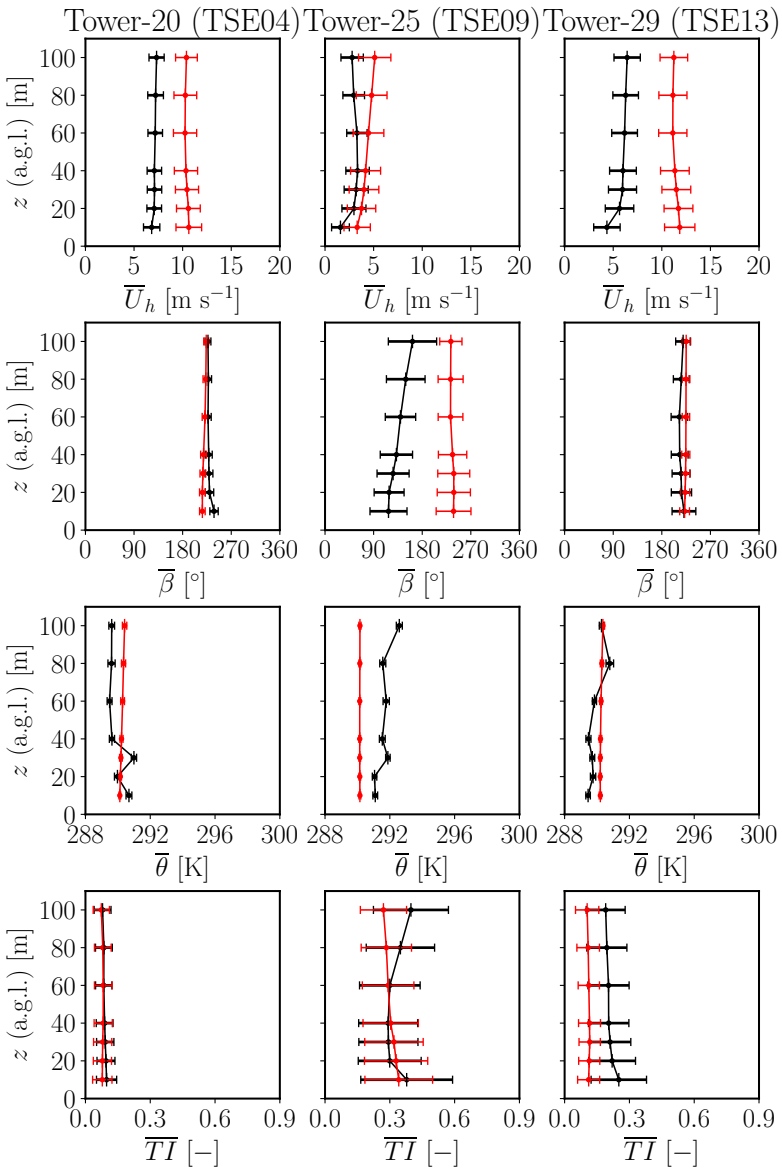

Figure 8.9: Comparison of the vertical profiles of 1-hour average horizontal wind speed, $\overline{U}_h$ (first row), wind direction, $\overline{\beta}$ (second row), potential temperature, $\overline{\theta}$ (third row), and turbulence intensity, $\overline{TI}$ (fourth row), obtained from TSE04 (first column), TSE09 (second column), and TSE13 (third column), and WLGL model. Black and red horizontal lines indicate the standard deviation around the mean value obtained during the averaging period of the measurement data and simulation results, respectively (a.g.l refers to above ground level). (——) corresponds to experimental data and (——) denotes the WRF-LES results from domain d05. The results correspond to the neutral case.

there was a consistent disparity of approximately 1-2 K in mean potential temperature across all heights above ground level. The WLGL model captured the mean turbulence intensity levels between 10-100 m on the ridges, but an underestimation of about $\overline{TI} \approx 0.1$ was observed at the TSE09 met mast location within the valley.

Figure 8.11 shows time-averaged vertical profiles of wind speed, wind direction, potential temperature, and turbulence intensity from met masts TSE04, TSE09, and TSE13 during stable ABL conditions. Results indicate that the wind speed profiles from the WRF-LES

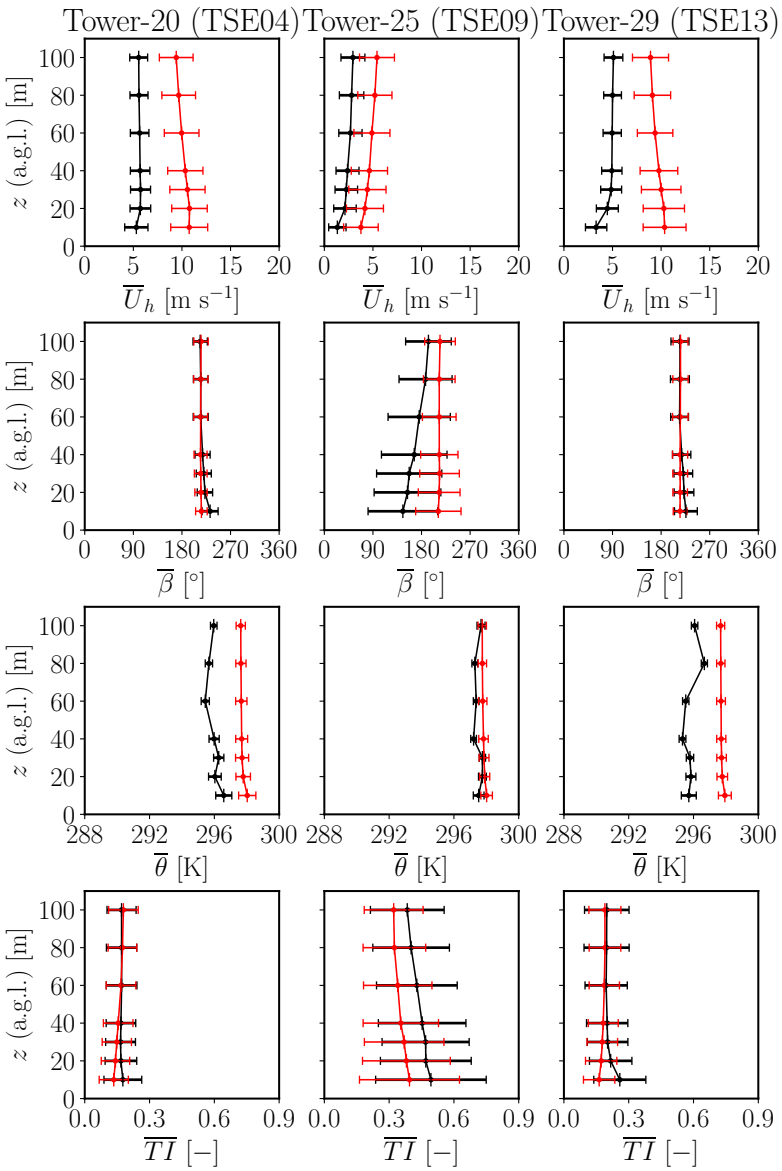

Figure 8.10: Same as in Figure 8.9, but for the unstable case.

model agree fairly well with the experimental data, with the highest error, which is on the order of 5 m s^{-1} near the surface (10 m) on top of the NE ridge. For the wind direction profiles, although the errors are at acceptable levels at all measurement heights on top of the two ridges (e.g., $-20° < \mathbb{E}^{\overline{\beta}}_{\text{bias}} < 40°$), the modeled wind direction profile overpredicted the experimental data, as in Figure 8.9. The potential temperature profile from met mast TSE04 showed near-unstable conditions, due to a higher potential temperature near the ground than observed at 100 m; however, the WLGL model's prediction depicted stable ABL conditions. Conversely, a comparable trend in the potential temperature profile was evident both in the valley and on top of the NE ridge. Nevertheless, the WLGL model exhibited an overestimation compared to the experimental data. The predicted mean $\overline{TI}$ profiles slightly underestimated the experimental data on the ridges, while a more significant bias was noted at all heights along the met mast within the valley in the model results.

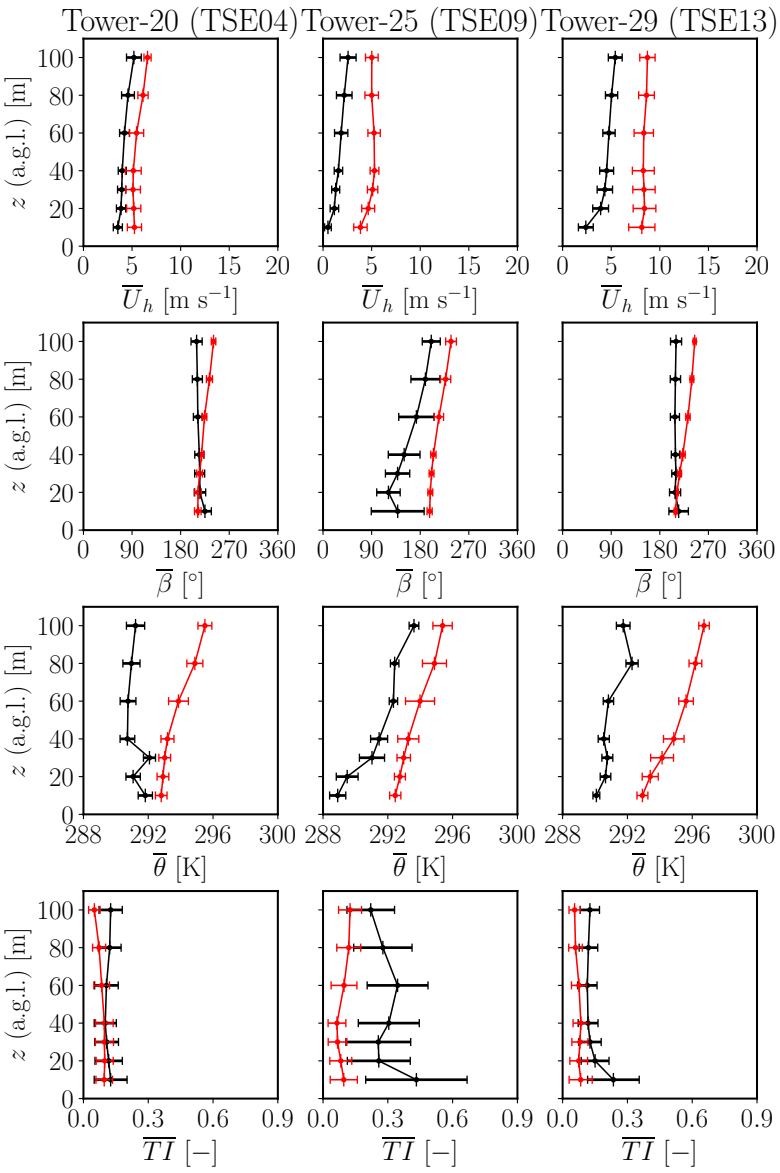

Figure 8.11: Same as in Figure 8.9, but for the stable case.

An error analysis based on bias and RMS errors, $\mathbb{E}_{\text{bias}}$ and $\mathbb{E}_{\text{rms}}$, respectively, for hub height mean horizontal wind speed, $\overline{U}_{hub}$, wind direction, $\overline{\beta}_{hub}$, 100-10 m temperature gradient, $\partial\overline{\theta}/\partial z$, surface kinematic heat flux, $(\overline{w'\theta'})_s$, at 10 m, friction velocity, u_*, at 10 m, and hub height turbulence intensity, $\overline{TI}_{hub}$, between the WRF-LES results and field measurements during the periods of interest for the three different atmospheric stability conditions are given in Table 8.3. It has been noted that model configurations used for the high-resolution WLGL simulations may not have been optimal for each stability case. Enhancing model performance can be achieved by exploring various PBL schemes, SFS models, and combinations of atmospheric physics schemes. Additionally, addressing improvements in land surface dynamics could further boost model performance.

Table 8.3: Bias and RMS errors of mean hub height horizontal wind speed, $\mathbb{E}_{\text{bias}}^{\overline{U}_{hub}}$ and $\mathbb{E}_{\text{rms}}^{\overline{U}_{hub}}$, wind direction, $\mathbb{E}_{\text{bias}}^{\overline{\beta}_{hub}}$ and $\mathbb{E}_{\text{rms}}^{\overline{\beta}_{hub}}$, 100-10 m temperature gradient, $\mathbb{E}_{\text{bias}}^{\partial\overline{\theta}/\partial z}$, surface kinematic heat flux, $\mathbb{E}_{\text{bias}}^{(\overline{w'\theta'})_s}$, at 10 m, friction velocity, $\mathbb{E}_{\text{bias}}^{u_*}$, at 10 m, and hub height turbulence intensity, $\mathbb{E}_{\text{bias}}^{\overline{TI}_{hub}}$, between WRF-LES results and field measurements during 1-hour for the three different atmospheric stability conditions.

Parameter	$\mathbb{E}_{\text{bias}}^{\overline{U}_{hub}}, \mathbb{E}_{\text{rms}}^{\overline{U}_{hub}}$ [m s^{-1}]	$\mathbb{E}_{\text{bias}}^{\overline{\beta}_{hub}}, \mathbb{E}_{\text{rms}}^{\overline{\beta}_{hub}}$ [°]	$\mathbb{E}_{\text{bias}}^{\partial\overline{\theta}/\partial z}$ [K m^{-1}]	$\mathbb{E}_{\text{bias}}^{(\overline{w'\theta'})_s}$ [K m s^{-1}]	$\mathbb{E}_{\text{bias}}^{u_*}$ [m s^{-1}]	$\mathbb{E}_{\text{bias}}^{\overline{TI}_{hub}}$ [−]
Case1: Neutral						
TSE04	3.061, 3.427	−4.757, 9.372	0.0151	−0.0070	0.0678	−0.0063
TSE09	1.844, 2.665	83.090, 93.451	−0.0165	0.0107	−0.1177	−0.0932
TSE13	4.862, 5.247	8.895, 18.152	−0.0075	−0.0023	−0.0005	−0.0999
Case2: Unstable						
TSE04	4.084, 4.468	0.292, 17.754	0.0024	0.0875	−0.2921	−0.0004
TSE09	2.394, 3.371	25.386, 64.132	−0.0046	0.0303	−0.2867	−0.1026
TSE13	4.099, 4.635	1.095, 25.022	−0.0069	0.0442	0.0164	−0.0233
Case3: Stable						
TSE04	1.543, 1.819	22.357, 26.260	0.0367	−0.0040	−0.0644	−0.0544
TSE09	2.822, 2.958	37.381, 48.472	−0.0199	0.0215	−0.0578	−0.1802
TSE13	3.596, 3.708	30.499, 32.428	0.0239	0.0180	−0.0464	−0.0605

Note. Simulation data have been subsampled to 0.05 s intervals during 1 hour simulation to match experimental data.

Turbulence spectra

The power spectral density of the longitudinal, u, lateral, v, and vertical, w, components of the velocity and potential temperature, θ, as well as the cross-spectral density, corresponding to the variables uv, uw, vw, and $w\theta$, both from the experimental and numerical data are computed using the Welch method. The 1-hour time series are divided into 20-min windows (10-min overlapping intervals using Hann window). A moving average algorithm, consisting of an averaging interval of 25 data points, is applied to the spectra and cross-spectra to obtain a smoother representation. A first-order low-pass Butterworth filter is applied to mitigate the aliasing effect in both the spectra and co-spectra.

Figure 8.12 shows power spectra of longitudinal (a-c), lateral (d-f), and vertical (g-i) velocity components, as well as potential temperature (j-l) obtained at hub height at the met mast locations from the simulation of the neutral case. The power spectra of the three velocity components are in good agreement with the measured spectra counterparts (a-i), except for the energy drop in the low-to-mid frequency range from TSE04 met mast. The spectra from the WRF-LES model attenuate faster at higher-frequency due to low-pass filtering and numerics involved in the model. Spectra of potential temperature are overestimated in the mid-to-high frequency range by the WLGL model for all met masts. This may be attributed to the improper set-up of the CPM parameters prior to the simulation. In this study, the nondimensional perturbation time scale value of $\mathfrak{T} = 1$ is utilized, as recommended by Muñoz-Esparza et al. [233].

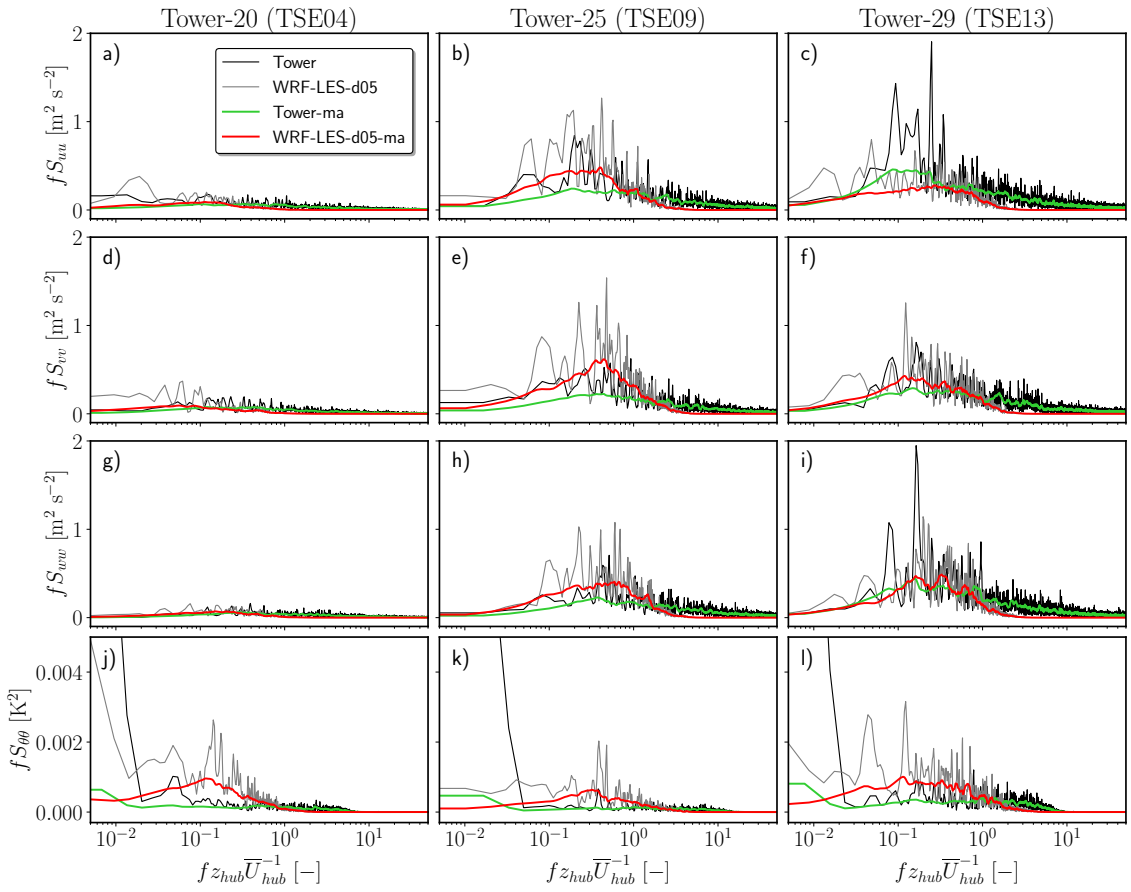

Figure 8.12: Spectra of velocity components (a-i) and potential temperature (j-l) during 1-hour period, represented as a function of nondimensional frequency normalized by hub height, z_{hub}, and 1-hour average horizontal freestream wind speed at hub height, $\overline{U}_{hub}$. "ma" refers to the moving average data from the WLGL model and met masts, consisting of an averaging interval of 25 data points. The results belong to the neutral case.

Figure 8.13 shows power spectra of the above-mentioned hub height atmospheric quantities at the met mast locations for the unstable case. Again, results from the WRF-LES model and measured data are similar, with slightly higher energy content at lower frequencies in the power spectra of the lateral velocity component. As a general conclusion, the WRF-LES model reproduces the measured power spectra at the met mast locations reasonably well.

The power spectra of velocity components and potential temperature for the stable case are given in Figure 8.14. The spectra of velocity components at all tower locations exhibited faster energy decay at higher frequencies (i.e., lower spatial scales) due to turbulent energy dissipation through viscosity in the WRF-LES model. This phenomenon was not observed in the experimental data because the state of the ABL was not completely stable. Instead, it was in transition over the period of interest, resulting in higher turbulence and consequently higher energy levels at all frequencies. Despite having relatively similar mean wind speeds, the energy content in the velocity spectra was significantly lower in the stable case compared to the neutral and unstable cases. The modeled potential temperature spectra showed temperature inversion near the surface, which resulted in vertical mixing

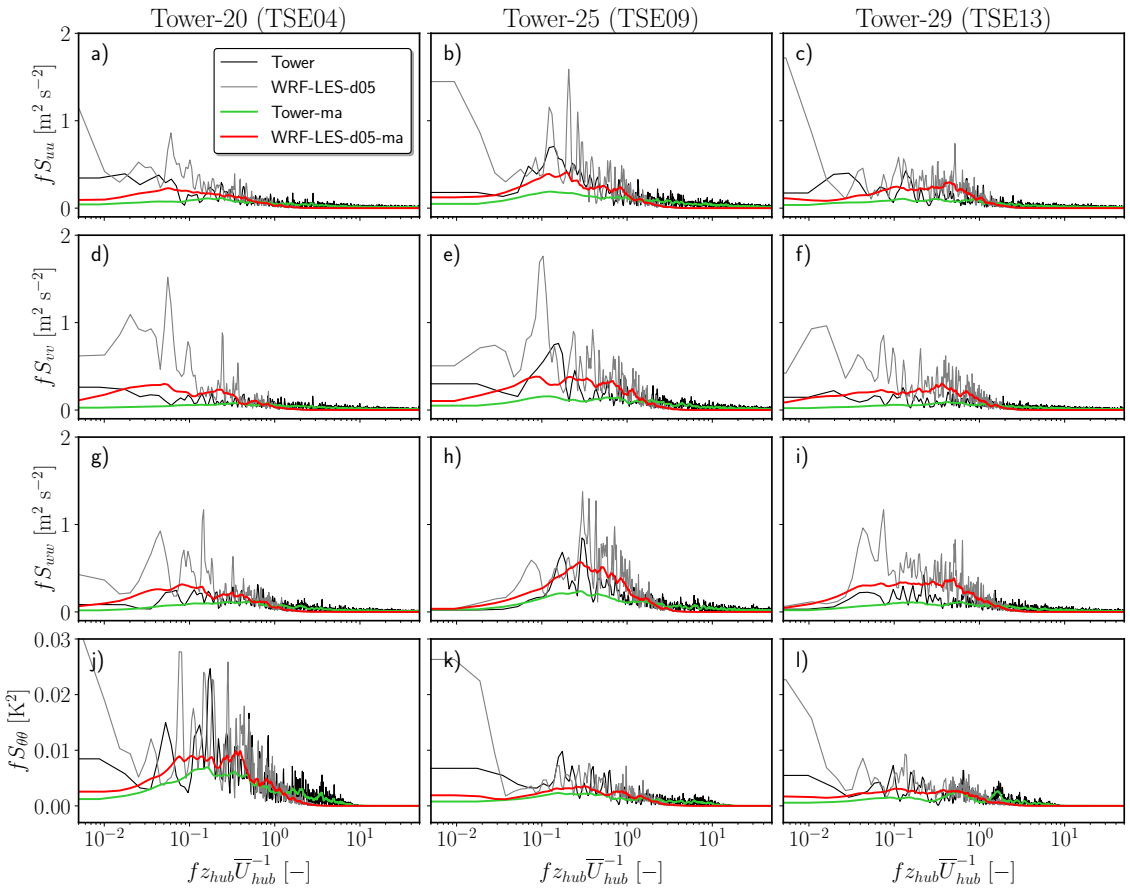

Figure 8.13: Same as in Figure 8.12, but for the unstable case.

being suppressed by the stable boundary layer. This restriction on heat and momentum exchange across the ABL led to the accumulation of energy at lower frequencies.

Figure 8.15 illustrates the uv (a-c), uw (d-f), vw (g-i), and $w\theta$ (j-l) cross-spectra, respectively, for the neutral case. The cross-spectra of different simulated velocity components agree fairly well with the measurement data from the DTU towers. Sensible heat flux cross-spectra from the WLGL model reveal a relatively higher energy content in the low-to-mid frequency range compared to the measured cross-spectra from all the met masts, yet the discrepancy between the simulated and measured spectral content at all frequencies is minor.

The cross-spectra of turbulent velocity components, as well as the cross-spectra of vertical velocity and virtual potential temperature for the unstable case, are given in Figure 8.16. Similar to the neutral case, the agreement between the simulated and observed lower-frequency spectral content of velocity components is good, with slightly higher lower-frequency content from the simulated uw spectra on the ridges. A sufficiently accurate reproduction of the cross-spectra of $w\theta$ and turbulent stress components at all locations indicates that the grid resolution used in the unsteady case is suitable for capturing small-scale buoyancy-driven turbulent structures.

Figure 8.17 shows the same results as in Figure 8.16 but for the stable case. As explained

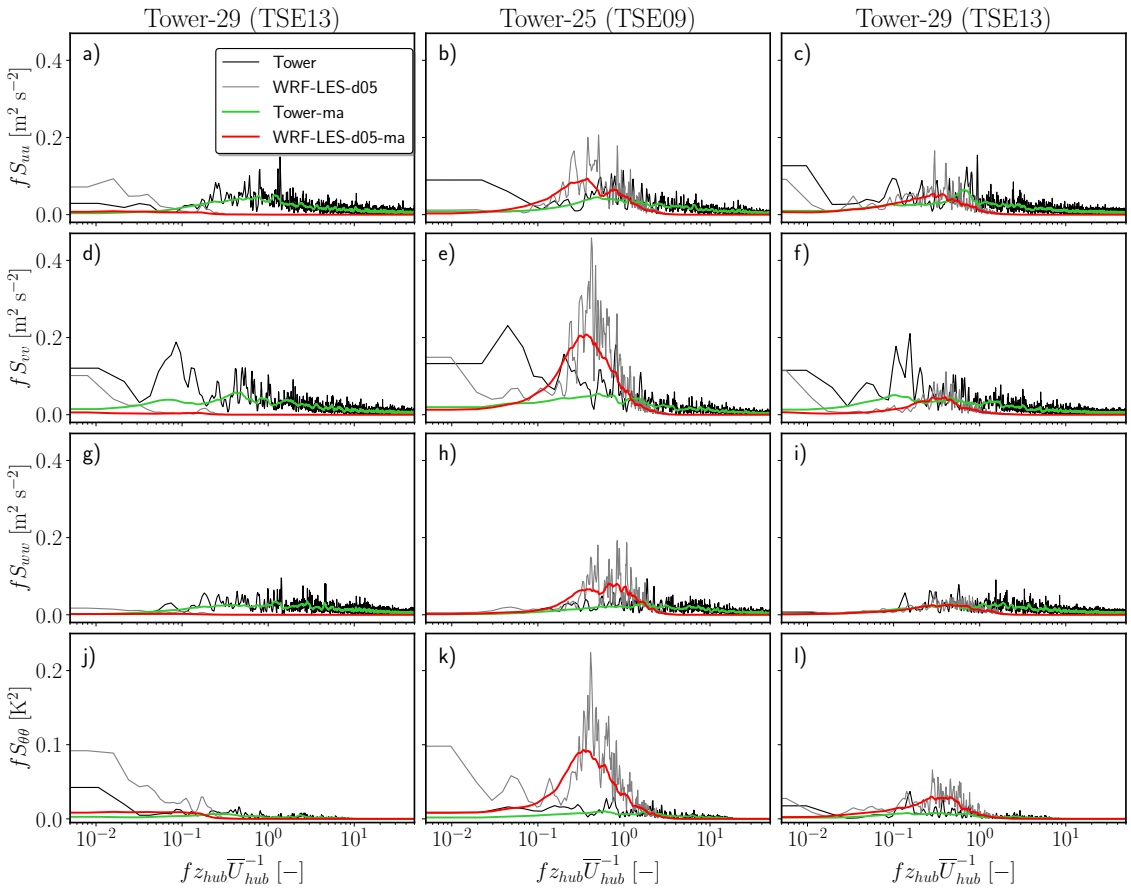

Figure 8.14: Same as in Figure 8.12, but for the stable case.

earlier, the cross-spectra between velocity components exhibit lower energy levels over a wide frequency range than in the neutral and unstable conditions, due to lower variability in all velocity components. The peaks with higher energy levels reproduced by the WLGL model in the $w\theta$ cross-spectra in the valley and on top of the NE ridge than on the SW ridge are associated with the longer wind turbine wake propagated into the valley. The wake persisting over long distances into the valley affected the wind flow on the lee side of the SW ridge and the redistribution of momentum in the vertical direction. Since the modeled flow was not disturbed by additional factors during the period of interest, the third control point on top of the second ridge was also affected. Thus, it resulted in higher energy levels in the cross-spectra of $w\theta$ in the mid-to-high frequency range and dissipated in a similar trend observed in measurements from the TSE13 met mast.

8.1.6 Wind turbine wake velocity fields and aerodynamic performance

Due to slight misalignment between the mean wind direction and wake transect ($\sim 2°$, $\sim 12°$, and $\sim 9°$ in the neutral, unstable, and stable cases, respectively), the wind turbine wake was not precisely aligned with the DLR lidars scanning vertical planes. Although this minor difference has a negligible effect on the near wake behavior of the wind turbine below hub height ($0.5D$-$1D$, with D being the rotor diameter), it precludes the exact comparison of the wake velocity deficit profiles reproduced by the model along the wake

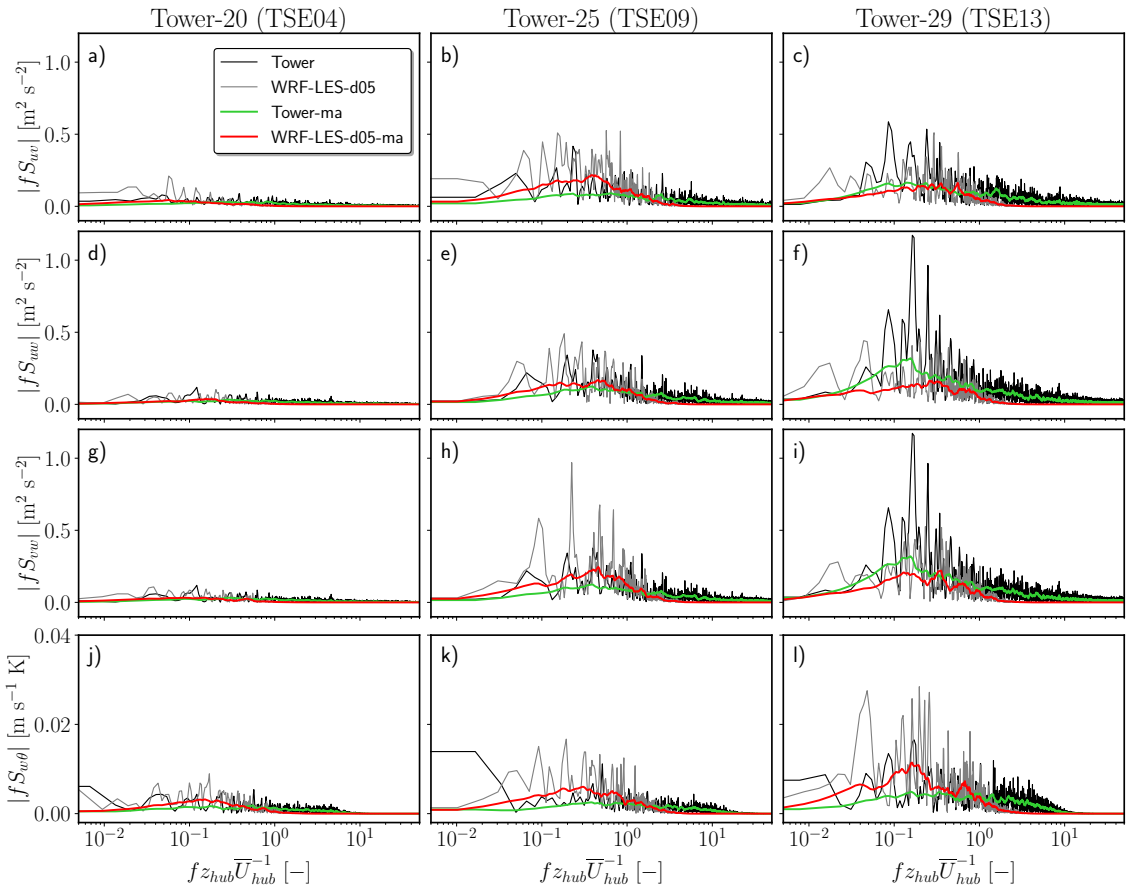

Figure 8.15: Cross-spectra of the u- and v-velocity components (a-c), vertical turbulent stresses, i.e., u- and w- (d-f) and v- and w- (g-i) velocity components, and cross-spectra of the w-velocity component and potential temperature (j-l) that are normalized by corresponding covariances during the 1-hour period, plotted as a function of nondimensional frequency normalized by hub height, z_{hub}, and horizontal wind speed at freestream at hub height, $\overline{U}_{hub}$. Note that only absolute values of the cross-spectra are shown. "ma" refers to the moving average data from the WLGL model and met masts, consisting of an averaging interval of 25 data points. The results correspond to the neutral case.

transect with those obtained from lidar scans. In order to improve the comparison between the simulated wake velocity field and the experimental lidar data, the longitudinal, u, and lateral, v, velocity components are projected onto a rotated coordinate system aligned with the wake transect for all cases.

Time-averaged horizontal wind speed at hub height, $\overline{U}_{hub}$, for the neutral, unstable, and stable cases are illustrated in Figure 8.18. From all figures, it can be understood that the wind speed tends to increase on the southwest and northeast ridges, and there is a recirculation zone formed on the lee side of the ridges where lower wind speeds are observed during the simulation of neutral and stable ABL conditions. The modeled wind turbine wake (encircled by the blue ellipse) for the neutral and stable cases stretches further downstream (up to $\sim 5D$) compared to the unstable case (up to $\sim 3D$), due to lower turbulence levels simulated.

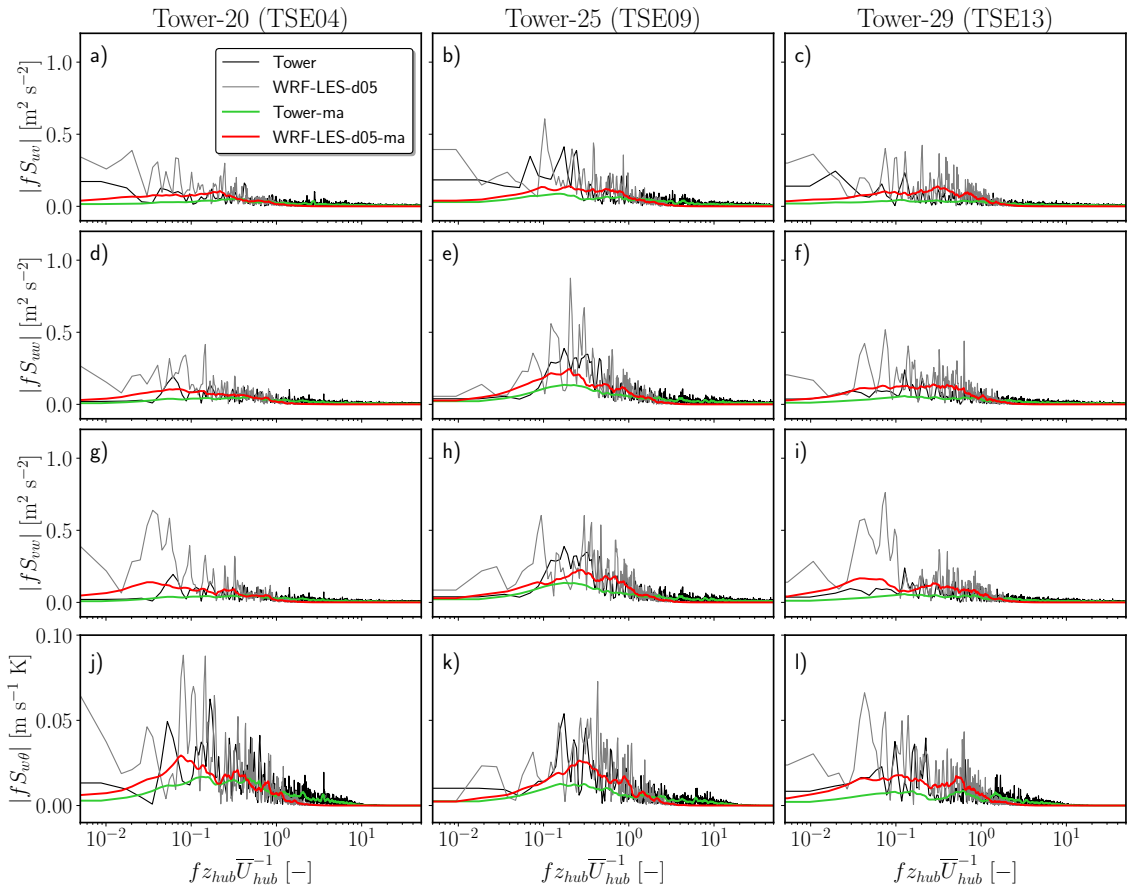

Figure 8.16: Same as in Figure 8.15, but for the unstable case.

For the neutral case, snapshots of instantaneous horizontal wind velocity, U_h, fields from DLR lidars and the WLGL model are shown in Figure 8.19. The snapshots from the DLR85 lidar and WLGL model, presented in the first row of the figure, were taken at approximately 22:41 (UTC), whereas snapshots from DLR86 and the numerical model were taken at approximately 22:27 (UTC). For the unstable case, the instantaneous wind velocity field from the DLR86 lidar and the WLGL model were taken at approximately 16:29 (UTC) and 16:44 (UTC), respectively (Figure 8.20). For the stable case, the instantaneous wind velocity field from the DLR85 and DLR86 lidars, and WLGL model were taken at approximately 04:57 (UTC) and 04:29 (UTC), respectively (Figure 8.21). Although the data from the lidar scans were post-processed, additional filtering was applied to eliminate velocity values with carrier-to-noise ratios less than −24 dB. The instantaneous velocity field from the DLR85 lidar in unstable conditions is not shown here due to large errors in measured line-of-sight velocity. Because the Froude number was greater than unity, $\mathrm{F_L} > 1$, at approximately 04:29 (UTC) and 04:57 (UTC), a longer wavelength mountain wave downwind of the mountain range was observed in the WLGL simulations. This situation was also observable in the DLR85 lidar scan 04:57:36 (UTC) despite the near-unstable ABL conditions measured locally at the TSE04 tower location on the SW ridge, indicating weak static stability rather than strong winds.

Note, transitions of unsteady turbulent flow structures are challenging to capture due

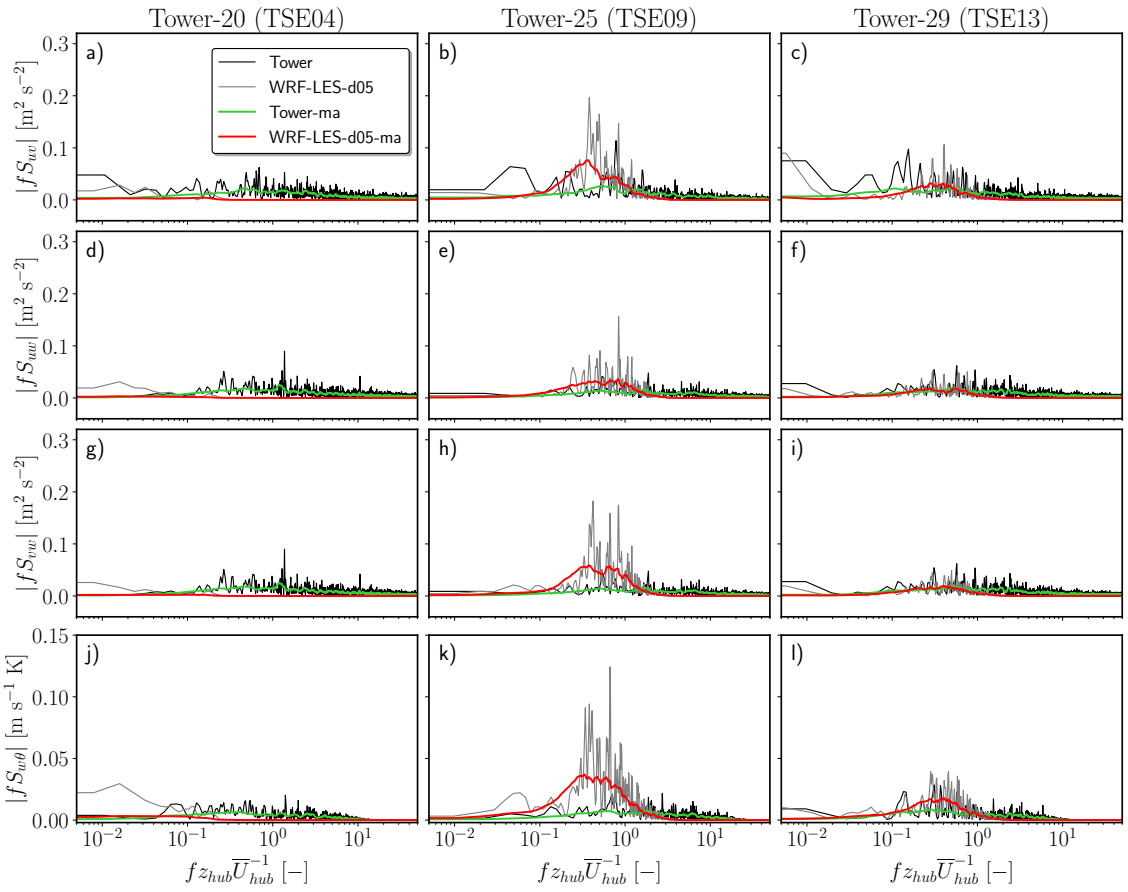

Figure 8.17: Same as in Figure 8.15, but for the stable case. Note the change in the y-axis range compared to the given cross-spectra for the neutral and unstable cases.

to large variability in the modeled and observed wind fields. Therefore, comparisons of instantaneous snapshots of wind fields from the model and observations will likely not match, especially in a complex terrain where wind flow is highly three-dimensional. However, the comparison of instantaneous snapshots of the wind flow fields along the wake and offset transects may provide additional information about the wake formation, as well as recirculation zones occurring downstream of the wind turbine into the valley at a particular time instant.

Figure 8.22 illustrates 1-hour average horizontal wind velocity, $\overline{U}_h$, fields from the DLR and DTU lidars, and WLGL model observed during the neutral case. Both DLR85 and DLR86 lidars capture the upward deflection of the wake, which extends up to ~ 200 m downstream of the wind turbine. The WLGL model predicts the horizontal extension of the wake fairly well, but it does not indicate the upward shift of the wake centerline observed in DLR lidar scans. This is probably due to the underestimation of the impact of buoyant forces (i.e., vertical kinematic heat flux, $\overline{w'\theta'}$) that affects upward-downward turbulence mixing in the model (see time series of the 100-10 m temperature gradient and the Obukhov length in Figure 8.6). A recirculation zone (observed in the 1-hour average horizontal velocity field) is formed on the lee side of the first ridge, which is captured by all the lidars. DTU lidar scans (bottom left plot in Figure 8.22) provide information about

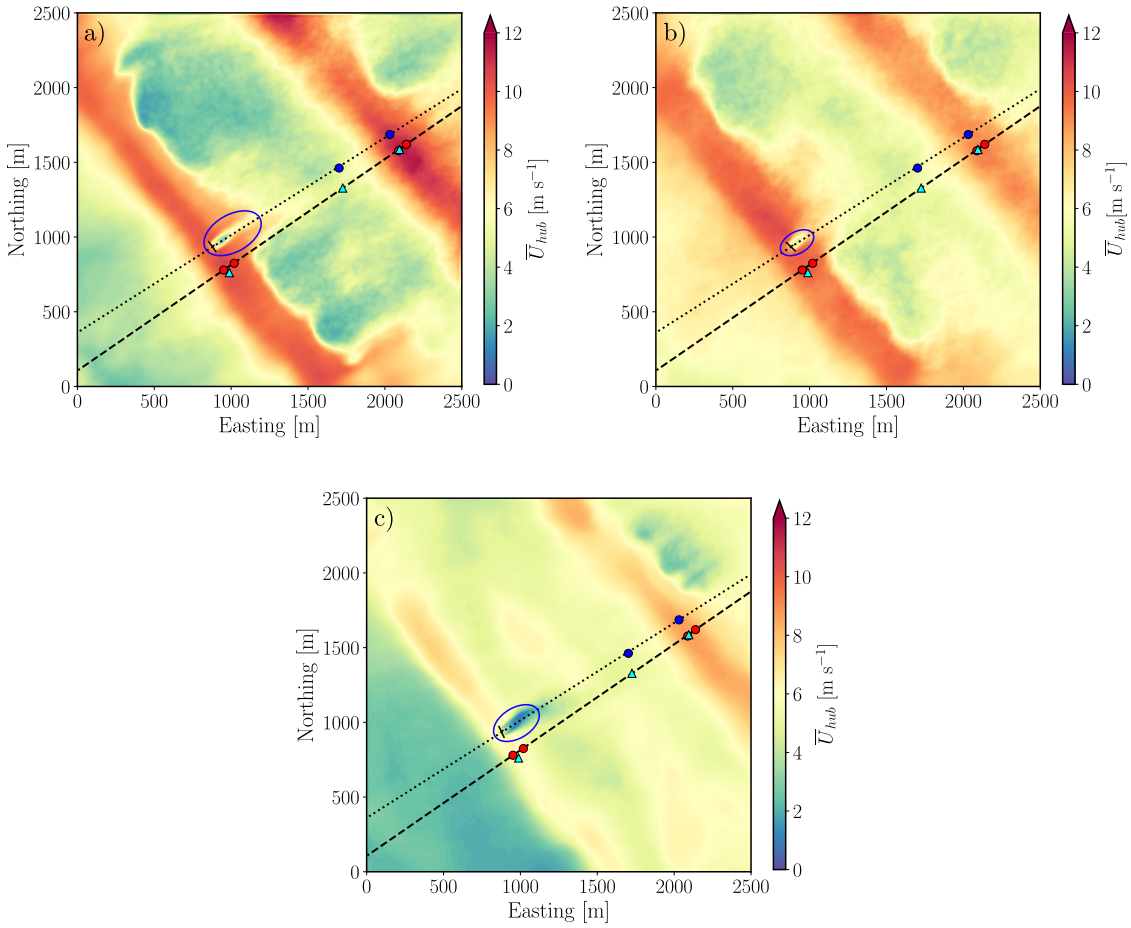

Figure 8.18: Color maps of 1-hour average horizontal wind speed at hub height, $\overline{U}_{hub}$, for the neutral (a), unstable (b), and stable (c) cases. (·····) and (- - -) denote the wake and offset transects, respectively. (●) and (●) indicate the DLR and DTU lidars, while (△) denotes the 100 m DTU towers, respectively. (——) indicate the wind turbine rotor and its wake is encircled by the blue ellipse.

the wind flow topology undisturbed by the wind turbine wake along the offset transect parallel to the wake transect. Although the WLGL model is able to model the recirculating flow, from the lee side of the first ridge into the valley, during the simulation period, the magnitude of the wind velocity in the recirculation zone is underestimated compared to the remote sensing data. The 1-hour bias in mean horizontal wind velocity above ∼600 m is on the order of ∼6 m s^{-1}.

In Figure 8.23, time-averaged horizontal wind velocity, $\overline{U}_h$, fields from the DLR and DTU lidars, and WLGL model are given for the unstable case. Due to the very low carrier-to-noise ratios of the DLR85 scans, the velocity field plotted along the wake transect, which was retrieved from the measured radial velocity, was distorted. The WLGL model captured the recirculation flow patterns observed in the experimental data from the DLR86 and DTU lidars on the lee side of the SW ridge. However, the size of the modeled recirculation zone is much smaller (not visible in the plots due to near-zero velocity values) than that captured by lidar scans. The vertical displacement of the wind turbine wake was